

# DIPLOMARBEIT

Homogenisierte Gleichungen der Strömungsmechanik in  
porösen Medien mit Anwendung auf  
Permeabilitätsberechnungen in Textilien

Angefertigt am  
Institut für Numerische Simulation

Vorgelegt der  
Mathematisch-Naturwissenschaftlichen Fakultät der  
Rheinischen Friedrich-Wilhelms-Universität Bonn

Juli 2006

Von  
Margrit Klitz  
Aus  
Husum



# DIPLOMA THESIS

Homogenised Fluid Flow Equations in Porous Media with  
Application to Permeability Computations in Textiles

Developed at  
the Institute for Numerical Simulation

Presented to  
the Faculty of Mathematics and Natural Sciences of the  
Rheinische Friedrich-Wilhelms-University Bonn, Germany

July 2006

By  
Margrit Klitz  
From  
Husum



# Contents

<b>1. Einleitung</b>	<b>1</b>
1.1. Eine Definition poröser Medien . . . . .	2
1.2. Homogenisierte Gleichungen der Strömungsmechanik in porösen Medien . .	2
1.3. Numerische Vorhersage der Permeabilität $\mathbf{K}$ in Darcys Gesetz . . . . .	4
1.4. Ein duales Porositätsmodell . . . . .	5
1.5. Anwendung auf Permeabilitätsberechnungen in Textilien . . . . .	6
1.6. Numerische Methode . . . . .	8
1.7. Überblick . . . . .	10
<b>1. Introduction</b>	<b>13</b>
1.1. A Definition of Porous Media . . . . .	14
1.2. Homogenised Fluid Flow Equations in Porous Media . . . . .	14
1.3. Numerical Prediction of the Permeability $\mathbf{K}$ in Darcy's Law . . . . .	16
1.4. A Dual Porosity Model . . . . .	17
1.5. Application to Permeability Computations in Textiles . . . . .	18
1.6. Numerical Methodology . . . . .	19
1.7. Thesis Outline . . . . .	21
<b>2. The Mathematical Model</b>	<b>25</b>
2.1. The Navier-Stokes Equations . . . . .	25
2.1.1. The Stokes Equations . . . . .	27
2.1.2. Boundary Conditions . . . . .	27
2.2. Darcy's Law . . . . .	28
2.2.1. Non-Dimensional Formulation of Darcy's Law . . . . .	29
2.2.2. Computation of Permeability via Darcy's Law . . . . .	30
2.3. Brinkman's Equation . . . . .	32
<b>3. Homogenisation of the Stokes and Navier-Stokes Equations</b>	<b>35</b>
3.1. Definition of a Porous Medium . . . . .	36
3.2. Homogenisation of the Stokes Equations . . . . .	37
3.2.1. Main Theorem: Darcy's Law . . . . .	39
3.2.2. Two-Scale Asymptotic Expansion . . . . .	39
3.2.3. Local Solvability of the Stokes System with Two Pressures . . . . .	41
3.2.4. Derivation of Darcy's Law . . . . .	45
3.2.5. Global Solvability of the Stokes Problem with Two Pressures . . . . .	47
3.2.6. Two-Scale Convergence . . . . .	48
3.3. Derivation of Brinkman's Law . . . . .	52
3.4. Slip Boundary Conditions on the Obstacles . . . . .	54

3.5.	On the Choice of the Appropriate Macroscopic Model . . . . .	55
3.6.	Homogenisation of the Navier-Stokes Equations . . . . .	56
3.6.1.	Homogenisation of the Nonstationary Navier-Stokes Equations . . . . .	57
3.6.2.	Derivation of the Nonlinear Brinkman Law . . . . .	58
3.6.3.	Homogenisation of the Navier-Stokes Equations with Varying Viscosity . . . . .	59
3.7.	Homogenisation Theory in Textiles . . . . .	60
<b>4.</b>	<b>Coupled Flow Problems in Plain and Porous Media</b>	<b>63</b>
4.1.	Interface Conditions between Plain and Porous Media . . . . .	63
4.2.	The Penalisation Approach . . . . .	64
4.3.	Penalisation of the Stokes Equations . . . . .	66
4.3.1.	The General Brinkman Model . . . . .	66
4.3.2.	The Fluid-Porous Model . . . . .	66
4.3.3.	An Excursus on the Fluid-Solid Model . . . . .	70
<b>5.</b>	<b>The Numerical Model</b>	<b>73</b>
5.1.	Discretisation of the Navier-Stokes Equations . . . . .	73
5.1.1.	Discretisation in Time . . . . .	74
5.1.2.	Discretisation in Space . . . . .	75
5.1.3.	Time-Step Control . . . . .	76
5.2.	Semi-Implicit Solution of the Navier-Stokes Equations . . . . .	77
5.2.1.	Boundary Conditions . . . . .	78
5.3.	Discretisation of the Brinkman Equations . . . . .	84
5.4.	Implementation of Darcy's Law . . . . .	84
5.5.	Implementation of the Unit Cell Problem . . . . .	85
5.6.	Numerical Analysis of the Semi-Implicit Solver . . . . .	86
5.6.1.	Lid-Driven Cavity Flow . . . . .	86
5.6.2.	Convergence Analysis . . . . .	86
5.6.3.	Speed-Up Compared to Explicit Computations . . . . .	89
<b>6.</b>	<b>Parallelisation</b>	<b>91</b>
6.1.	Parallelisation Strategy . . . . .	91
6.2.	Parallelisation of the Semi-Implicit Solver . . . . .	92
6.3.	Speed-Up and Efficiency of the Parallelised Solver . . . . .	93
<b>7.</b>	<b>Numerical Homogenisation</b>	<b>97</b>
7.1.	Validation of Permeability Computations in a Cubic Array of Spheres . . . . .	98
7.1.1.	The Two-Dimensional Case . . . . .	98
7.1.2.	The Three-Dimensional Case . . . . .	98
7.2.	3D Stokes versus Navier-Stokes Equations in an Array of Boxes . . . . .	101
7.3.	Validation of Darcy's Law in a Cubic Array of Spheres . . . . .	102
7.4.	Validation of the Stokes/Brinkman Equations . . . . .	103
7.4.1.	Are the Stokes/Brinkman Equations Darcy's Law in the Porous Part? . . . . .	108

---

<b>8. Computation of Textile Permeability</b>	<b>109</b>
8.1. Textile Architecture . . . . .	109
8.2. The Applied Mathematical Model . . . . .	111
8.3. Computation of the Local Yarn Permeability . . . . .	111
8.3.1. Derivation of Yarn Permeability According to Gebart . . . . .	112
8.3.2. Derivation of Yarn Permeability According to Berdichevsky and Cai . . . . .	114
8.3.3. Transformation of the Permeability Tensor . . . . .	115
8.3.4. Comparison to Finite Volume Numerical Results . . . . .	116
8.4. Monofilament Fabric . . . . .	121
8.5. Non Crimp Carbon Fabric . . . . .	124
8.6. Carbon Woven Fabric . . . . .	126
<b>9. Conclusion</b>	<b>129</b>
<b>A. Appendix</b>	<b>133</b>
A.1. Lebesgue and Sobolev Spaces . . . . .	133
A.2. Two-Scale Function Spaces . . . . .	133
A.3. Elementary Inequalities . . . . .	134
<b>Bibliography</b>	<b>135</b>



# 1. Einleitung

Strömungssimulationen in porösen Medien besitzen eine Vielfalt umwelttechnischer und industrieller Anwendungen. Sie stellen ein wichtiges Werkzeug für die Grundwasserhydrologie, das Bauingenieurwesen, die Erdölproduktion, die keramische Technik, die Automobilindustrie und die Textilkonstruktion dar. In vielen dieser Bereiche sind Experimente sehr zeitraubend oder sogar gefährlich. Daher werden numerische Simulationen zum neuen Maßstab solcher Experimente.

Beispielsweise simulieren Ingenieure unterirdische Strömungen durch poröse Felsen, um die Ausbreitung verunreinigter Flüssigkeiten aus einer Mülldeponie in das Grundwasser vorherzusagen. In industriellen Anwendungen können aus einer Flüssigkeit schädliche Partikel entfernt werden, indem beim Durchströmen eines porösen Mediums dessen kleine Poren den Durchfluß der größeren Teilchen verhindern. Zudem können Strömungssimulationen in porösen Medien die Auswirkungen eines Tsunami im Uferbereich modellieren [2]: Da es rechenstechnisch zu teuer ist, einzelne Bäume, Felsen, Wellenbrecher und Deiche in gefährdeten Gegenden auszugestalten, ist es ein effektiverer Ansatz, solche topographischen Variationen als Bereiche eines porösen Mediums mit gegebener Porosität und Permeabilität zu beschreiben.

Strömungsmodelle solcher Anwendungen müssen mehrere Phasen, thermische Effekte oder zum Beispiel chemische Reaktionen berücksichtigen. Diese können zusätzlich oder als Erweiterung der klassischen Navier-Stokes Gleichungen beschrieben werden. Für die einphasige, isotherme und gesättigte Strömung eines Newtonschen Fluids nehmen die Navier-Stokes Gleichungen in der inkompressiblen Formulierung die Gestalt

$$\begin{aligned} \rho \left[ \frac{\partial \mathbf{u}}{\partial t} + (\mathbf{u} \cdot \nabla) \mathbf{u} \right] + \nabla p &= \mu \Delta \mathbf{u} + \rho \mathbf{g} && \text{in } \Omega \times (0, T) \\ \nabla \cdot \mathbf{u} &= 0 && \text{in } \Omega \times (0, T) \end{aligned} \tag{1.1}$$

an, wobei  $\Omega$  eine offene Teilmenge des  $\mathbb{R}^n$ ,  $\rho(\mathbf{x}, t) = \rho_\infty$  die für inkompressible Fluide konstante Dichte und  $\mu$  die dynamische Viskosität ist. Außerdem steht  $\mathbf{u} : \Omega \times [0, T] \rightarrow \mathbb{R}^n$  für das Geschwindigkeitsfeld,  $p : \Omega \times [0, T] \rightarrow \mathbb{R}$  für den Druck und  $\mathbf{g}$  für die Volumenkräfte wie etwa die Gravitation. Die erste Gleichung beschreibt die Erhaltung des Impulses (Impulsgleichung), die zweite die Erhaltung der Masse (Kontinuitätsgleichung).

Allerdings ist die direkte numerische Strömungssimulation durch Lösung der Navier-Stokes Gleichungen (1.1) in der Mikrostruktur der Poren in vielen Fällen aufgrund der hierarchischen Struktur des porösen Mediums unmöglich [45]. Um dies zu verstehen, wird zunächst eine allgemeine Beschreibung solcher Medien gegeben.

## 1.1. Eine Definition poröser Medien

By a porous medium we mean a material consisting of a solid matrix with an interconnected void. We suppose that the solid matrix is either rigid (the usual situation) or it undergoes small deformation. The interconnectedness of the void (the pores) allows the flow of one or more fluids through the material.

*Donald A. Nield and Adrian Bejan [50, p.1]*

Dieser Definition folgend, finden wir viele Beispiele natürlicher und synthetischer poröser Medien. Natürliche poröse Medien sind beispielsweise Sand, Sandstein, Kalkstein, Roggenbrot, Holz und die menschliche Lunge. In diesen Medien kann die Größe und Verteilung der Poren sehr irregulär sein. Im Gegensatz dazu haben synthetische poröse Medien meist eine wohldefinierte oder gar periodische Struktur wie zum Beispiel Wischtücher, Windeln, Papiermaschinenbespannungen, Aktivkohlefilter, Ölfilter und Diesel-Partikelfilter. In solchen Fällen ist die Struktur des Mediums bereits durch eine periodisch fortsetzbare Zelle definiert, die z.B. bei einem Textil aus Fasern bestimmter Breite und Richtung besteht (Abb. 1.1).

Ein typisches Charakteristikum poröser Medien ist die Porösität, die den Anteil des freien Raumes am Gesamtvolumen bezeichnet. Für natürliche Medien ist dieser Wert normalerweise nicht größer als 0.6 [50]. Andere übliche Werte der Porösität sind 0.43 bis 0.54 für Erde, 0.02 bis 0.07 für Beton und 0.17 bis 0.49 für Zigarettensfilter [50].

Alle porösen Medien sind durch mindestens zwei verschiedene Längenskalen charakterisiert. Zum einen ist dies die Größe der Poren (Mikroskala), zum anderen die Größe der Form oder des Reservoirs, in dem das Medium eingebettet ist (Makroskala). Für gewöhnlich unterscheiden sich beide Skalen um mehrere Größenordnungen. Zum Beispiel ist die textile Zelle in Abb. 1.1 typischerweise ungefähr 5mm groß, das hergestellte Gewebe dagegen ungefähr einhundert Mal größer. Ebenso werden Grundwasserströmungen im Quadratkilometerbereich modelliert, während die Porengröße kleiner als ein Millimeter ist.

Dieser Größenunterschied in den Längenskalen macht die direkte numerische Strömungssimulation zeit- und speicherraubend: Die Auflösung der Poren erfordert sehr feine Gitter (und entsprechend sehr kleine Zeitschritte), die die Kapazitäten der existierenden Rechnerstrukturen stark in Anspruch nehmen. Da jedoch die charakteristische Größe des festen Anteils in einer Wiederholungszelle eines Mediums klein ist gegenüber der Gesamtheit des Mediums, gibt es bestimmte mathematische Techniken, die eine „Mittelung“, „Homogenisierung“ oder „Hochskalierung“ der strömungsmechanischen Gleichungen erlauben, wodurch man Gleichungen auf der Makro- statt auf der Mikroskala erhält. Von diesen hofft man dann, daß sie numerisch für Simulationszwecke einfacher zu handhaben sind. Eine dieser Techniken ist die Homogenisierung [7, 31, 45, 53].

## 1.2. Homogenisierte Gleichungen der Strömungsmechanik in porösen Medien

In der Homogenisierungstheorie wird versucht, die Diskrepanz in den Längenskalen durch eine Multiskalenentwicklung zu überbrücken [45], welche das Verhalten der Flüssigkeit auf

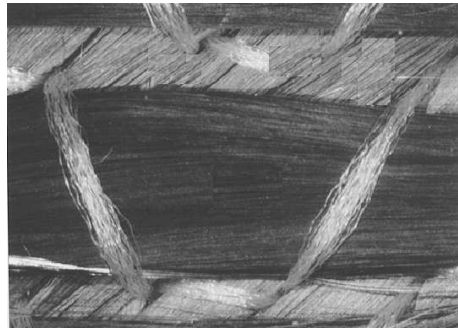


Abb. 1.1.: Beispiel einer textilen Wiederholungszelle [Bild: S.V. Lomov].

den zwei verschiedenen Längenskalen  $x$  und  $x/\varepsilon$  enthält:

$$\mathbf{u}^\varepsilon = \varepsilon^\beta \left\{ \mathbf{u}_0 \left( \mathbf{x}, \frac{\mathbf{x}}{\varepsilon} \right) + \varepsilon \mathbf{u}_1 \left( \mathbf{x}, \frac{\mathbf{x}}{\varepsilon} \right) + \varepsilon^2 \mathbf{u}_2 \left( \mathbf{x}, \frac{\mathbf{x}}{\varepsilon} \right) + \dots \right\}. \quad (1.2)$$

Eine solche Entwicklung für die Geschwindigkeit  $\mathbf{u}$  und den Druck  $p$  wird in die Strömungsgleichungen (1.1) auf der Mikroskala eingesetzt, zusammen mit einer entsprechenden Transformation der Operatoren  $\nabla$  und  $\Delta$ . Im nächsten Schritt wird der Grenzwert  $\lim_{\varepsilon \rightarrow 0} \mathbf{u}_\varepsilon$  untersucht, der dem Verschwinden der Porenstruktur entspricht. Die Grundidee hinter diesem Prozeß ist, daß die komplizierte Mikrostruktur ausgemittelt wird und die im Grenzwert gewonnene partielle Differentialgleichung, die ein sogenanntes Filtrationsgesetz darstellt, numerisch besser zu lösen ist.

Zum Beispiel ergibt die Homogenisierung der Navier-Stokes Gleichungen (1.1) für eine große konstante Viskosität  $\mu$  in periodischen und zufälligen Medien Darcys Gesetz auf der Makroskala [7, 45, 53]

$$\langle \mathbf{u} \rangle = -\frac{1}{\mu} \mathbf{K} \cdot \nabla p \quad \text{in } \Omega, \quad (1.3)$$

mit der Bezeichnung  $\langle \cdot \rangle$  für die Volumenmittelung und dem Permeabilitätstensor  $\mathbf{K}$ , der ein Maß für die Durchlässigkeit eines Materials gegenüber Fluiden ist. Dieser Tensor ist die einzige Größe in der homogenisierten Gleichung, in welcher die Information über die komplizierte Porengeometrie enthalten ist. Darcys Gesetz ist ausschließlich für langsame, viskose Strömungen gültig, jedoch erfüllen zum Beispiel die meisten Grundwasserströmungen diese Annahme. Daher müssen in diesem Fall nicht die Navier-Stokes Gleichungen in komplizierten Fels- und Erdreichgeometrien gelöst werden, sondern statt dessen die lineare Gleichung (1.3). Nichtsdestotrotz ist eine verlässliche numerische Vorhersage der Unbekannten  $\mathbf{K}$  absolut notwendig, um dann Darcy-Löser mittels Finiten Elementen oder Finiten Differenzen zur Strömungssimulation anwenden zu können [55, 59].

Arbeiten, die sich dem Studium der Permeabilität von porösen Medien im allgemeinen und von Textilien im besonderen widmen, können eingeteilt werden in rein experimentelle Ansätze, rein theoretische und solche, die auf analytischen Ansätzen mit numerischen Methoden zur Bestimmung der Permeabilität basieren. Jedoch, wie Mei, Auriault und Ng [42] hervorheben „there are many more theoretical papers applying the method of homogenisa-

tion [...] than there are quantitative solutions of the cell problems“. So ist die Theorie der Homogenisierung in der Literatur stark vertreten (vgl. [7, 31, 45, 53]), aber die numerische Anwendung und Diskussion der abgeleiteten Formeln ist eher spärlich [34, 47, 52]. Im Gegensatz dazu gibt es eine große Zahl von rein heuristischen Ansätzen zur Berechnung der Permeabilität [49], in denen Filtrationsgesetze wie Darcys Gesetz erfolgreich angewendet werden, ohne die Anwendbarkeit im einzelnen Fall zu prüfen.

Daher werden wir in dieser Arbeit insbesondere die beiden Punkte behandeln, welche in der theoretischen wie auch in der angewandten Literatur zur Homogenisierung am meisten fehlen:

1. Wir diskutieren, für welche speziellen Probleme die verschiedenen homogenisierten Gleichungen gültig sind.
2. Wir lösen die entstehenden Gleichungen numerisch zur Vorhersage der Permeabilität  $\mathbf{K}$ .

Als ein Beispiel der beschränkten Gültigkeit einiger homogenisierter Gleichungen betrachten wir spezielle Gleichungen, die ebenfalls mittels Homogenisierung aus den Navier-Stokes Gleichungen gewonnen werden (1.1), nämlich die Brinkman Gleichungen [7, 45]

$$\begin{aligned} \nabla p - \mu \Delta \mathbf{u} + \frac{\mu}{\sigma^2} \mathbf{M} \mathbf{u} &= f & \text{in } \Omega \\ \nabla \cdot \mathbf{u} &= 0 & \text{in } \Omega \\ \mathbf{u} &= 0 & \text{auf } \partial \Omega. \end{aligned} \tag{1.4}$$

Hierbei ist  $\sigma$  ein bestimmtes Verhältnis von festen Anteilen im porösen Medium und  $\mathbf{M}$  eine Permeabilität, die jedoch anders definiert ist als  $\mathbf{K}$  in Darcys Gesetz. Bemerkenswert ist, daß beide Filtrationsgesetze im selben Medium aus denselben Gleichungen stammen und der einzige Unterschied in der Herleitung eine unterschiedliche Skalierungsannahme an feste und flüssige Teile ist.

Nach einer Skalenuntersuchung wie in [34] erkennt man jedoch, daß die Brinkman Gleichungen (1.4) ausschließlich für Medien mit sehr hoher Porosität angewendet werden sollten, d.h. mit einer Porosität nahe bei Eins. Daher sind diese Gleichungen weder für natürliche Medien noch für Textilien, hingegen aber beispielsweise für harten Schaumstoff mit Porosität 0.972 [50] anwendbar. Solche Betrachtungen sind nur sehr selten in theoretischen Arbeiten zur Homogenisierungstheorie zu finden.

Rückkehrend zu Darcys Gesetz (1.3) wollen wir nun sehen, wie die Permeabilität  $\mathbf{K}$  numerisch bestimmt werden kann.

### 1.3. Numerische Vorhersage der Permeabilität $\mathbf{K}$ in Darcys Gesetz

Abgesehen von der Anwendbarkeit in der Strömungssimulation auf der Makroskala kann Darcys Gesetz auch zur numerischen Berechnung der Permeabilität [18, 26, 49, 61] benutzt werden. Unter der Voraussetzung, daß das poröse Medium eine periodische Struktur hat,

genügt es, die Strömung in einer Einheitszelle zu bestimmen. In dieser Zelle werden die Navier-Stokes Gleichungen (1.1) und somit das Geschwindigkeitsfeld  $\mathbf{u}$  und der Druck  $p$  berechnet und dann als Eingangsgrößen für Darcys Gesetz im stationären Zustand benutzt. Die Gleichungen (1.1) müssen also nur in einer einzelnen Zelle und nicht im ganzen Medium gelöst werden.

Nichtsdestotrotz bietet die Homogenisierung eine weitere (letztlich besser zu berechnende) Definition des Permeabilitätstensors [45, 53] in  $n$  Dimensionen

$$K_{ij} = \int_{Y_F} \nabla_y \mathbf{w}^i \nabla_y \mathbf{w}^j d\mathbf{y} \text{ for } 1 \leq i, j \leq n. \quad (1.5)$$

Dabei ist  $\mathbf{w}^i$  für  $1 \leq i \leq n$  die Lösung des sogenannten Einheitszellproblems: Finde  $(\mathbf{w}^i, \pi^i) \in H_{\text{per}}^1(Y)^n \times L^2(Y)$  für  $1 \leq i, j \leq n$ , so daß

$$\begin{aligned} -\Delta \mathbf{w}^i + \nabla \pi^i &= \mathbf{e}^i && \text{in } Y_F \\ \nabla \cdot \mathbf{w}^i &= 0 && \text{in } Y_F \\ \mathbf{w}^i &= 0 && \text{auf } \partial Y_F \setminus \partial Y \\ \mathbf{w}^i, \pi^i &&& Y - \text{periodisch,} \end{aligned} \quad (1.6)$$

wobei  $\mathbf{e}^i$  den Vektor mit den Komponenten  $e_j^i = \delta_{ij}$  bezeichnet,  $Y$  eine Einheitszelle des porösen Mediums mit  $\mathbf{y} \in Y$  ist und  $Y_F$  und  $Y_S$  die entsprechenden flüssigen und festen Teile bezeichnen.  $H_{\text{per}}^1(Y)^n$  sei der Sobolev-Raum  $H^{1,2}(Y)^n$  beschränkt auf  $Y$ -periodische Funktionen. Weiterhin sind  $(\mathbf{w}^i, \pi^i)$  vergleichbar mit den Fluidgeschwindigkeiten und dem Druck in den Stokes Gleichungen (der linearisierten Form der Navier-Stokes Gleichungen (1.1)). Daher führt die Lösung des Einheitszellproblems in 3D zur Lösung von drei Stokes Gleichungen mit externen Kräften  $(\mathbf{e}^i)_{1 \leq i \leq 3}$ , aus welcher die  $(\mathbf{w}^i)_{1 \leq i \leq 3}$  erhalten werden, die ihrerseits Eingang in  $\mathbf{K}$  finden. Dies führt zu denselben Ergebnissen wie die Berechnung der Permeabilität  $\mathbf{K}$  nach Darcys Gesetz, da in der Einheitszelle beide Probleme äquivalent sind [53].

## 1.4. Ein duales Porositätsmodell

Falls eine weitere Längenskala im porösen Medium berücksichtigt werden muß, d.h. falls der feste Anteil der porösen Matrix selbst porös ist, werden die Navier-Stokes/Brinkman Gleichungen

$$\begin{aligned} \rho \left[ \frac{\partial \mathbf{u}}{\partial t} + (\mathbf{u} \cdot \nabla) \mathbf{u} \right] + \nabla p + \mu \mathbf{K}_{\text{tow}}^{-1} \mathbf{u} &= \mu \Delta \mathbf{u} && \text{in } \Omega \\ \nabla \cdot \mathbf{u} &= 0 && \text{in } \Omega, \end{aligned} \quad (1.7)$$

benutzt, wobei  $\mathbf{K}_{\text{tow}}$  die Permeabilität auf der kleinsten Skala ist. Die Brinkman Gleichungen sind eine praktische Methode, um gekoppelte Strömungsprobleme in freien und porösen Medien zu beschreiben [33], da Angot [13] zeigte, daß diese Gleichungen ohne explizite Bedingungen an den Grenzflächen benutzt werden können. Der zusätzliche Term  $\nu \mathbf{K}_{\text{tow}}^{-1} \mathbf{u}$  ist dabei ein Bestrafungsterm der Navier-Stokes Gleichungen (1.1). So konvergieren die Glei-

chungen (1.7) gegen die Gleichungen (1.1) für große  $\|\mathbf{K}_{\text{tow}}\|$  im Fluidgebiet. Im Bereich des porösen Mediums ist (1.7) eine Brinkmanartige Gleichung mit der spezifischen Permeabilität im porösen Teil. Außerdem kann, da die spezifische Permeabilität  $\|\mathbf{K}_{\text{tow}}\|$  für gewöhnlich klein ist ( $10^{-4}\text{mm} \leq \|\mathbf{K}\|_{\text{max}} \leq 10^{-7}\text{mm}$  für Textilien), der Term  $\mu\mathbf{K}_{\text{tow}}^{-1}\mathbf{u}$  als dominant über den viskosen und konvektiven Term,  $\mu\Delta\mathbf{u}$  und  $(\mathbf{u} \cdot \nabla)\mathbf{u}$ , angesehen werden, und daher wird wiederum Darcys Gesetz (1.3) im porösen Medium erfüllt.

Diese Gleichungen sollten nicht mit den Brinkman Gleichungen (1.4) in der Homogenisierungstheorie verwechselt werden, da Gleichungen (1.7) keine homogenisierten Gleichungen darstellen und sich die Definition der Permeabilität in beiden unterscheidet.

## 1.5. Anwendung auf Permeabilitätsberechnungen in Textilien

Eines der Hauptziele dieser Arbeit ist die Prognose der Permeabilität von Textilien. Um die Strömung in Textilien modellieren zu können, ist es essentiell, eine solche Vorhersage schnell treffen zu können. Ein wichtiges Beispiel aus der Anwendung ist das sogenannte Liquid Composite Moulding (LCM) für die Herstellung von Verbundstoffen mit textiler Verstärkung. Um einen solchen Verbundstoff herzustellen, wird z.B. beim Resin Transfer Moulding (RTM) mit niedrigem Druck Kunstharz in einen geschlossenen Hohlraum injiziert, der mit Textilfasern gefüllt ist. Das Ziel der numerischen Strömungsberechnung ist nun, den Fluß des Harzes zwischen den Fasern so zu optimieren, daß Hohlräume und Luftblasen vermieden werden und die Injektionszeit reduziert wird. Die existierenden Verfahren zur Simulation dieses Kunstharzflusses wie etwa PAM-RTM oder LIMS [55, 59] benötigen die Werte der Permeabilität an verschiedenen Stellen in der Form.

Die Berechnung der Permeabilität setzt eine genaue Beschreibung der textilen Verstärkungsstruktur voraus, die von der WiseTex Software [63], entwickelt an der Katholieke Universiteit Leuven in Belgien, bereitgestellt wird. In Kooperation mit den Forschungsgruppen Verbundstoffe und Technisch-Wissenschaftliches Rechnen in Leuven entwickeln wir ein neues Modul für deren Softwarepaket FlowTex, das die Berechnung der Permeabilität von textilen Verstärkungen beinhaltet. Dieses Modul basiert auf dem frei erhältlichen Strömungslöser NaSt3DGP [3], einem CFD Paket, das am Institut für Numerische Simulation in der Forschungsgruppe von Prof. Michael Griebel [28] entwickelt wird.

Textilien sind spezielle poröse Medien, die mit den folgenden Vereinfachungen und Herausforderungen verbunden sind:

- Textilien sind periodische, zusammenhängende poröse Medien.
- Strömungen durch Textilien sind höchst laminar.
- Fasern in einem Textil können selber porös sein, was eine weitere Skala in unserem Modell zur Folge hat (Abb. 1.2).
- Textilien haben ziemlich komplizierte Strukturen, sogar wenn man nur eine Einheitszelle betrachtet (Abb. 1.1), und sind außerdem oft mehrlagig.
- Textilingenieure benötigen die Permeabilität an unterschiedlichen Positionen in der Form, was eine schnelle Berechenbarkeit voraussetzt.

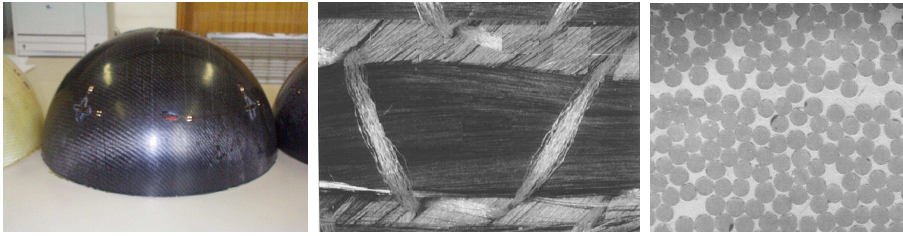


Abb. 1.2.: Skalen in textilen Verstärkungen: die Makroskala des Gewebestücks ( $\approx 1\text{m}$ ), die Mesoskala einer periodisch vorsetzbaren Zelle ( $\approx 0.01\text{m}$ ) und die Mikroskala der Fäden ( $\approx 0.0001\text{m}$ ) [Bild: S.V. Lomov].

Da Textilien eine periodische Struktur haben, konzentrieren wir uns in dieser Arbeit auf periodische poröse Medien und lassen außerdem keine Verformungen zu. Es kann gezeigt werden, daß die Homogenisierungstheorie auch für das zusammenhängende Textilgewebe gilt [5], weshalb die Berechnung der Permeabilität in einer Einheitszelle des Gewebes (Abb. 1.1) durchgeführt werden kann, und zwar indem entweder das Einheitszellproblem (1.6) oder Darcys Gesetz (1.3) gelöst wird.

Wir untersuchen Newtonsche Ein-Phasen-Strömungen durch die Poren der Textilien, was grundsätzlich mit den inkompressiblen Navier-Stokes-Gleichungen (1.1) modelliert werden kann. Die Viskosität  $\mu$  ist dabei ein Maß für den inneren Widerstand bzw. die Zähflüssigkeit des Fluids. Mit Einführung der dimensionslosen Reynoldszahl  $Re \equiv \rho_\infty u_\infty L / \mu$ , wobei  $L$  und  $u_\infty$  charakteristische Referenzgrößen sind, erhält man dann ein Maß für das Verhältnis von Trägheits- zu Reibungskräften. Beim Resin Transfer Moulding liegen die Geschwindigkeiten typischerweise im Bereich  $10^{-3}\text{ m/s}$  und die Reynoldszahl bei 0.05 [55, 59]. In diesen Größenordnungen sind Strömungen höchst laminar, und wir werden zeigen, daß sie in diesem Fall und für die dort wirkenden Kräfte ausreichend durch die linearen Stokes-Gleichungen beschrieben werden.

Betrachtet man die hierarchische Struktur von Textilien genauer, muß noch eine weitere Skala eingeführt werden (Abb. 1.2). Eine periodisch fortsetzbare Zelle des Gewebes besteht nämlich aus porösen Fasern, die wiederum aus Fäden aufgebaut sind. Daher muß unser Modell zwei verschiedene Längenskalen für die Porösität in Betracht ziehen, wodurch auch passende Bedingungen für die Grenzflächen zwischen einem reinen Strömungs- und einem porösen Gebiet gewählt werden müssen. Die Strömungen selber werden dann entweder durch die Navier-Stokes/Brinkman Gleichungen (1.7) oder die linearisierten Stokes/Brinkman Gleichungen beschrieben.

Der Ansatz in dieser Arbeit vermeidet bewußt die problematischen Bedingungen an den Grenzflächen, was mathematisch von Angot in [12] für den linearen Fall und von Angot, Bruneau und Fabrie in [13] für den nichtlinearen Fall gerechtfertigt wurde. Darin führt Angot einen Fehlerschätzer für die Lösung der Stokes/Brinkman Gleichungen im Vergleich zu den Lösungen der Brinkman und der Stokes Gleichungen ein, wobei er eine stetige Spannung und stetige Geschwindigkeit an den Grenzflächen voraussetzt. Allerdings bezieht sich Angots Fehlerschätzer nur auf skalare Permeabilitäten, was wir jedoch in dieser Arbeit auf

den Fall erweitern, daß die Permeabilität ein diagonaler, positiv definitiver Tensor zweiter Ordnung ist. Von solcher Form sind nämlich genau die Permeabilitäten auf textilen Mikroskalen.

Darüber hinaus muß auch die Permeabilität der Fasern  $\mathbf{K}_{\text{tow}}$  berechnet werden. Eine solche Berechnung ist bereits in der FlowTex Software implementiert, basierend auf semi-analytischen Formeln von Berdichevsky und Cai [18] und von Gebart [26].

Um all den oben erwähnten Aspekten gerecht zu werden, wurde für diese Arbeit eine Vielzahl von numerischen Methoden basierend auf dem Navier-Stokes Löser NaSt3DGP [3] implementiert.

## 1.6. Numerische Methode

Der dreidimensionale Navier-Stokes Löser NaSt3DGP [3] arbeitet vollständig parallel und ist eine gute Basis für Modifikationen und Erweiterungen zur schnellen Permeabilitätsberechnung.

In NaSt3DGP wird die Chorinsche Projektionsmethode [20] benutzt, die mit einer der üblichsten numerischen Ansätze zur Lösung der Navier-Stokes Gleichungen ist: Zunächst werden die Impulsgleichungen über die Zeit transportiert, um eine Näherung der Geschwindigkeit  $\mathbf{u}$  oder eines provisorischen Geschwindigkeitsfeldes  $\mathbf{u}^*$  zu erhalten. Dann wird eine elliptische Gleichung gelöst, welche die Divergenzfreiheit  $\nabla \cdot \mathbf{u} = 0$ , erzwingt und den Druck bestimmt.

Die Impulsgleichungen werden explizit in der Zeit vorangetrieben durch Euler- oder Adam-Bashforth-Integration, was eine Zeitschrittweitenbeschränkung für die konvektiven Terme wie auch für die Diffusionsterme und die Volumenkräfte ergibt. Diese Beschränkung sichert die numerische Stabilität des Verfahrens.

Allerdings ist im Bereich niedriger Reynoldszahlen die Stabilitätsbeschränkung der diffusiven Terme der Navier-Stokes Gleichung sehr viel restriktiver als die Bedingung für die konvektiven Terme. Deshalb diskretisieren wir die diffusiven Terme implizit in der Zeit durch ein Crank-Nicolson Schema und lassen die konvektiven Terme explizit. Dies führt zu einem sogenannten semi-impliziten Verfahren für die Navier-Stokes Gleichungen bzw. zu einem rein impliziten für die Stokes Gleichungen.

Die Navier-Stokes Gleichungen (1.1) werden numerisch auf einem regulären versetzten Gitter (staggered grid) mit Finite Volumen-Diskretisierung gelöst. Bei einem versetzten Gitter wird der Druck im Zentrum der Zellen diskretisiert, die Geschwindigkeiten dagegen auf den Zell-Seiten. Diese Diskretisierung führt zu einer starken Kopplung zwischen Druck und Geschwindigkeiten und vermeidet so unphysikalische Oszillationen im Druck.

Insgesamt mußten die folgenden Modifikationen am Quellcode vorgenommen werden:

- Eine Druckkorrekturmethode [15] wurde implementiert, zusammen mit einem semi-impliziten Lösungsalgorithmus der Navier-Stokes Gleichungen [19].
- Die Navier-Stokes/Brinkman Gleichungen (1.7) wurden eingefügt und werden semi-implizit in der Zeit gelöst.
- Die obigen Algorithmen wurden erweitert, um die Stokes und die Stokes/Brinkman Gleichungen implizit in der Zeit zu lösen.

- Darcys Gesetz (1.3) und das Einheitszellproblem (1.6) wurden implementiert.
- Alle obigen Zusätze wurden parallelisiert.

Eine der vielen auftauchenden Herausforderungen bei einer (semi-)impliziten Implementation ist die Lösung dreier weiterer linearer Gleichungssysteme für die drei provisorischen Geschwindigkeitskomponenten  $(u^*, v^*, w^*)$ . Nach einigen Tests haben wir uns für eine iterative Methode der konjugierten Gradienten mit symmetrischer sukzessiver Überrelaxation (SSOR) als Präkonditionierung entschieden. Die am schwierigsten zu implementierenden Teile sind die verschiedenen möglichen Randbedingungen für  $(u^*, v^*, w^*)$ , welche durch Manipulationen in der Lösungsmatrix eingefügt werden müssen, um Inkonsistenzen zu vermeiden.

Die semi-implizite Lösungsprozedur geht Hand in Hand mit dem implementierten Druckkorrekturschema. Zur Berechnung der Stokes-Strömung in einer textilen Wiederholungszelle setzen wir für die Geschwindigkeiten periodische Randbedingungen und für den Druck periodische Randbedingungen in zwei Raumrichtungen und in der dritten einen konstanten Gradienten. Der fixierte Druckgradient treibt die Strömung an und muß daher auch im semi-impliziten Iterationsschritt der Impulsgleichung eingebunden werden.

Die Implementation von den Stokes Gleichungen, Darcys Gesetz und dem Einheitszellproblem in den Navier-Stokes Löser ist relativ geradlinig. Dagegen ist die Einfügung der Navier-Stokes/Brinkman Gleichungen um einiges komplizierter. Wie der diffusive Term wird der Brinkman-Term  $\mu \mathbf{K}_{\text{tow}}^{-1} \mathbf{u}$  implizit in der Zeit vorangetrieben, um weitere Zeitschrittweitenbeschränkungen hinsichtlich der Stabilität zu vermeiden. Wiederum wird das Crank-Nicolson Schema eingesetzt und die Lösung des linearen Gleichungssystems wie oben beschrieben fortgesetzt.

Permeabilitätsberechnungen können ungefähr fünfzehnfach schneller mit den beschriebenen Methoden ausgeführt werden als mit expliziten Zeitschrittmethoden. Dieser Geschwindigkeitsgewinn allein jedoch ist nicht ausreichend für die von Ingenieuren benötigte schnelle Permeabilitätsvorhersage. Deshalb werden die implementierten Löser durch Parallelisierung weiter beschleunigt. Wir validieren unsere Parallelisierungsstrategie durch Berechnung der Effizienz und der erreichten Beschleunigung, des sogenannten Speed-Ups, was exzellente Ergebnisse selbst für große Prozessorzahlen, die sehr kleine Bereiche behandeln, liefert. Da Textilien oft mehrlagig sind, zeigen wir außerdem, daß eine weitere Textilschicht sehr effizient durch entsprechende Steigerung der Prozessorzahl behandelt werden kann.

Diese Implementationen verlangen die folgenden Proben und Verifikationen:

- Numerische Äquivalenz zwischen der Lösung von Darcys Gesetz für die Permeabilität in einer Wiederholungszelle des porösen Mediums und der Lösung des Einheitszellproblems aus der Homogenisierungstheorie (theoretisch sollten beide dieselben Resultate zeigen).
- Vergleich der numerisch berechneten Permeabilität mit anderen semi-analytischen und numerischen Methoden (numerische Permeabilitätsberechnungen sind nur spärlich in der Literatur vertreten).
- Vergleich der direkten numerischen Simulation auf der Mikroskala mit der numerischen Lösung der homogenisierten Gleichungen und der Navier-Stokes/Brinkman

Gleichungen (da letztere lediglich eine Näherung der ersteren sind).

Mit den in dieser Arbeit vorgelegten Methoden bieten wir einen vereinheitlichten Ansatz für die theoretische, numerische und experimentelle Validierung der Berechnung von Permeabilitäten in Textilien:

- Wir legen die Homogenisierungstheorie und die dabei entstehenden Einheitszellprobleme dar.
- Wir erweitern Angots Theorie [12] dahingehend, daß sie auch auf Permeabilitätsberechnungen in Textilien angewandt werden kann.
- Wir erweitern den Strömungslöser NaSt3DGP, um Strömungsgleichungen in porösen Medien zu behandeln und diese Gleichungen schnell zu lösen.
- Wir prüfen die eingesetzten theoretischen und numerischen Verfahren durch experimentelle Daten.

Erste Anwendungen der oben beschriebenen Methoden auf echte textile Verstärkungsmaterialien wurden bereits von Verleye, Klitz, Croce et al. in [61, 60, 62] veröffentlicht und stellten eine substantielle Verbesserung im Bereich der akkuraten Permeabilitätsvorhersage für industrielle Problemstellungen dar.

## 1.7. Überblick

Die weitere Arbeit ist wie folgt strukturiert.

In Kapitel 2 diskutieren wir die inkompressiblen Navier-Stokes und Stokes Gleichungen. Wir verwenden dabei eine Reihe von Randbedingungen, so daß sich ein wohldefiniertes Anfangs-Randwertproblem ergibt. Außerdem werden Darcys Gesetz und die Brinkman Gleichungen als die zwei Filtrationsgesetze dargelegt, die auf der Makroskala eines porösen Mediums eingesetzt werden. Wir stellen kurz ihren empirischen Hintergrund vor und diskutieren ihre Verwendung in dieser Arbeit.

Als nächstes widmen wir uns der Herleitung der Strömungsgleichungen in periodischen porösen Medien. Dabei folgen wir [7, 31, 45, 53] bei der Homogenisierung der (Navier-) Stokes Gleichungen in Kapitel 3. Um die Unterschiedlichkeit der beiden Längenskalen, der Mikroskala  $\varepsilon$  der Poren und der Makroskala  $L$  des Reservoirs, zu überwinden, wird eine asymptotischen Entwicklung (1.2) der Funktionen  $(\mathbf{u}_\varepsilon, p_\varepsilon)$  postuliert, in welcher jede Funktion in der Reihe von Variablen beider Längenskalen abhängt.

A priori muß ein solcher Ansatz nicht zwangsläufig gelten. Daher ist in einem zweiten Schritt das homogenisierte Ergebnis einer Prüfung zu unterziehen, indem die Konvergenz von  $(\mathbf{u}_\varepsilon, p_\varepsilon)$  zur Lösung  $(\mathbf{u}, p)$  des homogenisierten Problems bewiesen wird. Dies wird mit der Zwei-Skalen-Konvergenzmethode nach Allaire [11] gezeigt. Die Zwei-Skalen-Konvergenzmethode ist maßgeschneidert für periodische Homogenisierung, was in diesem Zusammenhang für Geradlinigkeit in der Darstellung sorgt.

Wir konzentrieren uns auf die linearen Stokes Gleichungen, für die wir das Einheitszellproblem und Darcys Gesetz im Detail herleiten. In einem zweiten Teil des Kapitels geben

wir einen kurzen Überblick der Homogenisierungsergebnisse für die Navier-Stokes Gleichungen [45]. Der nichtlineare Term in den Navier-Stokes Gleichungen kann in einigen Fällen als kleine Störung der Stokes-Gleichungen betrachtet werden, was sehr ähnliche Ideen für Konvergenzbeweise zur Folge hat. Werden jedoch sehr kleine Viskositätswerte oder eine Variation der Viskosität mit  $\varepsilon$  zugelassen, so sind theoretische Resultate weitaus schwieriger zu gewinnen bzw. wurden bisher noch gar nicht erzielt [45]. In einem letzten Schritt folgen wir Allaire in [5] und zeigen, daß die Homogenisierungstheorie auch in zusammenhängenden Textilgebieten anwendbar ist.

In Kapitel 4 wird das duale Porositätsmodell diskutiert. Wir legen nach [12, 13, 33] die sogenannte Fictitious-Domain-Methode zur Modellierung viskoser Strömung in einem einzelnen Bereich, welcher leere, poröse und feste Medien einschließt, dar. Im gesamten Gebiet werden dabei lediglich die (Navier-)Stokes/Brinkman Gleichungen gelöst. Innerhalb des fiktiven Bereichs wird das spezielle Medium durch seine charakteristische Permeabilität beschrieben, d.h. durch einen endlichen Wert für poröse, durch einen unendlichen Wert für rein flüssige und den Wert Null für feste Bereiche. Zusätzlich kann die Viskosität von ihrem spezifischen Wert im rein flüssigen Bereich zu einem effektiven Wert im porösen Teil und zur Unendlichkeit im festen Bereich variieren. Dieser Ansatz der Fictitious-Domain-Methode vermeidet die explizite Formulierung der Bedingungen an den Grenzflächen der Medien.

Abschließend zu den oben genannten Betrachtungen des mathematischen Modells konzentrieren wir uns auf Fragen der Implementation der Navier-Stokes Gleichungen und der Strömungsgleichungen in porösen Medien in Kapitel 5. Nach einer kurzen Beschreibung des Navier-Stokes Löser NaSt3DGP [3] erläutern wir die Erweiterungen des Quellcodes, die für eine schnelle Permeabilitätsberechnung benötigt wurden. Eine wichtige Modifikation ist dabei die semi-implizite Lösung der Navier-Stokes Gleichungen, welche die Geschwindigkeit der Simulation bei niedrigen Reynoldszahlen beträchtlich erhöht. Im letzten Teil dieses Kapitels diskutieren wir dann eine Anzahl von numerischen Prüfsteinen des implementierten semi-impliziten Löser. Zum einen vergleichen wir unsere Ergebnisse mit den Ergebnissen von Ghia, Ghia und Shin [27] für den viel untersuchten Fall der sogenannten Nischenströmung, und zum anderen messen wir die Gesamtkonvergenzrate des Verfahrens und beispielhaft den Geschwindigkeitsgewinn zwischen implizitem und explizitem Zeitschrittverfahren.

Als nächstes haben wir die Berechnungen durch Parallelisierung weiter beschleunigt. Dabei wird auf eine Reduktion der Gesamtrechnenzeit abgezielt, indem die Arbeit auf verschiedene Prozessoren aufgeteilt wird, die die Berechnungen bis zu einem gewisse Grade gleichzeitig ausführen. Zusätzlich werden Speicheranforderungen unter den Prozessoren aufgeteilt. In Kapitel 6 werden mehrere Aspekte paralleler Implementierung für die Strömungssimulation thematisiert und sogenannte Speed-Up- und Scale-Up-Berechnungen angegeben. Wir erhalten noch immer eine Effizienz von ungefähr 95% bei Einteilung von  $60^3$  Gitterzellen auf 8 Prozessoren. Außerdem können zusätzliche Textilschichten sehr zeitsparend durch eine entsprechende Steigerung der Prozessorzahl behandelt werden.

Weiter wird in Kapitel 7 die Berechnung der Permeabilität in porösen Medien, die aus kubischen Anordnungen von Kugeln bestehen, überprüft. Im zweidimensionalen Fall werden unsere Berechnungen mit numerischen Permeabilitätslösungen von Neuss [48] und von Bang und Lukkassen [14] verglichen, wohingegen im dreidimensionalen Fall semi-analytische Permeabilitätsdaten von Sangani und Acrivos [54] zum Vergleich verfügbar sind. Zusätz-

lich lösen wir die Stokes Gleichungen auf der Mikroskala eines Mediums, das aus einem Teil reiner Flüssigkeit und einem porösen Teil besteht, und vergleichen das berechnete Geschwindigkeitsfeld mit der Lösung der Stokes/Brinkman Gleichungen.

Schließlich werden in Kapitel 8 die mathematischen und numerischen Betrachtungen auf Textilien angewandt. Wir stellen die existierende WiseTex [63] und LamTex Software für die Modellierung von Textilgeometrien vor und geben die Berechnung der Faserpermeabilität auf der textilen Mikroskala an. Diese semi-analytisch erhaltenen Permeabilitäten können auch numerisch durch die Lösung von Darcys Gesetz (1.3) berechnet werden, da Fasern in einem Textil als quadratische Anordnungen von Zylindern genähert werden. Zudem werden drei realistische Textilverstärkungen erörtert, deren Permeabilitätsvorhersagen mit experimentellen Daten verglichen werden. Man stellt fest, daß die Permeabilitäten, die durch unser numerisches Verfahren berechnet werden, äußerst gut mit denen der realen Experimente übereinstimmen.

Wir schließen diese Arbeit mit einer Zusammenfassung ihrer Ergebnisse und einer Darlegung der verschiedenen Möglichkeiten weiterer Forschung in Kapitel 9 ab.

# 1. Introduction

Flow simulations in porous media have a very wide range of environmental and industrial applicability. They are an important tool in fields such as ground water hydrology, civil engineering, petroleum production, ceramic engineering, the automotive industry and textile engineering. In many of these areas practical experiments are very time-consuming or even dangerous. Hence, numerical simulations are on their way to become the new standard for such experiments.

For instance, engineers simulate underground flow through porous rocks to predict the movement of contaminated fluid from solid waste landfills into drinking water supplies. In industrial applications, harmful particles can be filtered from a fluid stream by flow through a porous medium, whose small pores do not permit the passage of the larger particles. Additionally, simulations of flow in porous media can even help modelling tsunami interactions on a shore-line [2]: since it is computationally impossible to account for single trees, rocks, breakwaters and fortified dams in tsunami-prone regions, a more practical method is to consider such topographical variations as regions of porous media with given porosity and permeability.

Fluid flow models for such applications have to take into account multiple phases, thermal effects, as well as for example, chemical reactions. These can be described in addition or as an extension to the classical Navier-Stokes equations. For single-phase, isothermal, saturated flow of a Newtonian fluid, the Navier-Stokes equations in their incompressible formulation read

$$\begin{aligned} \rho \left[ \frac{\partial \mathbf{u}}{\partial t} + (\mathbf{u} \cdot \nabla) \mathbf{u} \right] + \nabla p &= \mu \Delta \mathbf{u} + \rho \mathbf{g} & \text{in } \Omega \times (0, T) \\ \nabla \cdot \mathbf{u} &= 0 & \text{in } \Omega \times (0, T), \end{aligned} \tag{1.1}$$

where  $\Omega$  denotes an open subset of  $\mathbb{R}^n$ ,  $\rho(\mathbf{x}, t) = \rho_\infty$  denotes the for incompressible fluids constant density and  $\mu$  the dynamic viscosity. Further, we have the velocity field  $\mathbf{u} : \Omega \times [0, T] \rightarrow \mathbb{R}^n$ , the pressure  $p : \Omega \times [0, T] \rightarrow \mathbb{R}$  and  $\mathbf{g}$  denotes volume forces such as gravity. The first equation states the conservation of momentum (momentum equation), the second equation states the conservation of mass (continuity equation).

However, the direct numerical simulation of fluid flow, by solving the Navier-Stokes equations (1.1) in the pore microstructure, is in many cases impossible - as a consequence of the hierarchical structure of porous media [45]. To understand this, we first need a general characterisation of such media.

## 1.1. A Definition of Porous Media

By a porous medium we mean a material consisting of a solid matrix with an interconnected void. We suppose that the solid matrix is either rigid (the usual situation) or it undergoes small deformation. The interconnectedness of the void (the pores) allows the flow of one or more fluids through the material.

*Donald A. Nield and Adrian Bejan [50, p.1]*

Following this definition, we can find many examples of natural as well as of synthetic porous media. Natural porous media take form as, for instance, beach sand, sandstone, limestone, rye bread, wood or the human lung. In these media the size and the distribution of the pores may be highly irregular. In contrast, synthetic porous media have in most cases a well-defined or even periodic structure, as for example wipes, diapers, paper machine clothings, activated carbon-filters, oil filters or diesel particulate filters. Thus, the periodic structure of a fabric repeat cell, for instance, is well-defined by the width and direction of its fibres (Fig. 1.1).

A typical characteristic of porous media is their porosity, which denotes the fraction of the total volume of the medium that is occupied by void space. For natural media the porosity does not normally exceed 0.6 [50]. Other common porosity values are 0.43 to 0.54 for soil, 0.02 to 0.07 for concrete or 0.17 to 0.49 for cigarette filters [50].

All porous media are characterised by at least two different length scales, introduced by the scale of the pores (microscale) and the scale of the mould or reservoir in which the porous medium is embedded (macroscale). Usually, both scales differ by several orders of magnitude. For example, the fabric cell depicted in Figure 1.1 is typically about 5mm small, as opposed to its manufactured fabric part which is about one hundred times larger. More so, groundwater flows are modelled in domains extending square kilometres, while the pore size of soil is less than 1mm.

These two or more largely varying length scales in a porous medium are what renders the direct numerical simulation of fluid flow time- and memory consuming: the required resolution of the pores' microstructure calls for very fine grids (and accordingly for very fine time steps), which draw heavily on the capacities of existing computer architectures. However, since the characteristic size of the solid fraction in a repeat cell of the medium is small compared to the whole sample, there are certain mathematical techniques that allow us to "average", "homogenise" or "upscale" the equations of fluid mechanics that hold on the microscale to laws on the macroscale, from which we hope that they are numerically easier to handle for simulation purposes. One of these techniques is homogenisation (cf. [7, 31, 45, 53]).

## 1.2. Homogenised Fluid Flow Equations in Porous Media

In homogenisation theory we try to overcome the discrepancy in both length scales by employing a multiscale expansion [45], which contains the behaviour of the fluid on the two

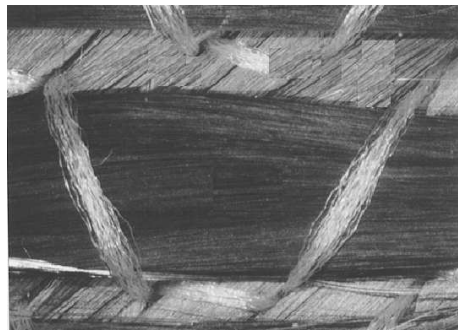


Fig. 1.1.: Example of a textile reinforcement's cell [picture: S.V. Lomov].

different length scales  $x$  and  $x/\varepsilon$

$$\mathbf{u}^\varepsilon = \varepsilon^\beta \left\{ \mathbf{u}_0 \left( \mathbf{x}, \frac{\mathbf{x}}{\varepsilon} \right) + \varepsilon \mathbf{u}_1 \left( \mathbf{x}, \frac{\mathbf{x}}{\varepsilon} \right) + \varepsilon^2 \mathbf{u}_2 \left( \mathbf{x}, \frac{\mathbf{x}}{\varepsilon} \right) + \dots \right\}. \quad (1.2)$$

Such an expansion for the velocity  $\mathbf{u}$  and the pressure  $p$  is inserted into the fluid equations (1.1) on the microscale, along with similar transformations of the operators  $\nabla$  and  $\Delta$ . In a next step, we study the limit  $\lim_{\varepsilon \rightarrow 0} \mathbf{u}_\varepsilon$ , which corresponds to letting the pore structure vanish. The basic idea behind this process is that the complicated microstructure averages out and that the partial differential equation obtained at the limit becomes numerically feasible, representing a so-called filtration law.

For instance, the homogenisation of the Navier-Stokes equations (1.1) for large constant viscosity  $\mu$  in periodic and random media yields Darcy's Law on the macroscale [7, 45, 53]

$$\langle \mathbf{u} \rangle = -\frac{1}{\mu} \mathbf{K} \cdot \nabla p \quad \text{in } \Omega, \quad (1.3)$$

where  $\langle \cdot \rangle$  denotes volume averaging and  $\mathbf{K}$  is the permeability tensor, which is a measure of the ability of a material to transmit fluids through it. This tensor is the only property in the homogenised equation, in which information about the complicated pore geometry is still kept. Darcy's law is valid for slow, viscous flow only, however, for instance most groundwater flow cases satisfy this assumption. Thus, we do not have to solve the Navier-Stokes equations in complicated rock and soil geometries, but instead the relatively simple linear equation (1.3). Nevertheless, a reliable numerical prediction of the unknown  $\mathbf{K}$  is absolutely necessary to enable practitioners to apply finite element or finite difference Darcy solvers for the numerical solution of flow through porous media [55, 59].

Works that are devoted to studying the permeability of porous media in general and of textiles in particular, can be divided into purely experimental approaches, purely theoretical ones, and works based on analytical approaches with elements of computational methods for the determination of permeability. Thus, as Mei, Auriault and Ng [42] point out, "there are many more theoretical papers applying the method of homogenisation [...] than there are quantitative solutions of the cell problems".

Hence, the theory of homogenisation is well accounted for in literature (cf. [7, 31, 45, 53]

and the reference therein), but the numerical application and discussion of the derived formulas is scarce [34, 47, 52]. Contrary, there are a vast number of purely heuristic approaches for the computation of permeability [49], where filtration laws like Darcy's are successfully applied without further ado about their applicability for the particular problem.

Therefore, in this thesis, we address the two points lacking most in theoretical as well as applied literature on the topic of homogenisation:

1. We discuss for which particular problems the different homogenised equations are valid.
2. We solve the resulting equations numerically for the prediction of the permeability  $\mathbf{K}$ .

As an example of the restricted relevance of some homogenised equations, let us consider a further possible equation to be obtained at the homogenisation limit of the same Navier-Stokes equations (1.1), namely the Brinkman equations [7, 45]

$$\begin{aligned} \nabla p - \mu \Delta \mathbf{u} + \frac{\mu}{\sigma^2} \mathbf{M} \mathbf{u} &= f & \text{in } \Omega \\ \nabla \cdot \mathbf{u} &= 0 & \text{in } \Omega \\ \mathbf{u} &= 0 & \text{on } \partial\Omega. \end{aligned} \tag{1.4}$$

Here,  $\sigma$  denotes some ratio of solid fractions in the porous medium, and  $\mathbf{M}$  a permeability defined very differently than  $\mathbf{K}$  in Darcy's Law. Note, that both these filtration laws are obtained in the same media from the same equations, just assuming a different scaling of the solid/fluid fraction only.

However, by a discussion of scales following [34], we find that the Brinkman equations (1.4) should be employed for media with a very high porosity only, i.e. a porosity extremely close to one. Hence, this equation is neither applicable for natural media, nor for textiles, whereas, for instance, it is found to apply for rigid foams of porosity 0.972 [50]. Such considerations are scarcely found in theoretical works about homogenisation theory.

Coming back to Darcy's Law (1.3), we now want to see how the permeability  $\mathbf{K}$  can be determined numerically.

### 1.3. Numerical Prediction of the Permeability $\mathbf{K}$ in Darcy's Law

Besides its applicability for flow simulation on the macroscale, Darcy's Law itself can be seen as a definition of permeability [18, 26, 49, 61]. Thus, we can determine the flow in a single repeat cell, if the porous medium has a periodic pattern. In this cell, we compute the Navier-Stokes equations (1.1) and use the computed velocity field  $\mathbf{u}$  and the pressure  $p$  as input for Darcy's Law at steady state. Hence, we merely have to solve equations (1.1) in a single cell, as opposed to their solution in the whole porous medium before.

Nevertheless, homogenisation theory offers another (ultimately easier to evaluate) defi-

dition of the permeability tensor [45, 53] in  $n$  dimensions

$$K_{ij} = \int_{Y_F} \nabla_y \mathbf{w}^i \nabla_y \mathbf{w}^j dy \text{ for } 1 \leq i, j \leq n. \quad (1.5)$$

Here,  $\mathbf{w}^i$  for  $1 \leq i \leq n$  denote the solutions of the so-called Unit Cell Problems: for  $1 \leq i, j \leq n$  find  $(\mathbf{w}^i, \pi^i) \in H_{\text{per}}^1(Y)^n \times L^2(Y)$  such that

$$\begin{aligned} -\Delta \mathbf{w}^i + \nabla \pi^i &= \mathbf{e}^i & \text{in } Y_F \\ \nabla \cdot \mathbf{w}^i &= 0 & \text{in } Y_F \\ \mathbf{w}^i &= 0 & \text{on } \partial Y_F \setminus \partial Y \\ \mathbf{w}^i, \pi^i & & Y - \text{periodic,} \end{aligned} \quad (1.6)$$

where  $\mathbf{e}^i$  denotes the vector with components  $e_j^i = \delta_{ij}$ ,  $y \in Y$ ,  $Y$  a unit cell of the porous medium,  $Y_F$  and  $Y_S$  its corresponding fluid and solid parts and  $H_{\text{per}}^1(Y)^n$  denotes the Sobolev space  $H^{1,2}(Y)^n$  restricted to  $Y$ -periodic functions. Furthermore,  $(\mathbf{w}^i, \pi^i)$  are comparable to the fluid velocity and the pressure in the Stokes equations (the linearised form of the Navier-Stokes equations (1.1)). Thus, the solution of the cell problems in 3D amounts to the solution of three Stokes equations with external forces  $(\mathbf{e}^i)_{1 \leq i \leq 3}$ , from which we obtain  $(\mathbf{w}^i)_{1 \leq i \leq 3}$  for the input into  $\mathbf{K}$ . This leads to the same results as the computation of the permeability  $\mathbf{K}$  by Darcy's Law since in the unit repeat cell these are equivalent problems [53].

## 1.4. A Dual Porosity Model

If we have to account for another length scale in a porous medium, i.e. if the solid fraction of the porous matrix is porous itself, we employ the Navier-Stokes/Brinkman equations

$$\begin{aligned} \rho \left[ \frac{\partial \mathbf{u}}{\partial t} + (\mathbf{u} \cdot \nabla) \mathbf{u} \right] + \nabla p + \mu \mathbf{K}_{\text{tow}}^{-1} \mathbf{u} &= \mu \Delta \mathbf{u} & \text{in } \Omega \\ \nabla \cdot \mathbf{u} &= 0 & \text{in } \Omega, \end{aligned} \quad (1.7)$$

where  $\mathbf{K}_{\text{tow}}$  denotes the permeability on the smallest scale. The Brinkman equations are a practical method to describe coupled flow problems in plain and porous media [33], since Angot [13] showed that these equations can be used without explicit interface conditions. Thus, the additional term  $\nu \mathbf{K}_{\text{tow}}^{-1} \mathbf{u}$  is a penalisation of the Navier-Stokes equations (1.1), in that equation (1.7) converges to equation (1.1) for large  $\|\mathbf{K}_{\text{tow}}\|$ , and is a Brinkman type equation with its specific permeability in the porous part. Furthermore, since this specific permeability  $\|\mathbf{K}_{\text{tow}}\|$  is usually small ( $10^{-4} \text{mm} \leq \|\mathbf{K}\|_{\text{max}} \leq 10^{-7} \text{mm}$  for textiles), the term  $\mu \mathbf{K}_{\text{tow}}^{-1} \mathbf{u}$  can be expected to dominate over the viscous and convective term,  $\mu \Delta \mathbf{u}$  and  $(\mathbf{u} \cdot \nabla) \mathbf{u}$ , and hence, satisfies again Darcy's Law (1.3) in the porous medium.

These equations should not be confused with the Brinkman equations (1.4) in homogenisation theory, since equation (1.7) is not a homogenised equation, and the permeabilities in both equations differ: in the porous region  $\mathbf{K}_{\text{tow}}$  is effectively a Darcy permeability

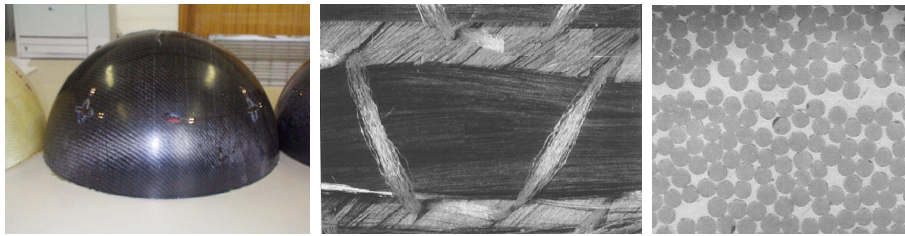


Fig. 1.2.: Scales in textile reinforcements: the macroscale of the fabric part ( $\approx 1\text{m}$ ), the mesoscale of the textile repeat cell ( $\approx 0.01\text{m}$ ) and the microscale of the fibres ( $\approx 0.0001\text{m}$ ) [picture: S.V. Lomov].

defined by (1.5), since we want the Navier-Stokes/Brinkman equations to satisfy Darcy's Law there.

## 1.5. Application to Permeability Computations in Textiles

One of the main aims of this thesis is the prediction of textile permeability. Fast prediction of permeability is invaluable for the modelling of fluid flow in textiles. An important example for its applicability is Liquid Composite Moulding (LCM) for the manufacturing of composites with textile reinforcements. One of the LCM techniques is Resin Transfer Moulding (RTM), which is the low-pressure injection of resin into a closed cavity filled with fibre preforms. In these fibre preforms the numerical computation of fluid flow aims at the enhancement of resin flow through the fibre preform to reduce voids, bubbles and injection time. The existing tools that simulate the injection stage of Resin Transfer Moulding like PAM-RTM or LIMS [55, 59] require the permeability at different positions in the preform model.

The calculation of permeability presumes a thorough characterisation of the textile reinforcement, which is provided by the WiseTex software [63] developed at the Katholieke Universiteit Leuven in Belgium. In cooperation with the Composite Materials and the Scientific Computing research group in Leuven we are developing a new module for their software package FlowTex for the computation of the permeability of textile reinforcements. This module is based on the freely available flow solver NaSt3DGP [3], a CFD package which is developed at the Institute of Numerical Simulation in the research group of Prof. Michael Griebel [28].

Textiles are special porous media, meeting us with the following simplifications and challenges:

- Textiles are periodic, connected porous media.
- Flow through textiles is strongly laminar.
- Yarns in a textile can be porous themselves, introducing a further scale into our model (Fig. 1.2).

- Textiles have fairly complicated structures even in a unit cell setup (Fig. 1.1) and are often multilayered.
- Textile engineers require the permeability at different positions in the preform model, which presumes its fast computation.

Since textiles have a periodic pattern we focus on periodic porous media in this thesis, and we approximate the textile matrix by assuming that it does not allow for deformations. Furthermore, homogenisation theory can be shown to hold in the connected textile domain [5]. Hence, the computation of permeability is conducted in a unit cell of the fabric structure (Fig. 1.1) by either solving the Unit Cell Problem (1.6) or Darcy’s Law (1.3).

We investigate one-phase Newtonian flow through the textiles’ pores, which is in principle modelled by the incompressible Navier-Stokes equations (1.1). The fluid’s internal resistance to flow is measured by the viscosity  $\mu$ . Introducing the dimensionless Reynolds number  $\text{Re} \equiv \rho_\infty u_\infty L / \mu$ , with  $L$  and  $u_\infty$  some characteristic scalar constants, we have a measure of the relative magnitude of inertial and viscous forces. In Resin Transfer Moulding velocities are typically of  $10^{-3}$  m/s, and the Reynolds number is about 0.05 [55, 59]. In this regime, flow is strongly laminar, and we show that for the applied forces flow is sufficiently described by the linear Stokes equations.

The hierarchical structure of textiles introduces a further scale into our considerations (Fig. 1.2). The fabric in the repeat cell of the reinforcement is made of porous yarns which consist of fibres. Thus, our model for fluid flow must account for the porosity on two different length scales, which leads to the mathematical problem of interface conditions between a pure fluid region and a porous region. Then, flow is described by the Navier-Stokes/Brinkman equations (1.7) or their linearised counterpart, the Stokes/Brinkman equations.

This approach explicitly avoids interface conditions and is mathematically justified by Angot in [12] for the linear case and by Angot, Bruneau and Fabrie in [13] for the nonlinear case. Thus, Angot introduces an error estimate for the solution of the Stokes/Brinkman equations compared to the solutions of the Brinkman equations and the Stokes equations with continuous stress and velocity as interface conditions - for scalar permeabilities. In this thesis we formulate a straightforward extension of this error estimate to the case that the permeability is a diagonal, positive definite, second-order tensor, since textile microscale permeabilities are of such form.

Moreover, the yarn permeability  $\mathbf{K}_{\text{tow}}$  has to be computed. Such a computation is already implemented in the FlowTex software, based on semi-analytical formulas by Berdichevsky and Cai [18] and by Gebart [26].

To meet all of the above mentioned aspects, a variety of numerical methods based on the Navier-Stokes solver NaSt3DGP [3] were implemented.

## 1.6. Numerical Methodology

The three-dimensional Navier-Stokes solver NaSt3DGP [3] works completely in parallel and offers a good basis for modifications and extensions necessary for fast permeability computations.

NaSt3DGP employs a projection method pioneered by Chorin [20], which is among the most common numerical approaches for the solution of the Navier-Stokes equations: first, the momentum equations are advanced to give an approximation of the velocity  $\mathbf{u}$  or some provisional velocity field  $\mathbf{u}^*$ . Then, an elliptic equation is solved that enforces the divergence constraint,  $\nabla \cdot \mathbf{u} = 0$ , and determines the pressure.

The momentum equations are advanced explicitly in time by Euler or Adams-Bashforth integration, which yields a time-step restriction for the convective terms, as well as for the diffusive terms and for volume forces. This restriction guarantees the numerical stability of the solution procedure.

However, in the low Reynolds number regime, the stability constraint for the diffusive terms of the Navier-Stokes equations is much more restrictive than the condition for the convective terms. Thus, we discretise the diffusive terms implicitly in time by a Crank-Nicolson scheme, and leave the convective terms explicitly. This amounts to a so-called semi-implicit scheme for the Navier-Stokes equations and is fully implicit for the Stokes equations.

The Navier-Stokes equations (1.1) are solved numerically on a regular staggered grid with a finite volume discretisation. In the staggered grid approach, the pressure is discretised at the centre of the cells, while the velocities are discretised on the cell sides. This discretisation leads to a strong coupling between pressure and velocities, and therefore avoids the occurrence of unphysical oscillations in the pressure.

All in all, the following modifications of the code had to be performed:

- A pressure correction method [15] was implemented, along with a semi-implicit solution algorithm of the Navier-Stokes equations [19].
- The Navier-Stokes/Brinkman equations (1.7) were implemented and are solved semi-implicitly in time.
- The above algorithms were extended to solve the Stokes and Stokes/Brinkman equations implicitly in time.
- Darcy's Law (1.3) and the Unit Cell Problems (1.6) were implemented.
- All of the above implementations were parallelised.

One of the many challenges arising with a (semi-)implicit implementation is the solution of three further linear systems of equations for the three provisional velocity components  $(u^*, v^*, w^*)$ . After some tests, we opted for an iterative Conjugate Gradient method with Symmetric Successive Overrelaxation (SSOR) preconditioning. The most demanding implementational issues are the various possible boundary conditions for  $(u^*, v^*, w^*)$ , which have to be included by manipulations in the solution matrix to avoid inconsistencies.

The semi-implicit solution procedure goes hand in hand with the implemented pressure correction scheme. For the computation of Stokes flow in a textile repeat cell, we set periodic boundaries for the velocities and also for the pressure, except for one direction, in which we specify a constant pressure gradient. Thus, flow is driven by this fixed pressure gradient, and has to be included in the semi-implicit advancement of the momentum equations.

The implementation of the Stokes equations, Darcy’s Law and the Unit Cell Problems into the Navier-Stokes solver is fairly straightforward. However, the implementation of Navier-Stokes/Brinkman equations is an entirely different matter. Like the diffusive term, the Brinkman term  $\mu \mathbf{K}_{\text{tow}}^{-1} \mathbf{u}$  has to be transported implicitly in time to avoid further time-step restrictions by stability considerations. Again, the Crank-Nicolson scheme is employed, and the solution of the linear system of equations proceeds as mentioned before.

Permeability computations can be conducted about fifteen times faster with the above described methods than by explicit time stepping. This speed-up alone, however, is not sufficient for the fast permeability prediction needed by engineers. Therefore, we fasten our implemented fluid flow and porous media solver further by parallelisation. We back our parallelisation strategy by efficiency and speed-up computations, which show excellent results even for large numbers of processors treating very small domains. Furthermore, since textiles are often multilayered, we show that another textile layer can be handled very efficiently by a respective increase in the number of processors.

These implementations demand the following validations and verifications:

- Numerical equivalence of solving Darcy’s Law for the permeability in a repeat cell of the porous medium and to solve the Unit Cell Problem arising from homogenisation theory (theoretically, they should give the same results).
- Comparison of the numerically computed permeability with other semi-analytical and numerical methods (numerical computation of permeability is scarce in literature).
- Comparison of direct numerical simulation on the microscale as opposed to the numerical solution of homogenised equations and of the Navier-Stokes/Brinkman equations (since the latter are merely an approximation of the first).

With the presented methods in this thesis, we offer a unified approach of theoretical, numerical and experimental validation for the computation of textile permeabilities:

- We present homogenisation theory and the resulting Unit Cell Problems.
- We extend Angot’s theory [12] to a level applicable to permeability computations in textiles.
- We extend the flow solver NaSt3DGP to handle porous media flow equations and to solve these equations fast.
- We validate the employed theoretical and numerical approaches by experimental data.

Note, that first applications of the methods developed in this thesis for real-world manufactured textile reinforcements have already been published by Verleye, Klitz, Croce et al. in [60, 61, 62], and have provided a substantial improvement in accurate permeability predictions for industrial requisitions.

## 1.7. Thesis Outline

The remainder of this thesis is structured as follows.

In Chapter 2 we discuss the incompressible Navier-Stokes and Stokes equations. We

adjust a variety of boundary conditions to these equations, so that a well-defined initial boundary value problem results. Furthermore, we present Darcy’s Law and Brinkman’s equations as the two filtration laws that we employ on the macroscale of a porous medium. We shortly give their empirical background and discuss their use in this thesis.

Next, we are devoted to the derivation of flow equations in periodic porous media. Thus, in Chapter 3, we follow [7, 31, 45, 53] in the homogenisation of the (Navier-)Stokes equations. In order to overcome the disparity of the two length scales, the microscale  $\varepsilon$  of the pores and the macroscopic scale  $L$  of the reservoir, an asymptotic expansion (1.2) of the functions  $(\mathbf{u}_\varepsilon, p_\varepsilon)$  is postulated, in which each function in the series depends on variables of both length scales.

A priori there is no reason for this ansatz to hold true. Thus, in a second step, the homogenised result has to be justified by proving the convergence of  $(\mathbf{u}_\varepsilon, p_\varepsilon)$  to the solution  $(\mathbf{u}, p)$  of the homogenised problem, which we show by the two-scale convergence method following Allaire [11]. The two-scale convergence method is dedicated to specifically periodic homogenisation, which makes it very efficient and straightforward in this context.

We focus on the linear Stokes equations, for which we derive the Unit Cell Problem and Darcy’s Law in detail. In a second part of the chapter we carry out a brief survey of homogenisation results for the Navier-Stokes equations [45]. The nonlinear term in the Navier-Stokes equations can in some cases be seen as a small perturbation of the Stokes equations which results in very similar ideas for convergence proofs. However, as soon as we allow the viscosity to take very small values or to vary with  $\varepsilon$ , theoretical results are more difficult to obtain or have not yet been obtained at all [45]. In a last step we show that homogenisation theory is applicable in the connected textile domain following [5].

In Chapter 4 we discuss the dual porosity model. We present the fictitious domain method for the modeling of viscous flow in a single domain which embeds plain, porous and solid media following [12, 13, 33]. The whole domain is governed by a single set of the (Navier-)Stokes/Brinkman equations. Within the fictitious domain the particular medium is taken into account by its characteristic permeability, that is, by a finite value for porous, by an infinite value for pure fluid and by zero for pure solid domains. In addition, the viscosity may vary from its specific value in the pure fluid domain, to some effective value in the porous part and up to infinity in the solid domain. This fictitious domain approach avoids the explicit expression of the transmission conditions at the interface of the different media.

In conclusion of the above considerations concerning the mathematical model, we focus on the implementational issues of the Navier-Stokes and of the porous media flow equations in Chapter 5. After a short presentation of the Navier-Stokes solver NaSt3DGP [3], we describe the extensions to the code that are necessary for fast permeability computations. One important modification is the semi-implicit solution of the Navier-Stokes equations, which fastens the speed of simulations in the low Reynolds number regime considerably.

Thus, in a last part of the chapter, we discuss a number of numerical validation aspects of the implemented semi-implicit solver. First, we compare our results to results obtained by Ghia, Ghia and Shin [27] for the well-studied lid-driven Cavity problem. Second, we measure the overall convergence rate of the scheme and third, exemplify the speed up of implicit compared to explicit time stepping.

We have accelerated our computations further by parallelisation, with which we aim at

a reduction of the total computing time by dividing the work between several processors, which perform their computations to a certain extent simultaneously. In addition, memory requirements will be divided between the processors. In Chapter 6 we address a number of parallel implementation aspects for our flow simulation model, and give speed-up and scale-up calculations. We still obtain an efficiency of about 95% when dividing  $60^3$  grid cells on 8 processors. Further, additional textile layers can be handled very time savingly by a respective increase in the number of processors.

Furthermore, in Chapter 7, we validate computations of the permeability in porous media consisting of cubic arrays of spheres. In the two-dimensional case we compare our computations to numerical permeability solutions by Neuss [48] and by Bang and Lukkassen [14], whereas in the three-dimensional case semi-analytical permeability data by Sangani and Acrivos [54] is available for comparison. In addition, we solve the Stokes equations on the microscale of a medium consisting of a pure fluid and a porous part and compare the computed velocity field to the solution of the Stokes/Brinkman equations.

Finally, in Chapter 8, we apply our mathematical and numerical considerations on textiles. We present the existing WiseTex [63] and LamTex software for the modeling of textile geometries and provide an insight into the computation of the yarn's permeability on the textile microscale. These semi-analytically computed permeabilities can also be computed numerically by the solution of Darcy's Law (1.3), since yarns in a textile are approximated as square arrays of cylinders. In addition, we present three realistic types of textile reinforcements and compare permeability computations to experimental data. The permeabilities, predicted by our numerical scheme, coincide extremely well with those of real experiments.

We conclude this thesis by a summary of its results and a presentation of the various possibilities for further research in Chapter 9.



## 2. The Mathematical Model

For the modelling of flow in porous media we consider up to three scales, i.e. the macroscale, the mesoscale and the microscale (Fig. 2.1). The third scale has to be considered, if dual porosity of a medium has to be taken into account, like for example, porous fibres in a porous textile.

We aim at the computation of permeability for the insertion into filtration equations, like Darcy's Law, that describe flow on the macroscale. On the one hand, if the pores on the mesoscale are rigid, we compute the Stokes or Navier-Stokes equations and insert the computed velocity field  $\mathbf{u}$  and the pressure  $p$  into Darcy's Law for the calculation of the permeability  $\mathbf{K}$ . In this case, a further possibility is to compute the permeability via the Unit Cell Problems, of which we show in homogenisation theory that it is equivalent to Darcy's Law. On the other hand, if the pores are porous themselves, we compute the Navier-Stokes/Brinkman or Stokes/Brinkman equations on the mesoscale, and again, insert  $\mathbf{u}$  and  $p$  into Darcy's Law for the computation of  $\mathbf{K}$ . These equations are of such form that they reduce to the standard fluid flow equations in the pure fluid regime of the mesoscale and are of Darcy type in the porous part.

In this chapter we discuss the incompressible Navier-Stokes and Stokes equations which describe one-phase Newtonian flow through the media's pores. We adjust a variety of boundary conditions to these equations, so that a well-defined initial boundary value problem results. Furthermore, we present Darcy's Law and Brinkman's equations as the two filtration laws that we employ on the mesoscale of a porous medium. We shortly give their empirical background and discuss their use in this thesis.

### 2.1. The Navier-Stokes Equations

Let  $\Omega$  denote an open subset of  $\mathbb{R}^n$ . For  $\mathbf{x} \in \Omega$  and time  $t \geq 0$  the time-dependent incompressible Navier-Stokes equations read

$$\begin{aligned} \rho \left[ \frac{\partial \mathbf{u}}{\partial t} + (\mathbf{u} \cdot \nabla) \mathbf{u} \right] + \nabla p &= \mu \Delta \mathbf{u} + \rho \mathbf{g} & \text{in } \Omega \times (0, T) \\ \nabla \cdot \mathbf{u} &= 0 & \text{in } \Omega \times (0, T), \end{aligned} \quad (2.1)$$

where  $\rho(\mathbf{x}, t) = \rho_\infty$  denotes the for incompressible fluids constant density,  $\mathbf{u} : \Omega \times [0, T] \rightarrow \mathbb{R}^n$  denotes the velocity field and  $p : \Omega \times [0, T] \rightarrow \mathbb{R}$  the pressure. The fluid's dynamic viscosity  $\mu$  can be replaced by its kinematic counterpart  $\nu \equiv \mu/\rho_\infty$  if we divide equation (2.1) by  $\rho_\infty$

$$\begin{aligned} \frac{\partial \mathbf{u}}{\partial t} + (\mathbf{u} \cdot \nabla) \mathbf{u} + \frac{1}{\rho_\infty} \nabla p &= \nu \Delta \mathbf{u} + \mathbf{g} & \text{in } \Omega \times (0, T) \\ \nabla \cdot \mathbf{u} &= 0 & \text{in } \Omega \times (0, T). \end{aligned} \quad (2.2)$$

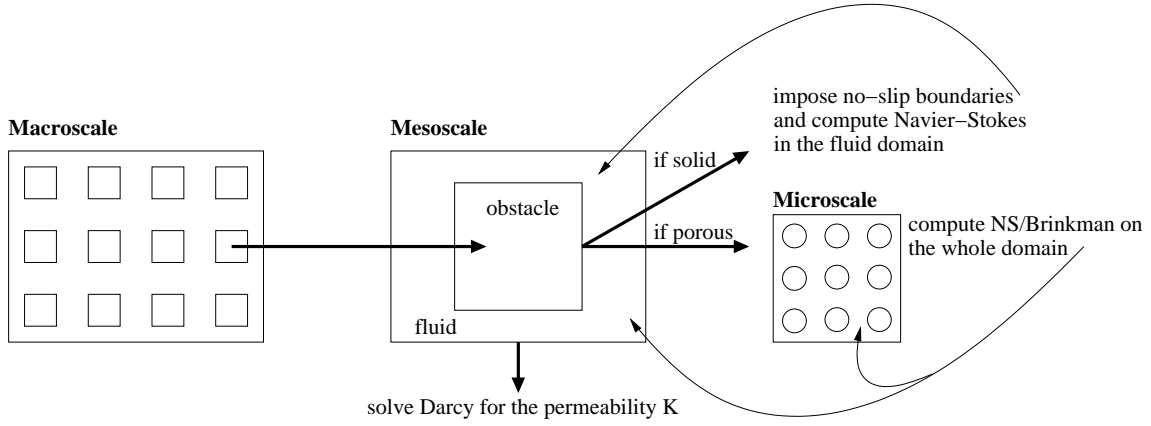


Fig. 2.1.: The interplay of flow equations in the hierarchy of porous media scales.

Since it is often necessary to describe large scale physical experiments in numerically feasible settings [28], the above equations are often studied in their dimensionless variables

$$\mathbf{u}^* \equiv \frac{\mathbf{u}}{u_\infty}, \quad \mathbf{x}^* \equiv \frac{\mathbf{x}}{L}, \quad t^* \equiv \frac{u_\infty t}{L}, \quad p^* \equiv \frac{p - p_\infty}{\rho_\infty u_\infty^2}$$

with scalar constants  $L$ ,  $u_\infty$ ,  $p_\infty$  and  $\rho_\infty$ . Substitution of these variables into (2.2) leads to

$$\begin{aligned} \frac{\partial (u_\infty \mathbf{u}^*)}{\partial \left( \frac{t^* L}{u_\infty} \right)} + \left( u_\infty \mathbf{u}^* \cdot \frac{1}{L} \nabla^* \right) u_\infty \mathbf{u}^* + \frac{\rho_\infty u_\infty^2}{\rho_\infty L} \nabla^* p^* &= \frac{\nu}{L^2} \Delta^* u_\infty \mathbf{u}^* + \mathbf{g} \\ \Leftrightarrow \frac{\partial \mathbf{u}^*}{\partial t^*} + (\mathbf{u}^* \cdot \nabla^*) \mathbf{u}^* + \nabla^* p^* &= \frac{\nu}{u_\infty L} \Delta^* \mathbf{u}^* + \frac{L}{u_\infty^2} \mathbf{g} \end{aligned}$$

and

$$\nabla^* \cdot \mathbf{u}^* = 0,$$

in which the operators  $\nabla^*$  and  $\Delta^*$  now refer to  $\mathbf{x}^*$ . Information on the flow is contained in its characteristic parameters such as the dynamic viscosity  $\mu$ , values for the length  $L$ , the velocity  $u_\infty$  and the density  $\rho_\infty$ . All of these parameters are now grouped on the left hand side of the above equation, so that two flows will behave similar if these parameter groupings coincide. Thus, we introduce the Reynolds and Froude number

$$\text{Re} \equiv \frac{u_\infty L}{\nu} = \frac{\rho_\infty u_\infty L}{\mu} \quad \text{and} \quad \text{Fr} \equiv \frac{u_\infty^2}{L \|\mathbf{g}\|},$$

which summarise the parameters in two further dimensionless quantities. The Reynolds number represents the relative magnitude of inertial and viscous forces, whereas the Froude number denotes the ratio of inertial to gravitational forces. We conclude that flows in similar geometries are dynamically similar, if they have the same Reynolds and Froude number

[28]. Furthermore, introducing the dimensionless body force  $\mathbf{g}^* \equiv \mathbf{g}/\|\mathbf{g}\|$ , we finally obtain the Navier-Stokes equations

$$\begin{aligned} \frac{\partial \mathbf{u}^*}{\partial t^*} + (\mathbf{u}^* \cdot \nabla^*) \mathbf{u}^* + \nabla^* p^* &= \frac{1}{\text{Re}} \Delta \mathbf{u}^* + \frac{1}{\text{Fr}} \mathbf{g}^* & \text{in } \Omega \times (0, T) \\ \nabla^* \cdot \mathbf{u}^* &= 0 & \text{in } \Omega \times (0, T) \end{aligned} \quad (2.3)$$

in dimensionless formulation.

### 2.1.1. The Stokes Equations

We show numerically that the convective terms in the Navier-Stokes equations are small as opposed to the discretisation error in the geometries and for the external forces considered in this thesis. That is why we foremost use the linearised Navier-Stokes equations for creeping flows, namely the Stokes equations

$$\begin{aligned} \rho \frac{\partial \mathbf{u}}{\partial t} + \nabla p &= \mu \Delta \mathbf{u} + \rho \mathbf{g} & \text{in } \Omega \times (0, T) \\ \nabla \cdot \mathbf{u} &= 0 & \text{in } \Omega \times (0, T). \end{aligned} \quad (2.4)$$

In dimensionless notation they satisfy

$$\begin{aligned} \frac{\partial \mathbf{u}^*}{\partial t^*} + \nabla^* p^* &= \frac{1}{\text{Re}} \Delta^* \mathbf{u}^* + \frac{1}{\text{Fr}} \mathbf{g}^* & \text{in } \Omega \times (0, T) \\ \nabla^* \cdot \mathbf{u}^* &= 0 & \text{in } \Omega \times (0, T). \end{aligned} \quad (2.5)$$

### 2.1.2. Boundary Conditions

At  $t = 0$  we impose initial conditions on the velocity  $\mathbf{u}$  which satisfy the continuity equation of the (Navier-)Stokes equations. In addition, conditions on the domain's boundary  $\Gamma = \partial\Omega$  are required, so that a well-defined initial boundary value problem results [28]. Let  $\mathbf{u} \cdot \boldsymbol{\nu}$  denote the component of the velocity orthogonal to the boundary,  $\mathbf{u} \cdot \boldsymbol{\tau}$  the component of the velocity tangential to the boundary and  $\partial \mathbf{u} / \partial \boldsymbol{\nu}$  the velocity's derivative in normal direction. We consider the following boundary conditions:

**No-Slip Condition:** The fluid adheres to the boundary, and no fluid penetrates the boundary. Hence the velocity vector has to vanish there

$$\mathbf{u}|_{\Gamma} = 0.$$

**Slip Condition:** Again, no fluid penetrates the boundary, but as opposed to the no-slip condition, there are no friction losses at the boundary, i.e.

$$\mathbf{u} \cdot \boldsymbol{\nu}|_{\Gamma} = 0 \quad \partial_{\boldsymbol{\nu}}(\mathbf{u} \cdot \boldsymbol{\tau})|_{\Gamma} = 0.$$

**In/Outflow Condition:** A fixed velocity  $\mathbf{u}_0$  is given for both components, i.e.

$$\mathbf{u}|_{\Gamma} = \mathbf{u}_0.$$

**Natural Outflow Condition:** The fluid velocity does not change in the normal direction of the boundary

$$(\partial_{\nu}\mathbf{u})|_{\Gamma} = 0.$$

**Periodic Boundary Condition:** For periodic problems along one or more coordinate directions the velocities and pressure values must coincide at opposite boundaries.

Following Gauss' Theorem, we note that the velocity on the boundaries has to fulfil the restriction

$$0 = \int_{\Omega} \nabla \cdot \mathbf{u} \, dx = \int_{\Gamma} \mathbf{u} \cdot \boldsymbol{\nu} \, d\Gamma,$$

that is, the boundary integral of the normal components of the given velocities must vanish. This conditions imposes a restriction if the velocities, rather than their normal derivatives, are given along the entire boundary.

## 2.2. Darcy's Law

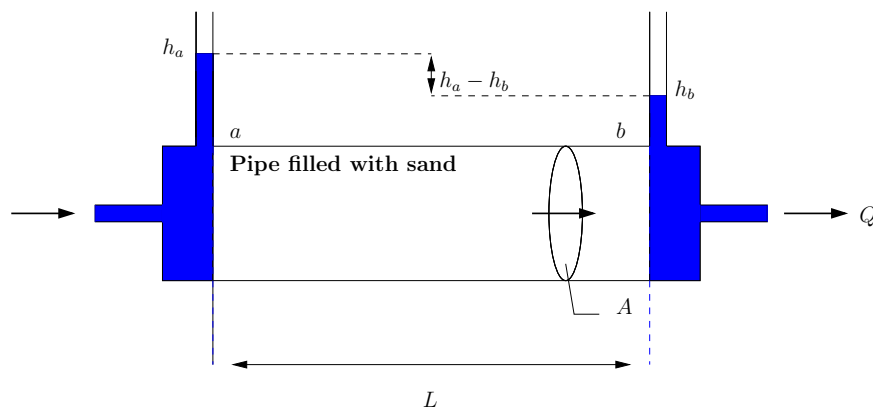


Fig. 2.2.: Darcy's experiment.

In 1856, Henry Darcy investigated the flow of water in sand filters for the fountains of the city of Dijon. From his experiments (Fig. 2.2) he concluded that the flow rate  $Q$  is proportional to the constant cross-sectional area  $A$ , to the difference in the hydraulic head  $h_a - h_b$  and inversely proportional to the length  $L$  of the specimen [1]. These relations form the famous equation that today still bears his name

$$Q = kA \frac{(h_a - h_b)}{L}, \quad (2.6)$$

Darcy's Law. In this equation  $k$  denotes the hydraulic conductivity which is related to the permeability  $K$  by

$$k = \frac{K\rho g}{\mu}.$$

Further, for constant fluid density, the hydraulic head  $h$  represents the total energy per unit weight of the fluid and consists of the pressure head  $p/\rho g$  and the elevation head  $z$ , which denotes the elevation of the bottom of the measuring point above sea level. Hence,

$$h = \frac{p}{\rho g} + z.$$

Substitution of the above properties into Darcy's Law (2.6) yields

$$Q = kA \frac{(h_a - h_b)}{L} = \frac{KA\rho g}{\mu} \left[ \frac{p_a - p_b}{L\rho g} + \frac{z_a - z_b}{L} \right] = \frac{KA}{\mu} \left[ \frac{p_a - p_b}{L} + \rho g \frac{z_a - z_b}{L} \right].$$

Foremost, we will use Darcy's Law without the inclusion of volume forces. Furthermore, we introduce the effective (seepage or filtration) velocity, which is the discharge per unit gross area of the porous medium and represents all the impossible to measure individual velocities throughout the porous medium. Then we write

$$q = \frac{Q}{A} = \frac{K}{\mu} \frac{p_a - p_b}{L},$$

or in differential formulation

$$q = -\frac{K}{\mu} \frac{dp}{dx}.$$

### 2.2.1. Non-Dimensional Formulation of Darcy's Law

In three dimensions the discharge  $\mathbf{q}$  and the pressure gradient are vectors, and the permeability is a second-order tensor. Then Darcy's Law reads

$$\mathbf{q} = -\frac{\mathbf{K}}{\mu} \nabla p.$$

Introducing the dimensionless notation for this equation

$$\begin{aligned} \mathbf{q}^* u_\infty &= -\frac{\mathbf{K} \text{Re}}{\rho_\infty u_\infty L} \nabla (p^* \rho_\infty u_\infty^2 + p_\infty) \\ &= -\frac{\mathbf{K} \text{Re} u_\infty}{L^2} \nabla^* p^*, \end{aligned}$$

we obtain Darcy's Law in the form

$$\mathbf{q}^* = -\frac{\text{Re}}{L^2} \mathbf{K} \nabla^* p^* \text{ in } \Omega. \quad (2.7)$$

Sometimes the introduction of a dimensionless permeability  $\mathbf{K}^* = \mathbf{K}/L^2$ , also called the Darcy number, is preferred in the above equation. However, we compute  $\mathbf{K}$  directly, since in most cases experimental and numerical characteristic length scales  $L$  for the input of the geometry coincide. If for example, one entry  $K_{\text{exp}}$  of the permeability tensor is experimentally computed in a representative cell of length  $L_{\text{exp}}$  and the numerical permeability  $K$  is computed in a cell scaled to  $L$ , we compare  $K_{\text{exp}}$  to the transformed numerical permeability

entry  $(K/L^2)L_{\text{exp}}^2$  according to equation (2.7). If both length scales coincide, no transformations are necessary. One usual unit for permeability is the darcy, (1 darcy  $\approx 10^{-12}\text{m}^2$ ), but we prefer to give it in  $\text{mm}^2$ .

### 2.2.2. Computation of Permeability via Darcy's Law

A direct computation of the permeability is offered by the so-called Unit Cell Problem, of which we see in homogenisation theory that it is equivalent to the solution of Darcy's Law for  $\mathbf{K}$ . The more indirect approach is to compute the Stokes equations with periodic boundary conditions up to a fixed pressure gradient in a textile repeat cell, and to use the velocity  $\mathbf{u}$  and the pressure  $p$  as input for Darcy's Law for the computation of  $\mathbf{K}$ . Thus, the velocity field  $\mathbf{u}$  is linked to the seepage velocity  $\mathbf{q}$  in Darcy's Law by integration over an arbitrary 2d-cut  $A$  of the computational domain

$$\mathbf{q} = \frac{1}{|A|} \int_A \mathbf{u} \, dx.$$

However, the permeability computation in such a way is not without problems. Consider that in three dimensions Darcy's Law reads

$$\begin{aligned} q_x &= -\frac{1}{\mu} \left( K_{xx} \frac{\partial p}{\partial x} + K_{xy} \frac{\partial p}{\partial y} + K_{xz} \frac{\partial p}{\partial z} \right) \\ q_y &= -\frac{1}{\mu} \left( K_{yx} \frac{\partial p}{\partial x} + K_{yy} \frac{\partial p}{\partial y} + K_{yz} \frac{\partial p}{\partial z} \right) \\ q_z &= -\frac{1}{\mu} \left( K_{zx} \frac{\partial p}{\partial x} + K_{zy} \frac{\partial p}{\partial y} + K_{zz} \frac{\partial p}{\partial z} \right), \end{aligned} \quad (2.8)$$

so that we have three equations for up to nine unknown entries of the permeability tensor, and  $\mathbf{K}$  cannot be computed directly. The solution of this problem is to conduct three (numerical) experiments. Physically, elements like  $K_{xy}$  give the flow that occurs in  $x$ -direction due to a pressure gradients in  $y$ -direction. Thus, in the first experiment, flow is driven by a given pressure difference in  $x$ -direction  $\partial p_1/\partial x$  and we measure the pressure differences that evolve in the other directions, namely  $\partial p_1/\partial y$  and  $\partial p_1/\partial z$ , where the subscript of the pressure now denotes the number of the experiment. In a second experiment, flow is driven by a pressure difference in  $y$ -direction  $\partial p_2/\partial y$ , and so on. This system of equations can then be solved for the permeability tensor  $\mathbf{K}$ . Doing so, we obtain for the entry  $K_{xx}$

$$-\mu K_{xx} = u \cdot \frac{-\frac{\partial p_1}{\partial z} \frac{\partial p_2}{\partial y} + \frac{\partial p_2}{\partial z} \frac{\partial p_1}{\partial y} - \frac{\partial p_3}{\partial y} \frac{\partial p_2}{\partial z} + \frac{\partial p_3}{\partial y} \frac{\partial p_1}{\partial z} - \frac{\partial p_3}{\partial z} \frac{\partial p_1}{\partial y} + \frac{\partial p_3}{\partial z} \frac{\partial p_2}{\partial y}}{-\frac{\partial p_3}{\partial x} \frac{\partial p_1}{\partial z} \frac{\partial p_2}{\partial y} + \frac{\partial p_3}{\partial x} \frac{\partial p_2}{\partial z} \frac{\partial p_1}{\partial y} - \frac{\partial p_3}{\partial y} \frac{\partial p_1}{\partial x} \frac{\partial p_2}{\partial z} + \frac{\partial p_3}{\partial y} \frac{\partial p_1}{\partial z} \frac{\partial p_2}{\partial x} - \frac{\partial p_3}{\partial z} \frac{\partial p_2}{\partial x} \frac{\partial p_1}{\partial y} + \frac{\partial p_3}{\partial z} \frac{\partial p_2}{\partial y} \frac{\partial p_1}{\partial x}}.$$

In this thesis we show numerically in Section 7.2, that the evolving pressure gradients  $\partial p_i/\partial x_j$  for  $i \neq j$  are neglectably small in the considered geometries. Hence, all terms that

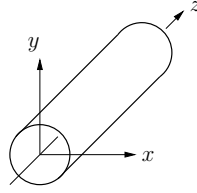


Fig. 2.3.: Unit cell of a porous medium consisting of cylinders:  $K_{xx} = K_{yy} = K_{\perp}$  and  $K_{zz} = K_{\parallel}$ .

are multiplied with other values than  $\partial p_1/\partial x$ ,  $\partial p_2/\partial y$ ,  $\partial p_3/\partial z$  vanish, and we obtain

$$-\mu K_{xx} = u \cdot \frac{\frac{\partial p_3}{\partial z} \frac{\partial p_2}{\partial y}}{\frac{\partial p_3}{\partial z} \frac{\partial p_2}{\partial y} \frac{\partial p_1}{\partial x}} = \frac{u}{\frac{\partial p_1}{\partial x}}.$$

The three main entries of the permeability tensor are the ones that are also measured in experiments, so we do not have to solve a linear system of equations to obtain the off-diagonal entries of the permeability tensor.

There are some porous media in which the permeability tensor takes a special form. Thus, we differentiate between anisotropic and isotropic porous media. A porous medium is called anisotropic if  $\mathbf{K}$  varies with the direction of measurement. If the porous medium is aligned with the principal directions of anisotropy, Darcy's Law has the form

$$q_x = -\frac{1}{\mu} K_{xx} \frac{\partial p}{\partial x}, \quad q_y = -\frac{1}{\mu} K_{yy} \frac{\partial p}{\partial y}, \quad q_z = -\frac{1}{\mu} K_{zz} \frac{\partial p}{\partial z}.$$

If, on the other hand,  $\mathbf{K}$  is independent of the direction of measurement at a point in the porous medium, this porous formation is isotropic. In this case the permeability can be expressed as a scalar and an identity matrix. In the even more special case that a medium is isotropic in two directions and is aligned with the principal directions of isotropy and anisotropy, we get a permeability tensor which reads

$$\mathbf{K} = \begin{bmatrix} K_{\perp} & 0 & 0 \\ 0 & K_{\perp} & 0 \\ 0 & 0 & K_{\parallel} \end{bmatrix}, \quad (2.9)$$

where  $K_{\parallel}$  denotes the permeability in the direction of the bedding plane and  $K_{\perp}$  the one perpendicular to it. This situation is illustrated in Figure 2.3 for a medium consisting of aligned cylinders. This example will gain importance later on, when the yarns of textiles are simplified as parallel bundles of cylinders.

More often than not none of the above special cases holds, and the permeability tensor has off-diagonal terms. For example, yarns in a textile are mostly not aligned with the principal coordinate directions. In such a case we either have to transform the permeability tensor as is explained in section (8.3.3) or we only compute the diagonal entries of the tensor as explained in the beginning of this section.

### 2.3. Brinkman's Equation

An alternative to Darcy's Law is what is commonly known as Brinkman's equation (or Brinkman's extension to Darcy's Law). In this thesis we will encounter Brinkman's equation in three different formulations. In all cases the permeability should be understood as a second-order, diagonal and positive definite tensor. Hence, a statement such as  $\mathbf{K} \rightarrow +\infty$  means that every entry of the tensor  $K_{xx} \rightarrow \infty$ ,  $K_{yy} \rightarrow \infty$  and  $K_{zz} \rightarrow \infty$ . Also,  $\mathbf{K}^{-1}\mathbf{u}$  for  $\mathbf{u} = (u, v, w)$  should be thought of as  $(u/K_{xx}, v/K_{yy}, w/K_{zz})^T$ .

1. We discuss Brinkman's equation in its original formulation as derived by Brinkman himself

$$\nabla p = -\mu\mathbf{K}^{-1}\mathbf{u} + \tilde{\mu}\Delta\mathbf{u} \quad \text{in } \Omega. \quad (2.10)$$

Here,  $\tilde{\mu}$  denotes an effective viscosity. Note, that the second term of the Brinkman equation is analogous to the diffusive term that appears in the Navier-Stokes equations.

2. We encounter the Brinkman equations in homogenisation theory

$$\begin{aligned} \nabla p - \mu\Delta\mathbf{u} + \frac{\mu}{\sigma^2}\mathbf{M}\mathbf{u} &= f & \text{in } \Omega \\ \nabla \cdot \mathbf{u} &= 0 & \text{in } \Omega \\ \mathbf{u} &= 0 & \text{on } \partial\Omega, \end{aligned} \quad (2.11)$$

where  $\sigma$  denotes some ratio of obstacle sizes and  $\mathbf{M}$  denotes a permeability which is computed by a very different Unit Cell Problem than  $\mathbf{K}$  in Darcy's Law.

3. We use the Stokes/Brinkman equations

$$\begin{aligned} \nabla p + \mu\mathbf{K}^{-1}\mathbf{u} &= \tilde{\mu}\Delta\mathbf{u} & \text{in } \Omega \\ \nabla \cdot \mathbf{u} &= 0 & \text{in } \Omega, \end{aligned} \quad (2.12)$$

or the Navier/Stokes Brinkman equations

$$\begin{aligned} \nabla p + (\mathbf{u} \cdot \nabla)\mathbf{u} + \mu\mathbf{K}^{-1}\mathbf{u} &= \tilde{\mu}\Delta\mathbf{u} & \text{in } \Omega \\ \nabla \cdot \mathbf{u} &= 0 & \text{in } \Omega, \end{aligned} \quad (2.13)$$

where we exploit the Brinkman equation's property that it reduces to a form of the (Navier-)Stokes equations for  $\mathbf{K} \rightarrow \infty$  and to the Darcy equations for  $\mathbf{K} \rightarrow 0$ .

Following Nield [50, pp. 12-14] we give a short overview on the scientific background of Brinkman's equation. First, Brinkman himself obtained a relationship between the permeability  $\mathbf{K}$  and the porosity  $\varphi$  as a "self-consistent" procedure, which is valid only when the porosity is sufficiently large ( $\varphi > 0.6$ ). This requirement is highly restrictive for natural porous media, as these have mostly porosities less than 0.6. There has been little experimental validation of Brinkman's theory, so from this point of view, its range of applicability

is quite unclear.

On the other hand Tam [56] points out that whenever the spatial length scale is much greater than  $\tilde{\mu}\|\mathbf{K}\|_{\max}/\mu$ , the diffusive term  $\Delta\mathbf{u}$  in equation (2.10) is negligible and Brinkman's equation reduces to Darcy's Law. Hence, for most practical purposes it is not necessary to include the Laplacian, and it is recommended to use Darcy's Law instead. For example, in textile applications we choose  $\tilde{\mu}/\mu = 1$  and the porosities of the yarns  $\mathbf{K}$  varies between  $10^{-4}\text{mm} \leq \|\mathbf{K}\|_{\max} \leq 10^{-7}\text{mm}$ , so  $\tilde{\mu}\|\mathbf{K}\|_{\max}/\mu \leq 10^{-8}\text{mm}$  is very small as opposed to the spatial length scale of the order of 1mm.

Following Allaire [8] we see in homogenisation theory that the Brinkman model holds only for porous particle sizes that are much smaller than the distance of neighbouring particles, which limits its applicability to porosities  $\varphi \approx 1$ . This is confirmed by the findings of Durlofsky and Brady [24] who use a Green's function approach to conclude that the Brinkman equation is valid for  $\varphi > 0.95$  only. In addition, the Brinkman equation is experimentally validated in rigid foams of a very high porosity of 0.972.

Thus, for practical purposes we use Brinkman's equation only in its form of the Stokes/Brinkman equations (2.12 or 2.13) in order to match flow solutions in a porous medium and a pure fluid part. This approach is mathematically validated in Chapter 4.

The question remains how to match  $\tilde{\mu}$  and  $\mu$ . Brinkman set them equal to each other, but this is not generally true. Rather,  $\tilde{\mu}/\mu$  depends on the geometry of the porous medium [50]. However, to the knowledge of this author, the question of how they should be matched is not quite solved yet, and we refer the reader to [34, p. 27] and [50, p. 13] for a more detailed discussion. For our purposes we set  $\tilde{\mu} = \mu$  and the agreement of the numerical solution of the Stokes/Brinkman equations and the Stokes equations supports this choice.



### 3. Homogenisation of the Stokes and Navier-Stokes Equations

Motivated by empirical filtration laws like Darcy and Brinkman, research has been devoted to the theoretical fortification of these macroscopic laws. In principal, there are two different approaches that might be considered, namely volume averaging and homogenisation. The main difference between them is that the upscaled equation in the first method is derived by smoothing and spatially averaging formulas and in the second by letting the microscale tend to zero.

In the volume averaging approach the equations that hold on the pore scale are integrated over sufficiently large representative volumes. Then the so-called averaging theorems aim at the elimination of all unknowns from the microscale and at replacing them by averaged variables. These variables are assumed to be independent of the pore scale and should reflect the PDEs' behaviour on the macroscale (cf. [34] and the references therein). This method is widely used in civil engineering.

On the other hand homogenisation, a theory developed in mathematics, considers a whole bunch of functions  $u_\varepsilon$ , where  $\varepsilon$  is a scale parameter denoting the typical size of the pore. The function  $u_\varepsilon$  represents the solution of the PDE at the microscale and homogenisation theory studies the limit  $\lim_{\varepsilon \rightarrow 0} u_\varepsilon$ . The basic idea behind this limit process is that the complicated microstructure averages out and that the PDE obtained at the limit represents a filtration law.

This chapter is devoted to the homogenisation of the Stokes and Navier-Stokes equations in a periodic porous domain. We will see that both Darcy's and Brinkman's Law can be obtained as the filtration law in the limit process  $\varepsilon \rightarrow 0$  depending on how we let the obstacles size  $a_\varepsilon$  scale with the period. The focus in this chapter is mainly on the Stokes equations which are not only sufficient to describe slow, viscous flow in textiles, but also offer a unique and easily extendable insight how the method of homogenisation works. This insight is particularly useful as the permeability tensor is computed by the so-called Unit Cell Problems, whose background becomes apparent in the more detailed parts of homogenisation theory.

In literature there are two methods devoted to homogenisation in periodic structures: two-scale asymptotic expansion (cf. [45] and [53]) and two-scale convergence (cf. [10, 11, 31]). Two-scale convergence is the more unified approach integrating the derivation of macroscopic laws and the convergence to their solutions. On the other hand, two-scale asymptotic expansion is the more general and explicit method, which is why we use a combination of both.

In a second part of this chapter we carry out a brief survey of homogenisation results for the Navier-Stokes equations. The nonlinear term in the Navier-Stokes equations can in some cases be seen as a small perturbation of the Stokes equations leading to very similar

proofs. But as soon as we allow the viscosity to take very small values or to vary with  $\varepsilon$ , theoretical results are more difficult to obtain or have not yet been obtained at all.

### 3.1. Definition of a Porous Medium

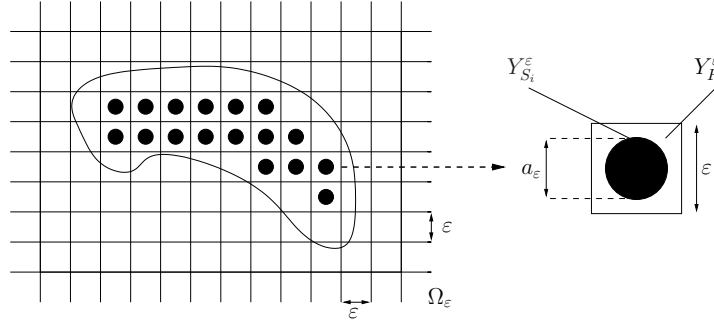


Fig. 3.1.: A periodic porous medium.

In order to derive the porous media flow equations, we first need a mathematical description of a porous medium. Let  $\Omega \subset \mathbb{R}^n$ ,  $n = 2, 3$ , be a smooth, bounded, connected domain representing a periodic structure. Suppose the set  $\Omega$  to be covered by a regular mesh of size  $\varepsilon$ . In this mesh, each cell shall be denoted by  $Y_i^\varepsilon = ]0, \varepsilon[^n$  with  $1 \leq i \leq N(\varepsilon)$ , where  $N(\varepsilon) = |\Omega| \varepsilon^{-n} (1 + o(1))$  denotes the number of cells. At the centre of each of the cells that are entirely included in  $\Omega$ , obstacles  $Y_{S_i}^\varepsilon$  with size  $a_\varepsilon$  represent the solid part of the medium. Then the fluid domain  $\Omega_\varepsilon \subset \Omega$  is obtained from  $\Omega$  by removing these periodically distributed obstacles

$$\Omega_\varepsilon = \Omega - \bigcup_{i=1}^{N(\varepsilon)} Y_{S_i}^\varepsilon. \quad (3.1)$$

Next, we define the associated unit cell or periodic cell  $Y = ]0, 1[^n$ ,  $n = 2, 3$  of the porous medium.  $Y$  is obtained by a linear homeomorphism  $\Pi_i^\varepsilon$  of each cell  $Y_i^\varepsilon$  with ratio of magnification  $1/\varepsilon$  (i.e. we rescale the cells  $Y_i^\varepsilon$  to one). Hence,

$$Y_S = \Pi_i^\varepsilon(Y_{S_i}^\varepsilon) \text{ and } Y_F = \Pi_i^\varepsilon(Y_{F_i}^\varepsilon) \quad (3.2)$$

denote the solid and the fluid part of the unit cell. Further, we assume that the fluid part  $Y_F$  repeated by  $Y$ -periodicity is a smooth, connected, open set of  $\mathbb{R}^n$  and that  $Y_S$  is a smooth closed set. For the boundary of the unit cell  $\partial Y_F$  we differentiate between the boundary  $\Gamma_1$  of the obstacles and the boundary  $\Gamma_2$  of the cell itself, where  $\partial Y_F = \Gamma_1 \cup \Gamma_2$  (Fig. 3.2).

An example of a two-dimensional idealised periodicity cell fulfilling the above assumptions is given in Figure (3.2). These quite restrictive conditions imply that the solid part of each period is strictly contained in the period and that the union of solid parts does not

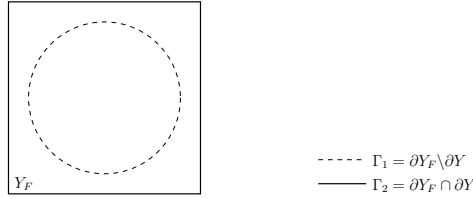


Fig. 3.2.: Unit cell of a porous medium with definition of the boundaries.

form a connected body. This is not fulfilled by the typical three-dimensional porous media cell, where the parts  $Y_S$  are typically connected. An extension to the case that both solid and fluid part ‘are of one piece’ can, however, be found in [53] and [5], which we also discuss at the end of this chapter for textile geometries.

## 3.2. Homogenisation of the Stokes Equations

In this section we specify the flow problem in the geometrical structure defined above. We suppose that fluid flow on the microscale is stationary and viscous and can be modelled by the Stokes equations, which we refer to by  $\mathcal{P}^\varepsilon$

$$\mathcal{P}^\varepsilon \left\{ \begin{array}{ll} \nabla p_\varepsilon - \mu \Delta \mathbf{u}_\varepsilon = \mathbf{f} & \text{in } \Omega_\varepsilon \\ \nabla \cdot \mathbf{u}_\varepsilon = 0 & \text{in } \Omega_\varepsilon \\ \mathbf{u}_\varepsilon = 0 & \text{on } \partial\Omega_\varepsilon \setminus \Omega \\ \text{boundary condition} & \text{on } \partial\Omega_\varepsilon \cap \Omega. \end{array} \right. \quad (3.3)$$

Here,  $\mu$  denotes the viscosity,  $\mathbf{f}$  represents volume forces,  $\mathbf{u}_\varepsilon$  denotes the velocity and  $p$  the pressure. In the space

$$W_\varepsilon = \{z \in H^1(\Omega_\varepsilon), z = 0 \text{ on } \partial\Omega_\varepsilon \setminus \partial\Omega, \text{ b.c. on } \partial\Omega_\varepsilon \cap \Omega\}$$

the variational problem associated to (3.3) is to find  $\mathbf{u}_\varepsilon \in W_\varepsilon$ ,  $\nabla \cdot \mathbf{u}_\varepsilon = 0$  in  $\Omega_\varepsilon$  and  $p_\varepsilon \in L^2(\Omega_\varepsilon)$  such that

$$\mu \int_{\Omega_\varepsilon} \nabla \mathbf{u}_\varepsilon \nabla \varphi \, dx - \int_{\Omega_\varepsilon} p_\varepsilon \operatorname{div} \varphi \, dx = \int_{\Omega_\varepsilon} \mathbf{f} \varphi \, dx \quad \forall \varphi \in W_\varepsilon. \quad (3.4)$$

If the forcing term is assumed to have the usual regularity  $\mathbf{f} \in L^2(\Omega_\varepsilon)^n$ , then elliptic variational theory gives the existence of a unique velocity field which solves (3.4) [45]. Uniqueness of the pressure field can be shown up to an additive constant, which is usually fixed by supposing  $\int_{\Omega_\varepsilon} p_\varepsilon \, dx = 0$ . Fixing this constant is equivalent to showing uniqueness in the corresponding equivalence class

$$L^2(\Omega_\varepsilon)/\mathbb{R} = \{p_\varepsilon \in L^2(\Omega_\varepsilon) : \int_{\Omega_\varepsilon} p_\varepsilon \, dx = 0\}.$$

Note, that equations (3.3) do not consist of a single problem, but of a whole series of problems  $\mathcal{P}^\varepsilon$  when we let  $\varepsilon$  pass to zero. That is, the sequence of solutions  $(\mathbf{u}_\varepsilon, p_\varepsilon)$  is not defined in a fixed domain independent of  $\varepsilon$  but in varying sets  $\Omega_\varepsilon$ . However, for homogenisation purposes convergence proofs in fixed Sobolev spaces on  $\Omega$  are required, which is why the first step in the upscaling of (3.3) must be to extend  $(\mathbf{u}_\varepsilon, p_\varepsilon)$  on the whole domain  $\Omega$ . The velocity can be extended to zero in  $\Omega \setminus \Omega_\varepsilon$ . This extension is not only compatible with the velocity's no-slip boundary condition on  $\partial\Omega_\varepsilon \setminus \Omega$  but conveniently, also  $L^q$  and  $H_0^{1,q}$  norms are preserved for  $1 < q < \infty$ . Thus we define the extension,

$$\tilde{\mathbf{u}}_\varepsilon = \begin{cases} \mathbf{u}_\varepsilon & \text{in } \Omega_\varepsilon \\ 0 & \text{in } \Omega \setminus \Omega_\varepsilon \end{cases}. \quad (3.5)$$

The pressure is extended to the whole domain  $\Omega$  by

$$\tilde{p}_\varepsilon = \begin{cases} p_\varepsilon & \text{in } \Omega_\varepsilon \\ \frac{1}{|Y_{F_i}^\varepsilon|} \int_{Y_{F_i}^\varepsilon} p_\varepsilon d\mathbf{y} & \text{in } Y_{S_i}^\varepsilon \text{ for } 1 \leq i \leq N(\varepsilon). \end{cases} \quad (3.6)$$

In the following, if not otherwise indicated, we will always use the extended versions of pressure and velocity and we will omit the tilde symbol. The next step in the homogenisation process is to find a priori estimates for the velocity and the pressure, which are given by

### Lemma 3.1

*The extensions  $(\mathbf{u}_\varepsilon, p_\varepsilon)$  of the solution of the Stokes problem (3.3) satisfy the a priori estimates*

$$\frac{1}{\varepsilon^2} \|\mathbf{u}_\varepsilon\|_{L^2(\Omega)^n} + \frac{1}{\varepsilon} \|\nabla \mathbf{u}_\varepsilon\|_{L^2(\Omega)^{n \times n}} \leq C \quad (3.7)$$

$$\|p_\varepsilon\|_{L^2(\Omega)/\mathbb{R}} \leq C, \quad (3.8)$$

where the constant  $C$  does not depend on  $\varepsilon$ .

The Lemma's proof can be found in [45] and we are now very well equipped to study the homogenisation limit  $\varepsilon \rightarrow 0$  of the Stokes equations  $\mathcal{P}^\varepsilon$ . In the next section we present the main theorem, whose proof we give in three steps. Firstly, we derive Darcy's Law by an asymptotic expansion of the Stokes equations. Secondly, existence and uniqueness of the limit equations are shown. Thirdly, the convergence  $(\mathbf{u}_\varepsilon, p_\varepsilon)$  towards Darcy's Law is addressed with the two-scale convergence method.

We have not yet given explicit conditions on the outer boundary  $\partial\Omega_\varepsilon \cap \Omega$  of the Stokes equations, because there is a choice. Mikelić [45] handles the problem with periodic boundary conditions in a rectangular domain  $\Omega = [0, L]^n$ , i.e. he specifies in (3.3)

$$\{\mathbf{u}_\varepsilon, p_\varepsilon\} \text{ is } \Omega - \text{periodic}. \quad (3.9)$$

Many other authors (cf. Allaire [31] or Sanchez-Palencia [53]) set no-slip conditions on the

outer boundary

$$\mathbf{u}_\varepsilon = 0 \text{ on } \partial\Omega_\varepsilon \cap \Omega. \quad (3.10)$$

The derivation of Darcy's Law and the convergence proof are basically the same for both cases, differentiating only in some periodicity assumptions on the homogenised equations. Hence, for the case of periodic boundary conditions we refer the reader to [45] and [52] and continue with Dirichlet zero boundary conditions. Apart from the outer boundary, the condition on the obstacles  $\partial\Omega_\varepsilon \setminus \Omega$  is always the same no-slip condition, except for Section 3.4, in which we shortly present the slip case.

### 3.2.1. Main Theorem: Darcy's Law

**Theorem 3.2** [DARCY'S LAW]

Let  $(\mathbf{u}_\varepsilon, p_\varepsilon)$  denote the extension of the solution of the Stokes problem (3.3). Then  $\mathbf{u}_\varepsilon$  converges weakly in  $L^2(\Omega)^n$  to  $\mathbf{u}$ , and  $p_\varepsilon$  converges strongly in  $L^2(\Omega) \setminus \mathbb{R}$  to  $p$ , where  $(\mathbf{u}, p)$  is the solution of the respective homogenised problem, which is a Darcy's Law

$$\mathcal{P}^0 = \begin{cases} \mathbf{u} = \frac{1}{\mu} \mathbf{K}(\mathbf{f} - \nabla p) & \text{in } \Omega \\ \nabla \cdot \mathbf{u} = 0 & \text{in } \Omega \\ \mathbf{u} \cdot \boldsymbol{\nu} = 0 & \text{on } \partial\Omega. \end{cases} \quad (3.11)$$

The permeability tensor  $\mathbf{K}$  is defined by

$$K_{ij} = \int_{Y_F} \nabla_y \mathbf{w}^i \nabla_y \mathbf{w}^j \, d\mathbf{y} \text{ for } 1 \leq i, j \leq n, \quad (3.12)$$

where  $\mathbf{w}^i$  for  $1 \leq i \leq n$  denote the solutions of the Unit Cell Problems.

**Definition 3.3** [UNIT CELL PROBLEMS]

For  $1 \leq i, j \leq n$  find  $(\mathbf{w}^i, \pi^i) \in H_{\text{per}}^1(Y)^n \times L^2(Y)$  such that

$$\begin{aligned} -\Delta \mathbf{w}^i + \nabla \pi^i &= \mathbf{e}^i & \text{in } Y_F \\ \nabla \cdot \mathbf{w}^i &= 0 & \text{in } Y_F \\ \mathbf{w}^i &= 0 & \text{on } \partial Y_F \setminus \partial Y \\ \mathbf{w}^i, \pi^i & & Y - \text{periodic.} \end{aligned} \quad (3.13)$$

where  $\mathbf{e}^i$  denotes the vector with components  $e_j^i = \delta_{ij}$ , and  $H_{\text{per}}^1(Y)^n$  is the Sobolev space  $H^{1,2}(Y)^n$  restricted to  $Y$ -periodic functions.

### 3.2.2. Two-Scale Asymptotic Expansion

In order to overcome the disparity of the two length scales, the microscale  $\varepsilon$  of the pores and the macroscopic scale  $L$  of the reservoir, an asymptotic expansion of the functions  $(\mathbf{u}_\varepsilon, p_\varepsilon)$  is postulated, in which each function in the series depends on variables of both length scales. A priori there is no reason for this ansatz to hold true. Thus, in a second

step, the homogenised result has to be justified by proving the convergence of  $(\mathbf{u}_\varepsilon, p_\varepsilon)$  to the solution  $(\mathbf{u}, p)$  of the homogenised problem  $\mathcal{P}^0$ . Tartar [57] was the first to give a proof for this convergence result in the appendix of [53], employing what has later been called the energy method.

This section will focus on the first part of the two-scale asymptotic expansion method: the heuristic derivation of the Darcy equations and will be mainly based on the works of Mikelić [45] and [53].

Let us begin with the assumption that the pressure  $p_\varepsilon$  and the velocity  $\mathbf{u}_\varepsilon$  can be expanded such that

$$\begin{aligned}\mathbf{u}^\varepsilon(x) &= \varepsilon^2 \mathbf{u}^0(x, y) + \varepsilon^3 \mathbf{u}^1(x, y) + \dots \\ p^\varepsilon(x) &= p^0(x, y) + \varepsilon p^1(x, y) + \dots,\end{aligned}\tag{3.14}$$

where  $y = \frac{x}{\varepsilon}$  represents the fast scale of the porous medium, on which  $p_\varepsilon$  and  $\mathbf{u}_\varepsilon$  are supposed to depend periodically. Further, we would like to insert this expansion into the Stokes equations (3.3) on  $\Omega_\varepsilon$ . Hence, we have to transform the appropriate differential operators, too, denoting by the subscript the variable involved in the differentiation

$$\begin{aligned}\nabla &= \nabla_x + \frac{1}{\varepsilon} \nabla_y \\ \operatorname{div} &= \operatorname{div}_x + \frac{1}{\varepsilon} \operatorname{div}_y \\ \Delta &= \Delta_x + \frac{2}{\varepsilon} \operatorname{div}_x \nabla_y + \frac{1}{\varepsilon^2} \Delta_y.\end{aligned}\tag{3.15}$$

Insertion of equations (3.14) and (3.15) into the Stokes equations (3.3), yields the following equations, which we arrange according to the order of approximation.

$$\begin{aligned}O(\varepsilon^{-1}) : & \quad \nabla_y p^0(x, y) = 0 & \quad \text{in } \Omega \times Y_F \\ O(1) : & \quad -\mu \Delta_y \mathbf{u}^0(x, y) + \nabla_y p^1(x, y) + \nabla_x p^0(x, y) = f(x) & \quad \text{in } \Omega \times Y_F \\ O(\varepsilon) : & \quad \operatorname{div}_y \mathbf{u}^0(x, y) = 0 & \quad \text{in } \Omega \times Y_F \\ & \quad -\mu \Delta_y \mathbf{u}^1(x, y) + \nabla_y p^2(x, y) + \nabla_x p^1(x, y) = 0 & \quad \text{in } \Omega \times Y_F \\ O(\varepsilon^2) : & \quad \operatorname{div}_x \mathbf{u}^0(x, y) + \operatorname{div}_y \mathbf{u}^1(x, y) = 0 & \quad \text{in } \Omega \times Y_F \\ & \quad -\mu \Delta_y \mathbf{u}^2(x, y) + \nabla_y p^3(x, y) + \nabla_x p^2(x, y) = 0 & \quad \text{in } \Omega \times Y_F \\ & \quad \mathbf{u}^0(x, y) = 0 & \quad \text{on } \Omega \times \partial Y_F \\ & \quad \{\mathbf{u}^0(x, y), p^1(x, y)\} & \quad \text{is periodic in } y \\ O(\varepsilon^3) : & \quad \dots\end{aligned}$$

First, we note that the  $\varepsilon^{-1}$ -term yields the single equation  $\nabla_y p^0(x, y) = 0$ . This equation implies that  $p = p^0(x)$  is independent of the fast scale  $y$ . Next, if we consider the two

divergences in the  $\varepsilon^2$ -term, integration over  $Y_F$  yields

$$\begin{aligned}
0 &= \int_{Y_F} \operatorname{div}_x \mathbf{u}^0(x, y) + \operatorname{div}_y \mathbf{u}^1(x, y) dy \\
&= \operatorname{div}_x \int_{Y_F} \mathbf{u}^0(x, y) dy + \int_{Y_F} \operatorname{div}_y \mathbf{u}^1(x, y) dy \\
&= \operatorname{div}_x \int_{Y_F} \mathbf{u}^0(x, y) dy + \int_{\partial Y_F} \boldsymbol{\nu} \cdot \mathbf{u}^1(x, y) d\Gamma \\
&= \operatorname{div}_x \int_{Y_F} \mathbf{u}^0(x, y) dy.
\end{aligned}$$

Summarising the conditions that  $\{\mathbf{u}^0, p^0, p^1\}$  should satisfy in  $\Omega \times Y_F$ , we obtain the following problem called *Stokes-system with two pressures*

$$\begin{aligned}
-\mu \Delta_y \mathbf{u}^0(x, y) + \nabla_y p^1(x, y) + \nabla_x p^0(x) &= \mathbf{f}(x) && \text{in } \Omega \times Y_F \\
\operatorname{div}_y \mathbf{u}^0(x, y) &= 0 && \text{in } \Omega \times Y_F \\
\mathbf{u}^0(x, y) &= 0 && \text{on } \Omega \times \partial Y_F \\
\{\mathbf{u}^0(x, y), p^1(x, y)\} &&& \text{is periodic in } y \\
\operatorname{div}_x \int_{Y_F} \mathbf{u}^0(x, y) dy &= 0 && \text{in } \Omega.
\end{aligned} \tag{3.16}$$

And we introduce the seepage velocity and porosity by the following definition.

**Definition 3.4** [SEEPAGE VELOCITY, POROSITY]

By seepage velocity we denote the quantity

$$\mathbf{q}^0(x) \equiv \frac{1}{|Y_F|} \int_{Y_F} \mathbf{u}^0(x, y) dy$$

for the filtration through the porous medium  $\Omega$  with porosity  $|Y_F|$ .

### 3.2.3. Local Solvability of the Stokes System with Two Pressures

Following Sanchez [53], we study the local part of equation (3.16), where the fast scale independent pressure  $p^0$  as well as  $\mathbf{f}$  play the role of a given force and where  $x$  is a parameter. The unknowns then are  $\mathbf{u}^0$  and  $p^1$ . First, we define an appropriate space of  $Y$ -periodic functions

$$\mathcal{V}_Y = \{\mathbf{u}(\cdot, y) \in H^1(Y_F)^n : \operatorname{div}_y \mathbf{u}(\cdot, y) = 0 \text{ and } \mathbf{u} \text{ is } Y\text{-periodic}\}, \tag{3.17}$$

which is a Hilbert space in which the associated norm is

$$(\mathbf{u}, \mathbf{v})_{\mathcal{V}_Y} = \int_{Y_F} \nabla \mathbf{u} \cdot \nabla \mathbf{v} dy. \tag{3.18}$$

For the investigation of the local Stokes system with two pressures we need the following classical results which are applicable for a general set of Stokes equations in a bounded domain  $\Omega$  with a smooth boundary.

**Lemma 3.5**

If  $\mathbf{f} \in L^2(\Omega)$  the Stokes equations have a unique solution  $\mathbf{v} \in H^2(\Omega)^n$  and  $p \in H^1(\Omega) \setminus \mathbb{R}$ .

**Lemma 3.6**

Let  $\Omega$  be a Lipschitz bounded open set of  $\mathbb{R}^n$  and  $\mathcal{T} = \{\mathbf{v} \in H_0^1(\Omega)^n \text{ such that } \nabla \cdot \mathbf{v} = 0\}$ . Moreover, we denote by  $\langle \cdot, \cdot \rangle$  the duality product between  $H^{-1}$  and  $H_0^1$  and let  $\mathbf{g} \in H^{-1}(\Omega)^n$ . A necessary and sufficient condition that

$$\mathbf{g} = \nabla \phi$$

for some  $\phi \in L^2(\Omega)$ , is that

$$\langle \mathbf{g}, \Psi \rangle = 0 \quad \forall \Psi \in \mathcal{T}.$$

A proof of this Lemma can be found in the classical textbook by Temam [58]. Thus equipped we prove the following theorem:

**Theorem 3.7** [LOCAL SOLVABILITY OF THE STOKES SYSTEM WITH TWO PRESSURES]

Finding a solution  $(\mathbf{u}^0, p^1)$  fulfilling the local Stokes system with two pressures (3.16) is equivalent to finding  $\mathbf{u}^0 \in \mathcal{V}_Y$  satisfying

$$(\mathbf{u}, \Psi)_{\mathcal{V}_Y} = \left( f_i - \frac{\partial p^0}{\partial x_i} \right) \int_{Y_F} \Psi_i dy \quad \forall \Psi \in \mathcal{V}_Y. \quad (3.19)$$

Furthermore, in both cases we obtain  $(\mathbf{u}^0, p^1) \in H^2(Y_F)^n \times H^1(Y_F)$ .

*Proof.*

“  $\implies$  ”

Suppose  $(\mathbf{u}^0, p^1)$  is a solution of the local two pressure Stokes system. Then, we have to show that  $\mathbf{u}^0 \in \mathcal{V}_Y$  and satisfies equation (3.19). In a first step we multiply the two-pressure Stokes system (3.16) with a test function  $\Psi \in \mathcal{V}_Y$  and evaluate this multiplication term by term. For the pressure  $\nabla_y p^1(\cdot, y)$  we obtain

$$\begin{aligned} \int_{Y_F} \nabla_y p^1 \Psi_i dy &= \int_{Y_F} \frac{\partial p^1}{\partial y_i} \Psi_i dy \\ &= \int_{Y_F} \frac{\partial}{\partial y_i} (p^1 \Psi_i) dy + \int_{Y_F} p^1 \frac{\partial \Psi_i}{\partial y_i} dy \\ &= \int_{\partial Y_F} p^1 \Psi_i \nu^i dS + 0 \\ &= 0. \end{aligned} \quad (3.20)$$

The integral over  $\partial Y_F$  vanishes, because the integrals over both parts of the boundaries  $\Gamma_1$  and  $\Gamma_2$  vanish. On  $\Gamma_1$  it holds that  $\Psi|_{\Gamma_1} = 0$  because of the no-slip condition on the obstacles. On  $\Gamma_2$   $p^1$  and  $\Psi$  are periodic but the unit outward normal  $\nu$  changes the sign

on points  $y$  and  $\hat{y}$  homologous by periodicity (Fig. 3.3). Hence we obtain for the integral over  $\Gamma_2$

$$\begin{aligned} \int_{\Gamma_2} p^1 \Psi_i \nu^i dS &= \int_{\Gamma_{2/2}} p^1(y) \Psi_i(y) \nu^i dS + \int_{\hat{\Gamma}_{2/2}} p^1(\hat{y}) \Psi_i(\hat{y}) \hat{\nu}^i dS \\ &= \int_{\Gamma_{2/2}} p^1(y) \Psi_i(y) \nu^i dS - \int_{\Gamma_{2/2}} p^1(y) \Psi_i(y) \nu^i dS \\ &= 0. \end{aligned}$$

This confirms that  $p^1(\cdot, y) \in H^1(Y_F)$ . Next, we test the Laplacian in the two-pressure Stokes system in the same manner with the function  $\Psi$

$$\begin{aligned} \int_{Y_F} \Delta_y \mathbf{u}^0 \Psi dy &= \int_{Y_F} \Delta_y u_i^0 \Psi_i dy \\ &= \int_{Y_F} \frac{\partial^2 u_i}{\partial y_k^2} \Psi_i dy \\ &= \int_{Y_F} \left( \frac{\partial}{\partial y_k} \left( \frac{\partial u_i}{\partial y_k} \Psi_i \right) - \frac{\partial u_i}{\partial y_k} \frac{\partial \Psi_i}{\partial y_k} \right) dy \quad (3.21) \\ &= \int_{\partial Y_F} \nu_k \frac{\partial u_i}{\partial y_k} \Psi_i dS - \int_{Y_F} \frac{\partial u_i}{\partial y_k} \frac{\partial \Psi_i}{\partial y_k} dy \\ &= - \int_{Y_F} \frac{\partial u_i}{\partial y_k} \frac{\partial \Psi_i}{\partial y_k} dy = \int_{Y_F} \nabla_y \mathbf{u}^0 \nabla_y \Psi dy. \end{aligned}$$

This confirms  $\mathbf{u}(\cdot, y) \in \mathcal{V}_Y$  and also  $\mathbf{u}(\cdot, y) \in H^2(Y_F)^n$ . Further, inserting this information into (3.16), employing the scalar product defined on  $\mathcal{V}_Y$  and using information from equation (3.20), we obtain

$$\begin{aligned} (\mathbf{u}, \Psi)_{\mathcal{V}_Y} &= - \int_{Y_F} \Delta_y \mathbf{u}^0 \Psi dy \\ &= \left( f_i - \frac{\partial p^0}{\partial x_i} \right) \int_{Y_F} \Psi_i dy \quad \forall \Psi \in \mathcal{V}_Y. \end{aligned} \quad (3.22)$$

Hence,  $\mathbf{u} \in \mathcal{V}_Y$  satisfies (3.19).

“ $\Leftarrow$ ”

Suppose now that we already knew that  $\mathbf{u}^0 \in V_Y$  satisfied (3.19). By integration by parts we obtain

$$\int_{Y_F} \left[ \Delta_y u_i^0 + \left( f_i - \frac{\partial p^0}{\partial x_i} \right) \right] \Psi_i dy = 0 \quad \forall \Psi \in \mathcal{V}_Y. \quad (3.23)$$

The above equation is a linear and bounded functional, so that we can conclude

$$\left[ \Delta_y u_i^0 + \left( f_i - \frac{\partial p^0}{\partial x_i} \right) \right] \in H^{-1}(Y_F).$$

Furthermore, note that equation (3.23) also holds for any  $\Psi \in H_0^1(Y_F)^n$  with  $\operatorname{div} \Psi = 0$ .

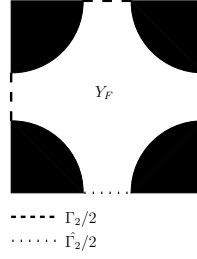


Fig. 3.3.: Single cell of a porous medium. Marked are the points of the boundaries which are homologous by periodicity.

Hence, Lemma 3.6 applies and gives the existence of some  $p^1 \in L^2(Y_F)$  such that

$$\nabla p^1 = \Delta_y u_i^0 + \left( f_i - \frac{\partial p^0}{\partial x_i} \right),$$

which is the first of the two-pressure Stokes equations (3.16). Moreover, by Lemma 3.5 we even get the regularity properties  $\mathbf{u}^0 \in H^2(Y_F)^n$  and  $p^1 \in H^1(Y_F)^n$ . In a last step we have to show that the so found function  $p^1$  is  $Y$ -periodic. We already know that it fulfils the first equation of (3.16) which we now multiply again by  $\Psi_i$ . By comparison with (3.23) we find

$$0 = - \int_{Y_F} \frac{\partial p^1}{\partial y_i} \Psi_i dy.$$

Partial integration and application of  $\operatorname{div} \Psi = 0$  yields

$$0 = \int_{Y_F} \frac{\partial}{\partial y_i} (p^1 \Psi_i) dy = \int_{\partial Y_F} p^1 \Psi_i \nu^i dS. \quad (3.24)$$

The surface integral in (3.24) is zero on the part of the boundary  $\Gamma_1$  because  $\Psi$  is zero there. For the part  $\Gamma_2$  we consider again only half the faces of the period and take into account points  $y$  and  $\hat{y}$  which are homologous by periodicity (Fig. 3.3). On these points  $\Psi_i(y) = \Psi_i(\hat{y})$ . Consequently (3.24) becomes

$$0 = \int_{\partial(Y_F \cap Y)/2} [p^1(y) - p^1(\hat{y})] \Psi_i \cdot n^i dS,$$

which holds for any  $\Psi_i \cdot n^i$ . Hence, we have to conclude  $p^1(y) = p^1(\hat{y})$  which is the required  $Y$ -periodicity.

Consequently, the solution of the local problem (3.16) is equivalent to the variational problem: find  $\mathbf{u}^0 \in \mathcal{V}_Y$  satisfying (3.19). In both cases the regularity properties  $(\mathbf{u}^0, p^1) \in H^2(Y_F)^n \times H^1(Y_F)$  hold.  $\square$

The existence and uniqueness of the solution of (3.19) is an immediate consequence of Lax Milgram's Theorem because the right-hand side is a linear and bounded functional on  $\mathcal{V}_Y$ .

### 3.2.4. Derivation of Darcy's Law

Let us consider the Unit Cell Problems (definition 3.3) as auxiliary problems for the derivation of Darcy's Law. They consist of  $n$  Stokes problems which naturally (cf. Theorem 3.7) admit a unique solution. With the help of the unit cell and the two pressure Stokes problem, Darcy's Law follows immediately. Multiplication of the first unit cell equation by a test function  $\Psi \in \mathcal{V}_Y$  yields for  $1 \leq i, j \leq n$

$$\begin{aligned}
& - \int_{Y_F} \frac{\partial^2 w_j^i}{\partial y_k^2} \Psi_j \, dy + \int_{Y_F} \frac{\partial \pi^i}{\partial y_j} \Psi_j \, dy = \int_{Y_F} \Psi \mathbf{e}^i \, dy \\
\Leftrightarrow & \int_{Y_F} (\mathbf{w}^i, \Psi) \, dy + \int_{Y_F} \pi^i \frac{\partial \Psi_j}{\partial y_j} \, dy = \int_{Y_F} \Psi_i \, dy \\
\Leftrightarrow & \int_{Y_F} (\mathbf{w}^i, \Psi) \, dy = \int_{Y_F} \Psi_i \, dy.
\end{aligned} \tag{3.25}$$

Comparison of this equation with the variational formulation (3.19) leads to

$$\begin{aligned}
(\mathbf{u}, \Psi)_{\mathcal{V}_Y} &= \left( f_i - \frac{\partial p^0}{\partial x_i} \right) \int_{Y_F} \Psi_i \, dy \quad \forall \Psi \\
\Leftrightarrow (\mathbf{u}, \Psi)_{\mathcal{V}_Y} &= \left( f_i - \frac{\partial p^0}{\partial x_i} \right) \int_{Y_F} (\mathbf{w}^i, \Psi) \, dy \quad \forall \Psi,
\end{aligned}$$

and hence

$$\mathbf{u} = \left( f_i - \frac{\partial p^0}{\partial x_i} \right) \mathbf{w}^i,$$

or

$$u_j = \left( f_i - \frac{\partial p^0}{\partial x_i} \right) w_j^i.$$

Applying the mean integral, the definition of the permeability tensor in Theorem 3.2 and definition 3.4 of the seepage velocity  $\mathbf{q}^0$ , we obtain

$$q_j^0 = \frac{1}{|Y_F|} \int_{Y_F} u_j \, dy = \frac{1}{|Y_F|} \int_{Y_F} w_j^i \, dy \left( f_i - \frac{\partial p^0}{\partial x_i} \right) = K_{ij} \left( f_i - \frac{\partial p^0}{\partial x_i} \right),$$

i.e. (considering Lemma 3.8) Darcy's Law.

**Remark:** For the second pressure  $p^1$  there exists an analogous formula, namely

$$p^1(x, y) = \sum_{j=1}^n \left[ \pi^j \left( f_j - \frac{\partial p^0}{\partial x_j} \right) \right]. \tag{3.26}$$

It can be obtained by multiplication of  $(\mathbf{f} - \nabla_x p^0(x))$  by the first equation of the Unit Cell Problem (3.3). Comparison with the two-pressure Stokes system (3.16) and application of the mean operator leads to the above equation as well as to the Darcy's Law for  $\mathbf{u}^0$ .

**Lemma 3.8**

The permeability tensor  $\mathbf{K}$  is symmetric and positive definite and the equation

$$K_{ij} = \int_{Y_F} \nabla_y \mathbf{w}^i \cdot \nabla_y \mathbf{w}^j dy = \int_{Y_F} w_j^i dy$$

holds for  $1 \leq i, j \leq n$ .

*Proof.* For  $1 \leq i, j \leq n$

$$\begin{aligned} K_{ij} &= \int_{Y_F} \nabla_y \mathbf{w}^i \cdot \nabla_y \mathbf{w}^j dy = - \int_{Y_F} \mathbf{w}^i \Delta_y \mathbf{w}^j dy && \text{Insert (3.13)} \\ &= - \int_{Y_F} \mathbf{w}^i (\nabla \pi_j - \mathbf{e}_j) dy = - \int_{Y_F} \mathbf{w}^i \nabla \pi_j dy + \int_{Y_F} \mathbf{w}^i \mathbf{e}_j dy && \text{Integration by parts} \\ &= \underbrace{\int_{Y_F} \nabla \cdot \mathbf{w}^i \pi_j dy}_{=0 \text{ (3.13)}} + \int_{Y_F} \mathbf{w}^i \mathbf{e}_j dy \\ &= \int_{Y_F} w_j^i dy. \end{aligned}$$

This formulation implies the symmetry of  $\mathbf{K}$ . In order to show that  $\mathbf{K}$  is positive definite, we first see that for all  $\mathbf{x} \in \mathbb{R}^n$

$$\begin{aligned} \mathbf{x}^T \mathbf{K} \mathbf{x} &= x_i K_{ij} x_j \\ &= \frac{1}{|Y_F|} \int_{Y_F} x_i w_j^i x_j dy = \frac{1}{|Y_F|} \int_{Y_F} x_i \nabla_y \mathbf{w}^i \nabla_y \mathbf{w}^j x_j dy \\ &= (x_i \mathbf{w}^i, x_j \mathbf{w}^j) = \|x_i \mathbf{w}^i\|_{V_2^2} \\ &\geq 0. \end{aligned}$$

Then it remains to be shown that  $x_i \mathbf{w}^i = 0 \Leftrightarrow x_i = 0$ . Hence, we take a test function  $\Psi$  such that  $\int_{Y_F} \Psi_i = x_i$ , which is possible because  $Y_F$  is connected. Also, we multiply equation (3.25) with the same  $x_i$

$$\int_{Y_F} (x_i \mathbf{w}^i, \Psi) dy = x_i \int_{Y_F} \Psi_i dy = x_i x_i,$$

and  $x_i \mathbf{w}^i = 0 \Rightarrow x_i = 0$ , whereas the opposite inclusion is obvious.  $\square$

### 3.2.5. Global Solvability of the Stokes Problem with Two Pressures

In this section we are going to show that problem (3.16) has a unique solution  $\{\mathbf{u}^0, p^0, p^1\}$  in some appropriate function space. We introduce the Hilbert space

$$\begin{aligned} \mathcal{V} = \{ \mathbf{u}(x, y) \in L^2(\Omega, \mathcal{V}_Y) : \operatorname{div}_x \int_{Y_F} \mathbf{u}(x, y) dy = 0 \text{ in } \Omega \\ \text{and } \boldsymbol{\nu} \cdot \int_{Y_F} \mathbf{u}(x, y) dy = 0 \text{ on } \partial\Omega \}. \end{aligned} \quad (3.27)$$

Further we need the space

$$\mathcal{Q} = \{ q \in L^2(Y_F) : q \text{ is } Y\text{-periodic} \}.$$

**Theorem 3.9** [SOLVABILITY OF THE STOKES SYSTEM WITH TWO PRESSURES]

*The Stokes system with two pressures (3.16) has a unique solution*

$$(\mathbf{u}^0, p^0, p^1) \in (\mathcal{V} \times H^1(\Omega)/\mathbb{R} \times L^2(\Omega, \mathcal{Q})).$$

*Proof.* Following [52] we first write the continuity equation in (3.16) in terms of the average velocity  $\mathbf{q}^0$ . We have

$$\operatorname{div}_x \mathbf{q}^0(x) = 0 \text{ in } \Omega. \quad (3.28)$$

Substitution of this property into Darcy's Law yields

$$\begin{aligned} 0 &= \operatorname{div}_x \left[ \frac{\mathbf{K}}{\mu} (\mathbf{f}(x) - \nabla_x p^0(x)) \right] \text{ in } \Omega \\ \Leftrightarrow \Delta_x p^0(x) &= \frac{\mathbf{K}}{\mu} \operatorname{div}_x \mathbf{f}(x) \text{ in } \Omega. \end{aligned} \quad (3.29)$$

In order to obtain the solution  $p^0$  of this elliptic equation we have to adjoin boundary conditions. For a discussion on this question see Section 5 in [53]. In our case the induced boundary condition on  $\partial\Omega$  for  $\mathbf{q}^0$  is of Neumann type

$$\boldsymbol{\nu}(x) \cdot \mathbf{q}^0(x) = 0 \text{ on } \partial\Omega. \quad (3.30)$$

For equation (3.29) this condition reads

$$\left[ \frac{\mathbf{K}}{\mu} (\mathbf{f}(x) - \nabla_x p^0(x)) \right] \cdot \boldsymbol{\nu}(x) = 0 \text{ on } \partial\Omega. \quad (3.31)$$

Thus, we have a second-order elliptic equation, which adjoined with Neumann boundary conditions, admits a unique solution  $p^0 \in H^1(\Omega)/\mathbb{R}$ . Next, the velocity  $\mathbf{u}^0 \in \mathcal{V}$  is given via Darcy's Law and  $p^1$  is given by formulation (3.26) respectively. Uniqueness of  $p^0$  and uniqueness of the solution of the cell problems induce uniqueness of  $p^1$  and  $\mathbf{u}^0$ .  $\square$

### 3.2.6. Two-Scale Convergence

In the previous section we proved the equivalence of the Stokes system with two pressures (3.16) and Darcy's Law. It remains to be shown that the solution  $(\mathbf{u}_\varepsilon, p_\varepsilon)$  of the Stokes system  $\mathcal{P}_\varepsilon$  converges to the solution of the two pressure Stokes system (3.16).

One possibility to do this is Tartar's energy method [57]. Despite the frequent success of this very general and powerful method, it is not entirely satisfactory for our homogenisation problem because it involves two partly redundant steps [31]: firstly, a heuristic derivation via the asymptotic expansion method and secondly a formal justification of the obtained homogenised problem. These steps have little in common, as for example, the energy method does not exploit the periodicity of the structure. Hence, an all-in-one method would in this situation be preferable. Such is the two-scale convergence method [11].

The two-scale convergence method is dedicated to periodic homogenisation, which makes it very efficient and simple in this context. In this method, multiplication of the equations satisfied by some  $\mathbf{u}_\varepsilon$  with an oscillating test function  $\Psi(x, x/\varepsilon)$ , and passing to the two-scale limit, automatically yields the homogenised result. Thus, we not only present the desired convergence result, but also explain a further method, with which we could have started at the beginning of this chapter. Our outline is based on the works of Allaire in [11, 10, 31]. The two-scale convergence method relies on the following result:

**Theorem 3.10** [TWO-SCALE CONVERGENCE]

Let  $h_\varepsilon$  be a bounded sequence in  $L^2(\Omega)$ , where  $\Omega$  is an open set in  $\mathbb{R}^n$ . Then there exists a subsequence  $\hat{h}_\varepsilon$  and a function  $h_0(x, y) \in L^2(\Omega \times Y)$  such that

$$\lim_{\varepsilon \rightarrow 0} \int_{\Omega} \hat{h}_\varepsilon(x) \Psi\left(x, \frac{x}{\varepsilon}\right) dx = \int_{\Omega} \int_Y h_0(x, y) \Psi(x, y) dy dx \quad (3.32)$$

for any function which  $\Psi \in C_0^\infty[\Omega, C_{\text{per}}^\infty(Y_F)]$ . Then we say that  $h_\varepsilon$  two-scale converges to  $h_0(x, y)$ .

A proof of this Lemma can be found in [11]. We also only cite here, that for any smooth  $Y$ -periodic function  $a(x, y)$ , the associated sequence  $a_\varepsilon(x) = a(x, \frac{x}{\varepsilon})$  two-scale converges to  $a(x, y)$ .

Let us again consider the steady Stokes equations in a porous medium  $\Omega_\varepsilon$  as given by (3.3). For their unique solution  $(\mathbf{u}_\varepsilon, p_\varepsilon) \in H_0^1(\Omega_\varepsilon)^n \times L^2(\Omega_\varepsilon) \setminus \mathbb{R}$  we have already established extensions  $(\tilde{\mathbf{u}}_\varepsilon, \tilde{p}_\varepsilon) \in H_0^1(\Omega)^n \times L^2(\Omega) \setminus \mathbb{R}$  of the velocity and the pressure in equations (3.5) and (3.6) respectively. Also, Lemma 3.1 gives bounds for the velocity and pressure. Hence, we are in the position to apply Theorem 3.10, and there exist three functions<sup>1</sup>  $\mathbf{u}_0(x, y)$  and  $\xi_0(x, y)$  in  $L^2(\Omega \times Y)^n$  as well as  $p_0(x, y)$  in  $L^2(\Omega \times Y)$  such that

$$\lim_{\varepsilon \rightarrow 0} \int_{\Omega} \frac{\tilde{\mathbf{u}}_\varepsilon(x)}{\varepsilon^2} \Psi\left(x, \frac{x}{\varepsilon}\right) dx = \int_{\Omega} \int_Y \mathbf{u}_0(x, y) \Psi(x, y) dy dx \quad (3.33)$$

$$\lim_{\varepsilon \rightarrow 0} \int_{\Omega} \nabla \frac{\tilde{\mathbf{u}}_\varepsilon(x)}{\varepsilon} \Xi\left(x, \frac{x}{\varepsilon}\right) dx = \int_{\Omega} \int_Y \xi_0(x, y) \Xi(x, y) dy dx \quad (3.34)$$

---

<sup>1</sup>Note here, that the two-scale limits  $\mathbf{u}_0(x, y)$  and  $p_0(x, y), p(x)$  are to be distinguished from the solution of the Stokes systems with two pressures  $\mathbf{u}^0(x, y)$  and  $p^0(x)$  by the position of the super/subscript respectively.

$$\lim_{\varepsilon \rightarrow 0} \int_{\Omega} \tilde{p}_{\varepsilon}(x) \Phi \left( x, \frac{x}{\varepsilon} \right) dx = \int_{\Omega} \int_Y p_0(x, y) \Phi(x, y) dy dx \quad (3.35)$$

for all  $\Psi, \Xi$  in  $C_0^{\infty}[\Omega, C_{\text{per}}^{\infty}(Y_F)^n]$  and  $\Phi$  in  $C_0^{\infty}[\Omega, C_{\text{per}}^{\infty}(Y_F)]$ . Here,  $C_0^{\infty}[\Omega, C_{\text{per}}^{\infty}(Y_F)]$  denotes the space of infinitely often differentiable and compactly supported functions in  $\Omega$  with values in the space  $C_{\text{per}}^{\infty}(Y_F)$ , which is the space of infinitely often differentiable  $Y$ -periodic functions in  $Y_F$ .

Thus, we show the following Lemma:

**Lemma 3.11** [PROPERTIES OF THE TWO-SCALE LIMITS]

Let  $\{\tilde{\mathbf{u}}_{\varepsilon}, \tilde{p}_{\varepsilon}\}$  denote the extensions of the solutions of the Stokes system and let their two-scale limits be given by equations (3.33-3.35). Then these limits satisfy  $\mathbf{u}_0(x, y) \in L^2[\Omega; H_{\text{per}}^1(Y)^n]$  and  $p_0(x, y) = p(x) \in L^2(\Omega/\mathbb{R})$  and

$$\nabla_y \cdot \mathbf{u}_0(x, y) = 0 \quad \text{in } \Omega \times Y \quad (3.36)$$

$$\nabla_x \cdot \left[ \int_Y \mathbf{u}_0(x, y) dy \right] = 0 \quad \text{in } \Omega \quad (3.37)$$

$$\left[ \int_{Y_F} \mathbf{u}_0(x, y) dy \right] \cdot \boldsymbol{\nu} = 0 \quad \text{on } \partial\Omega \quad (3.38)$$

$$\mathbf{u}_0(x, y) = 0 \quad \text{in } \Omega \times Y_S. \quad (3.39)$$

*Proof.* First we show that  $\boldsymbol{\xi}_0 = \nabla_y \mathbf{u}_0$  in equation (3.34). Integrating (3.34) by parts and passing to the limit yields

$$\begin{aligned} \lim_{\varepsilon \rightarrow 0} \int_{\Omega} \nabla \frac{\tilde{\mathbf{u}}_{\varepsilon}(x)}{\varepsilon} \Psi \left( x, \frac{x}{\varepsilon} \right) dx &= - \lim_{\varepsilon \rightarrow 0} \int_{\Omega} \frac{\tilde{\mathbf{u}}_{\varepsilon}(x)}{\varepsilon} \left[ \frac{1}{\varepsilon} \nabla_y \Psi \left( x, \frac{x}{\varepsilon} \right) + \nabla_x \Psi \left( x, \frac{x}{\varepsilon} \right) \right] dx \\ &= - \lim_{\varepsilon \rightarrow 0} \int_{\Omega} \frac{\tilde{\mathbf{u}}_{\varepsilon}(x)}{\varepsilon^2} \left[ \nabla_y \Psi \left( x, \frac{x}{\varepsilon} \right) + \varepsilon \nabla_x \Psi \left( x, \frac{x}{\varepsilon} \right) \right] dx \\ &= - \int_{\Omega} \int_Y \mathbf{u}_0(x, y) \nabla_y \Psi(x, y) dy dx \\ &= \int_{\Omega} \int_Y \nabla_y \mathbf{u}_0(x, y) \Psi(x, y) dy dx, \end{aligned}$$

establishing that  $\nabla \tilde{\mathbf{u}}_{\varepsilon}$  converges to  $\nabla \mathbf{u}_0$  and  $\mathbf{u}_0(x, y) \in L^2[\Omega; H_{\text{per}}^1(Y)^n]$ .

Next, we show that the two-scale limit of  $\tilde{p}_{\varepsilon}$  does not depend on  $y$  by multiplying the first of the Stokes equations (3.3) by  $\varepsilon \Psi(x, \frac{x}{\varepsilon})$  with  $\Psi(x, \frac{x}{\varepsilon}) \in C_0^{\infty}[\Omega, C_{\text{per}}^{\infty}(Y_F)^n]$

$$\begin{aligned} \lim_{\varepsilon \rightarrow 0} \int_{\Omega} \mathbf{f} \varepsilon \Psi \left( x, \frac{x}{\varepsilon} \right) dx &= \lim_{\varepsilon \rightarrow 0} \int_{\Omega} [\nabla \tilde{p}_{\varepsilon} - \mu \Delta \tilde{\mathbf{u}}_{\varepsilon}] \varepsilon \cdot \Psi \left( x, \frac{x}{\varepsilon} \right) dx \\ &= - \lim_{\varepsilon \rightarrow 0} \int_{\Omega} \tilde{p}_{\varepsilon} \varepsilon \operatorname{div}_x \Psi \left( x, \frac{x}{\varepsilon} \right) dx + \lim_{\varepsilon \rightarrow 0} \int_{\Omega} \mu \nabla \tilde{\mathbf{u}}_{\varepsilon} \varepsilon \cdot \nabla \Psi \left( x, \frac{x}{\varepsilon} \right) dx \\ &= - \lim_{\varepsilon \rightarrow 0} \int_{\Omega} \tilde{p}_{\varepsilon} \varepsilon \left[ \frac{1}{\varepsilon} \operatorname{div}_y \Psi \left( x, \frac{x}{\varepsilon} \right) + \operatorname{div}_x \Psi \left( x, \frac{x}{\varepsilon} \right) \right] \\ &\quad + \lim_{\varepsilon \rightarrow 0} \int_{\Omega} \mu \nabla \frac{\tilde{\mathbf{u}}_{\varepsilon}}{\varepsilon} \left[ \varepsilon \nabla_y \Psi \left( x, \frac{x}{\varepsilon} \right) + \varepsilon^2 \nabla_x \Psi \left( x, \frac{x}{\varepsilon} \right) \right]. \end{aligned}$$

Passing to the limit this equation becomes

$$0 = - \int_{\Omega} \int_Y p_0(x, y) \operatorname{div}_y \Psi(x, y) dy dx + 0.$$

Another integration by parts shows that  $\nabla_y p_0(x, y) = 0$ . Thus, there exists  $p(x) \in L^2(\Omega)/\mathbb{R}$  such that  $p_0(x, y) = p(x)$  independent of  $y$ .

Now we will prove the four properties of the two-scale limits (3.36-3.39).

**ad 3.36** Multiplication of the continuity equation of the Stokes system with  $\Psi(x, \frac{x}{\varepsilon})/\varepsilon$  yields

$$0 = \lim_{\varepsilon \rightarrow 0} \int_{\Omega} \operatorname{div}_x \tilde{\mathbf{u}}_{\varepsilon}(x) \frac{\Psi(x, \frac{x}{\varepsilon})}{\varepsilon} dx = \int_{\Omega} \int_Y \mathbf{u}_0(x, y) \operatorname{div}_y \Psi(x, y) dy dx,$$

which establishes  $\operatorname{div}_y \mathbf{u}_0(x, y) = 0$ .

**ad 3.37** If we test the continuity equation with  $\Psi(x)/\varepsilon^2$ , where  $\Psi \in C_0^{\infty}$ , we obtain

$$\begin{aligned} 0 &= \lim_{\varepsilon \rightarrow 0} \int_{\Omega} \operatorname{div}_x \tilde{\mathbf{u}}_{\varepsilon}(x) \frac{\Psi(x)}{\varepsilon^2} dx = \int_{\Omega} \int_Y \mathbf{u}_0(x, y) \nabla_x \Psi(x) dy dx \\ &= \int_{\Omega} \Psi(x) \operatorname{div}_x \int_Y \mathbf{u}_0(x, y) dy dx \end{aligned}$$

and hence,  $\operatorname{div}_x \int_Y \mathbf{u}_0(x, y) dy = 0$ .

**ad 3.38** If in the above equation we now only take<sup>2</sup> a  $Y$ -periodic function  $\Psi \in L^2(\Omega)$ , then integration by parts yields

$$0 = \int_{\Omega} \int_Y \mathbf{u}_0(x, y) \nabla_x \Psi(x) dy dx + \int_{\partial\Omega} \int_Y \mathbf{u}_0(x, y) \Psi(x) \cdot \boldsymbol{\nu}(x) dy dS,$$

which is fulfilled if  $\boldsymbol{\nu}(x) \cdot \int_Y \mathbf{u}_0(x, y) dy = 0$ .

**ad 3.39** Taking a function  $\Psi \in C_0^{\infty}(\Omega; C_{\text{per}}^{\infty})$  with  $\Psi(\cdot, y) = 0$  for all  $y \in Y_F$  we obtain

$$0 = \lim_{\varepsilon \rightarrow 0} \int_{\Omega} \frac{\mathbf{u}_0(x, y)}{\varepsilon^2} \Psi\left(x, \frac{x}{\varepsilon}\right) dx = \int_{\Omega} \int_{Y_S} \mathbf{u}_0(x, y) \Psi(x, y) dy dx$$

and hence  $\mathbf{u}_0 = 0$  almost everywhere on  $\Omega \times Y_S$ .

□

From this Theorem it follows immediately that the two-scale limit  $\mathbf{u}_0(x, y)$  is in the space  $\mathcal{V}$  as defined by (3.27). The next step in the two-scale convergence method is to multiply the Stokes equation  $\mathcal{P}_{\varepsilon}$  by a function  $\Psi$  which has the same form as the two-scale limit  $\mathbf{u}_0(x, y)$  given by Lemma 3.11. But first, we need the following lemma:

<sup>2</sup>The test function in the two-scale convergence does not have to be very smooth (cf. [10]).

**Lemma 3.12**

Let  $\mathcal{V}$  be the subspace of  $L^2(\Omega; \mathcal{V}_Y)$ , where  $\mathcal{V}$  and  $\mathcal{V}_Y$  are defined by equations (3.27) and (3.17) respectively. The orthogonal  $\mathcal{V}^\perp$  of  $\mathcal{V}$ , with respect to the usual scalar product in  $L^2(\Omega \times Y_F)$ , is a subspace of the dual space  $L^2(\Omega, H_{\text{per}}^{-1}(Y_F)^n)$  and has the following characterisation

$$V^\perp = \{\nabla_x \varphi(x) + \nabla_y \varphi_1(x, y) \text{ with } \varphi \in H^1(\Omega) \setminus \mathbb{R} \text{ and } \varphi_1 \in L^2(\Omega; \mathcal{Q})\}.$$

This Lemma's proof can be found in ([31]). Finally we obtain the following theorem:

**Theorem 3.13**

The extension  $(\tilde{\mathbf{u}}_\varepsilon, \tilde{p}_\varepsilon)$  of the solution of the Stokes equations two-scale converges to the unique solution  $(\mathbf{u}_0, p)$  of the Stokes system with two pressures (3.16).

*Proof.* We choose a test function  $\Psi(x, y) \in C_0^\infty[\Omega, C_{\text{per}}^\infty(Y_F)^n]$  with  $\Psi(x, y) = 0$  in  $\Omega \times Y_S$ . Furthermore we assume that  $\Psi$  satisfies the incompressibility conditions  $\text{div}_y \Psi(x, y) = 0$  and  $\text{div}_x \int_Y \Psi(x, y) dy = 0$ . We multiply this function with the first equation of the Stokes system and obtain

$$\begin{aligned} & \lim_{\varepsilon \rightarrow 0} \int_{\Omega_\varepsilon} \mathbf{f}(x) \Psi \left( x, \frac{x}{\varepsilon} \right) dx \\ &= \lim_{\varepsilon \rightarrow 0} \int_{\Omega_\varepsilon} (\nabla p_\varepsilon - \mu \Delta \mathbf{u}_\varepsilon) \Psi \left( x, \frac{x}{\varepsilon} \right) dx \\ &= - \lim_{\varepsilon \rightarrow 0} \int_{\Omega_\varepsilon} p_\varepsilon \text{div}_x \Psi \left( x, \frac{x}{\varepsilon} \right) + \mu \nabla \frac{\mathbf{u}_\varepsilon}{\varepsilon} \left[ \nabla_y \Psi \left( x, \frac{x}{\varepsilon} \right) + \varepsilon \nabla_x \Psi \left( x, \frac{x}{\varepsilon} \right) \right] dx. \end{aligned}$$

In these equations we can replace  $\Omega_\varepsilon$  by  $\Omega$  as  $\Psi$  is zero in  $\Omega \setminus \Omega_\varepsilon$ . Hence, we can use the two-scale convergence limits (3.34 -3.35) and their properties of Lemma 3.11. When passing to the two-scale limit the pressure term vanishes, because the two-scale limit of  $p_\varepsilon$  does not depend on  $y$  and  $\text{div}_x \int_Y \Psi(x, y) dy = 0$

$$- \lim_{\varepsilon \rightarrow 0} \int_{\Omega} p_\varepsilon \text{div}_x \Psi \left( x, \frac{x}{\varepsilon} \right) = \int_{\Omega} \int_Y p(x) \text{div}_x \Psi \left( x, \frac{x}{\varepsilon} \right) dx dy = 0. \quad (3.40)$$

The limits of the other terms contribute

$$\int_{\Omega} \int_{Y_F} \nabla_y \mathbf{u}_0(x, y) \nabla_y \Psi(x, y) dy dx = \int_{\Omega} \int_{Y_F} \mathbf{f}(x) \Psi(x, y) dy dx. \quad (3.41)$$

The above chosen test functions form a space which is dense in  $\mathcal{V}$ . Using this density argument the variational formulation (3.41) holds for all  $\Psi \in \mathcal{V}$ . In the Hilbert space  $\mathcal{V}$  Lax Milgram's Lemma is applicable and admits a unique solution  $\mathbf{u}^0 \in \mathcal{V}$ . Furthermore, by Lemma 3.12, we know that the orthogonal of  $\mathcal{V}$  is made of gradients of the form

$$\nabla_x \varphi(x) + \nabla_y \varphi_1(x, y) \text{ with } \varphi \in H^1(\Omega) \setminus \mathbb{R} \text{ and } \varphi_1 \in L^2(\Omega; \mathcal{Q}).$$

Thus, there exist such  $\varphi$  and  $\varphi_1$  that

$$\begin{aligned} & \int_{\Omega} \int_{Y_F} \nabla_y \mathbf{u}_0(x, y) \nabla_y \Psi(x, y) dy dx - \int_{\Omega} \int_{Y_F} \mathbf{f}(x) \Psi(x, y) dy dx \\ &= \int_{\Omega} \int_{Y_F} (\nabla_x \varphi(x) + \nabla_y \varphi_1(x, y)) \Psi(x, y) dy dx, \end{aligned} \quad (3.42)$$

with which the variational formulation (3.41) becomes equivalent to the two pressure Stokes system.

Furthermore, in order to obtain a comparable result for the convergence of  $p_\varepsilon$  we choose a test function  $\Psi(x, y) \in C_0^\infty[\Omega, C_{\text{per}}^\infty(Y_F)^n]$  with  $\Psi(x, y) = 0$  in  $\Omega \times Y_S$ . Furthermore, we assume that  $\Psi$  satisfies only the incompressibility condition for  $y$ , namely  $\text{div}_y \Psi(x, y) = 0$ . Again, we multiply this function by the first equation of the Stokes system and obtain in the limit

$$\begin{aligned} & \int_{\Omega} \int_{Y_F} \nabla_y \mathbf{u}_0(x, y) \nabla_y \Psi(x, y) dy dx - \int_{\Omega} \int_{Y_F} p(x) \text{div}_x \Psi(x, y) dy dx \\ &= \int_{\Omega} \int_{Y_F} \mathbf{f}(x) \Psi(x, y) dy dx. \end{aligned} \quad (3.43)$$

Since by Theorem 3.9 the two pressure Stokes system admits a unique solution, all sequences and subsequences  $(\tilde{\mathbf{u}}_\varepsilon, p_\varepsilon)$  converge to the same solution  $(\mathbf{u}_0, p)$ .  $\square$

We have established the two-scale convergence<sup>3</sup> of the solution  $(\mathbf{u}_\varepsilon, p_\varepsilon)$  of the Stokes system  $\mathcal{P}_\varepsilon$  to the solution  $(\mathbf{u}_0, p_0)$  of the two pressure Stokes system (3.16). This result concludes the homogenisation of the Stokes equations and the proof of Theorem 3.2.

In the following we will see that depending on the scaling of the obstacles in the porous medium, other limit flow regimes appear. Hence, we will try and give an answer to the question, which of these should be the macroscopic model of choice for our range of applications. Then we will give an overview about homogenisation results obtainable when starting with the nonlinear Navier-Stokes instead of the linear Stokes equations.

### 3.3. Derivation of Brinkman's Law

So far we have shown that the homogenisation of the Stokes equations leads to Darcy's Law with the assumption that the obstacle size  $a_\varepsilon$  is of the same order of magnitude as the period  $\varepsilon$ . Contrary, in the following we will assume that  $a_\varepsilon$  passes faster to zero than  $\varepsilon$

$$a_\varepsilon \ll \varepsilon \text{ and } \lim_{\varepsilon \rightarrow 0} \frac{a_\varepsilon}{\varepsilon} = 0. \quad (3.44)$$

The first of these assumptions is not necessary to obtain the homogenisation results but will be justified in Section 3.5. Depending on the scaling of this  $a_\varepsilon$  there are three different limit flow regimes represented by three different macroscopic equations. For a so-called critical

<sup>3</sup>The two-scale convergence is a result, which is stronger than the weak convergence but weaker than the strong convergence. However, the first proof of the strong convergence in  $L^2$  is given by Allaire in [6].

size (e.g.  $a_\varepsilon = \varepsilon^3$  in the three-dimensional case), the homogenised problem is a Brinkman's Law. For larger obstacles we find again Darcy's Law, but a considerably different one than we have obtained previously. On the other hand, if the obstacles are very small, the macroscopic problem reduces to the initial Stokes equations. In the derivation of these macroscopic equations we will follow Allaire's works [7] and [8] to which we also refer to for the proof of Theorem 3.15.

Let us begin with the definition of the critical obstacle size  $a_\varepsilon^{\text{crit}}$ .

**Definition 3.14** [CRITICAL SIZE OF THE OBSTACLES]

The so-called critical obstacle size  $a_\varepsilon^{\text{crit}}$  is defined by

$$\begin{cases} a_\varepsilon^{\text{crit}} \equiv C \cdot \varepsilon^{\frac{n}{n-2}} & \text{for } n \geq 3 \\ a_\varepsilon^{\text{crit}} \equiv e^{-\frac{C}{\varepsilon^2}} & \text{for } n = 2, \end{cases}$$

where  $C$  is a strictly positive constant. Furthermore, we define the ratio  $\sigma_\varepsilon$  between the current and the critical obstacle size

$$\begin{cases} \sigma_\varepsilon \equiv \left( \frac{\varepsilon^n}{a_\varepsilon^{\text{crit}}} \right)^{\frac{1}{2}} & \text{for } n \geq 3 \\ \sigma_\varepsilon \equiv \varepsilon \cdot \left| \log \left( \frac{a_\varepsilon}{a_\varepsilon^{\text{crit}}} \right) \right|^{\frac{1}{2}} & \text{for } n = 2. \end{cases}$$

**Theorem 3.15** [HOMOGENISED STOKES EQUATIONS FOR SMALL OBSTACLES]

There are three different limit flow regimes depending on the size of the obstacles.

1. If  $\lim_{\varepsilon \rightarrow 0} \sigma_\varepsilon = +\infty$ , then  $(\mathbf{u}_\varepsilon, p_\varepsilon)$  converges strongly to  $(\mathbf{u}, p)$  in  $[H_0^1(\Omega)]^n \times [L^2(\Omega)/\mathbb{R}]$ , where  $(\mathbf{u}, p)$  is the unique solution of the Stokes equations

$$\begin{aligned} \nabla p - \mu \Delta \mathbf{u} &= f & \text{in } \Omega \\ \nabla \cdot \mathbf{u} &= 0 & \text{in } \Omega \\ \mathbf{u} &= 0 & \text{on } \partial\Omega. \end{aligned} \tag{3.45}$$

2. If  $\lim_{\varepsilon \rightarrow 0} \sigma_\varepsilon = \sigma > 0$ , then  $(\mathbf{u}_\varepsilon, p_\varepsilon)$  converges weakly to  $(\mathbf{u}, p)$  in  $[H_0^1(\Omega)]^n \times [L^2(\Omega)/\mathbb{R}]$ , where  $(\mathbf{u}, p)$  is the unique solution of the Brinkman-type equations

$$\begin{aligned} \nabla p - \mu \Delta \mathbf{u} + \frac{\mu}{\sigma^2} \mathbf{M} \mathbf{u} &= f & \text{in } \Omega \\ \nabla \cdot \mathbf{u} &= 0 & \text{in } \Omega \\ \mathbf{u} &= 0 & \text{on } \partial\Omega. \end{aligned} \tag{3.46}$$

3. If  $\lim_{\varepsilon \rightarrow 0} \sigma_\varepsilon = 0$ , then  $(\frac{\mathbf{u}_\varepsilon}{\sigma_\varepsilon}, p_\varepsilon)$  converges strongly to  $(\mathbf{u}, p)$  in  $[L^2(\Omega)]^n \times [L^2(\Omega)/\mathbb{R}]$ , where  $(\mathbf{u}, p)$  is the unique solution of the Darcy equations

$$\begin{aligned} \mathbf{u} &= \frac{\mathbf{M}^{-1}}{\mu} (f - \nabla p) & \text{in } \Omega \\ \nabla \cdot \mathbf{u} &= 0 & \text{in } \Omega \\ \mathbf{u} &= 0 & \text{on } \partial\Omega. \end{aligned} \tag{3.47}$$

In the first case of Theorem 3.15 the obstacles are too small and the limit flow regime is again Stokes flow. If the size of the obstacles is critical as in the second case, a supplementary term has to be treated in the Stokes equations. In the third case, the obstacles are comparably large and Stokes flow degenerates into Darcy flow.

Note again that Darcy's Law in Theorem 3.2 has little to do with the one derived in Theorem 3.15 here. Actually, the permeability tensors  $\mathbf{K}$  and  $\mathbf{M}^{-1}$  take in both cases different values and are computed by different Unit Cell Problems around the model obstacle  $Y_S$ . Indeed, for the computation of  $\mathbf{M}$  the local problem occurs in the entire space around the obstacle, and no longer only in the unit period of the porous medium with a periodic boundary condition, when the obstacle and the period have the same size  $\varepsilon$ . See [7] for a definition of the local problems and of  $\mathbf{M}$ .

However, from a physical point it seems rather odd that the permeability tensor should be the same for a large range of obstacle sizes smaller than the period but should mysteriously differ when the obstacle size is equal to the period. Accordingly, Allaire shows in [6] that there is an actual continuity of the permeability tensor, which we will shortly present here. Let us denote the obstacle size in the rescaled unit cell by  $\eta$ , which is a constant during the homogenisation process. After taking the homogenisation limit we can take a second, the so-called low-volume fraction limit, in which we let  $\eta$  go to zero. Within this second limit process, Allaire shows that the permeability tensor  $\mathbf{K}(\eta)$  converges to the permeability tensor  $\mathbf{M}^{-1}$  after a suitable rescaling. That is,

$$\begin{cases} \lim_{\eta \rightarrow 0} \eta^{n-2} \mathbf{K}(\eta) = \mathbf{M}^{-1} & \text{for } n \geq 3 \\ \lim_{\eta \rightarrow 0} \frac{1}{|\log \eta|} \mathbf{K}(\eta) = \mathbf{M}^{-1} & \text{for } n = 2. \end{cases}$$

### 3.4. Slip Boundary Conditions on the Obstacles

For our model problem of the Stokes equations we have investigated no-slip conditions on the obstacles. In one of the works of Allaire [9] the Stokes equations are provided with a slip boundary conditions on the very small obstacles  $a_\varepsilon$ : for  $1 \leq i \leq N(\varepsilon)$

$$\begin{aligned} \mathbf{u}_\varepsilon \cdot \boldsymbol{\nu} &= 0 && \text{on } \partial Y_{\tilde{S}_i}^\varepsilon \\ \frac{\alpha}{a_\varepsilon} \mathbf{u}_\varepsilon &= 2 \left( \frac{\partial \mathbf{u}_\varepsilon}{\partial \boldsymbol{\nu}} \cdot \boldsymbol{\nu} \right) \boldsymbol{\nu} - (\nabla \mathbf{u}_\varepsilon + \nabla^T \mathbf{u}_\varepsilon) \boldsymbol{\nu} && \text{on } \partial Y_{\tilde{S}_i}^\varepsilon \\ \mathbf{u}_\varepsilon &= 0 && \text{on } \partial \Omega. \end{aligned} \tag{3.48}$$

where the slip coefficient  $\alpha$  is a positive constant. The first of these equations expresses that the fluid does not flow through the obstacles and the second equation balances the tangential components of the velocity and the infinitesimal force exerted by the fluid on the obstacle. Roughly speaking, Theorem 3.15 is still applicable, but the Unit Cell Problem is different and thus also the permeability tensor  $\mathbf{M}$ .

From a physical point of view Allaire shows in his article that the slowing effect is mainly due to the fact that the fluid does not penetrate the obstacles (the normal component of the velocity is zero) rather than to the fact that it sticks to the obstacles (the tangential component is zero because of a no-slip condition). However, in this thesis, no-slip bound-

aries are taken into account only.

The question that now arises is, of course, which macroscopic model should be chosen, for e.g. modelling fluid flow in textiles.

### 3.5. On the Choice of the Appropriate Macroscopic Model

In the previous sections we have seen that for one and the same problem (3.3) four different macroscopic flow regimes can be derived. In order to understand which of these should be the limit model of choice, we will take a more practical view on homogenisation, following Laptev [34].

Normally, the main purpose in homogenisation theory is to obtain the limit problem for  $\varepsilon \rightarrow 0$ . In this section we suppose that our main purpose lies in finding a good approximation of a given problem  $\mathcal{P}$ . Thus, we will consider the limit problems as just one way to obtain this approximation. More precisely, we construct a sequence of imaginary problems  $\{\mathcal{P}^\varepsilon\}$ , where  $\varepsilon \in \{\varepsilon^n : \lim_{n \rightarrow \infty} \varepsilon^n = 0\}$ , such that one of them,  $\mathcal{P}^{\bar{\varepsilon}}$ , is the problem  $\mathcal{P}$  itself. If the series is in some sense convergent to some limit problem  $\mathcal{P}^0$  and if this solution can be obtained with moderate requirement on resources, as opposed to the computation of the solutions of  $\{\mathcal{P}^\varepsilon\}$ , then  $\mathcal{P}^0$  can be used to approximate the solutions of  $\{\mathcal{P}^\varepsilon\}$  and, in particular, of  $\mathcal{P}^{\bar{\varepsilon}}$ .

As an example, let us again consider a Stokes problem in  $\Omega$  with a fixed period  $\bar{\varepsilon}$  and obstacle size  $\bar{a}$  as the problem  $\mathcal{P} = \mathcal{P}^{\bar{\varepsilon}}$  which we wish to approximate. Furthermore, let us define the Stokes problems in  $\Omega_\varepsilon$  with varying  $\varepsilon$  define our series of imaginary problems  $\{\mathcal{P}^\varepsilon\}$ . Then, the limit problem  $\mathcal{P}^0$  is for a suitable assumption on the scaling of the obstacles Darcy's Law (3.2).

The convergence of problems, as Laptev [34] puts it, is not precisely defined, although it is strongly related to the weak or strong convergence of the problems' solutions. In fact, convergence alone does not guarantee a good approximation of our given problem  $\mathcal{P}^{\bar{\varepsilon}}$ , since  $\bar{\varepsilon}$  itself cannot be made smaller as it is.  $\bar{\varepsilon}$  might be too large, to be reasonably approximated by  $\mathcal{P}^0$ , as for example, drawn in the following schematic convergence diagram. If  $n$  were small compared to the number of steps  $\#n$  needed before the limit  $\mathcal{P}^0$  is reached,  $\mathcal{P}^0$  would be a very bad approximation of  $\mathcal{P}^{\bar{\varepsilon}}$ .

$$\mathcal{P}^{\varepsilon^0}, \dots, \mathcal{P}^{\varepsilon^{n-1}}, \underbrace{\mathcal{P}^{\varepsilon^n}, \mathcal{P}^{\varepsilon^{n+1}}, \dots}_{=\mathcal{P}^{\bar{\varepsilon}}=\mathcal{P}} \longrightarrow \mathcal{P}^0.$$

Ideally, the computation of  $\mathcal{P}$  can be done directly, giving us an estimation of the error  $E(\varepsilon)$  when approximating one of the problems  $\mathcal{P}^\varepsilon$  by  $\mathcal{P}^0$ . This error would also indicate a range of microstructural problems for which the approximation by  $\mathcal{P}^0$  is admissible. If our particular problem does not lie within this range we have to try to improve the approximation, by e.g. constructing another sequence  $\tilde{\mathcal{P}}^\varepsilon$  with another limit problem  $\tilde{\mathcal{P}}^0$  or by taking into account lower order terms in the asymptotic expansion. For an example of such an improvement compare Section 3.6.3 for the case  $\gamma > 1$ : here, a nonlinear Darcy Law is obtained by including lower order terms in the asymptotic expansion of the Navier-Stokes equations.

Towards the end of our homogenisation analysis of the Stokes equations, we are in a way confronted with the opposite problem. We have already given two different sequences of

problems  $\{\mathcal{P}^\varepsilon\}$  and  $\{\tilde{\mathcal{P}}^\varepsilon\}$ , the first converging to Darcy's Law and the second converging to three different limit problems when  $\lim_{\varepsilon \rightarrow 0} a_\varepsilon/\varepsilon = 0$ . Now, we have to decide which of these models meets our needs best. Therefore, let us have a closer look at the Stokes problem  $\mathcal{P}$  with a fixed period  $\bar{\varepsilon}$  and obstacle size  $\bar{a}$ . In addition, we assume  $\bar{a} < \bar{\varepsilon}$  but not necessarily  $\bar{a} \ll \bar{\varepsilon}$ . Then it is possible to choose a function  $a(\varepsilon)$  for  $n \geq 3$  such that

$$a(\varepsilon) = \left[ \frac{\bar{a}}{\bar{\varepsilon}^\gamma} \right] \varepsilon^\gamma \text{ and } \sigma(\varepsilon) = \left[ \frac{\bar{\varepsilon}^\gamma}{\bar{a}} \right]^{\frac{n-2}{2}} \varepsilon^{(n-\gamma(n-2))/2},$$

where  $\gamma \in \mathbb{N} \setminus \{0\}$ . These functions suggest obstacle sizes for the problems  $\tilde{\mathcal{P}}^\varepsilon$  and the so constructed sequence satisfies the condition  $\tilde{\mathcal{P}}^{\bar{\varepsilon}} = \mathcal{P}$  since then  $a(\bar{\varepsilon}) = \bar{a}$ . The limit problem can be controlled by the choice of  $\gamma$  (cf. Theorem 3.15): Brinkman flow for  $\gamma = n/(n-2)$ , Darcy flow for  $1 < \gamma < n/(n-2)$  and Stokes flow for  $\gamma > n/(n-2)$ . Hence, different choices of  $\gamma$  lead to different sequences  $\{\tilde{\mathcal{P}}^\varepsilon\}$  and different limit problems, all supposedly an approximation for the same solution of  $\mathcal{P}$ . If we can compute the solution of  $\mathcal{P}$  directly, we can check which of these approximations are better than others, otherwise the choice of the appropriate macroscopic model for  $\mathcal{P}$  is not easy.

Let us try and find a range of actual obstacle sizes  $\bar{\varepsilon}$  for which  $\tilde{\mathcal{P}}^0$  and  $\mathcal{P}^0$  might offer a good approximation. Especially, for the scaling of the obstacles in the sequence  $\{\tilde{\mathcal{P}}^\varepsilon\}$ , where the size of the obstacles goes to zero faster than in the sequence  $\{\mathcal{P}^\varepsilon\}$ , a situation is imaginable in which  $\tilde{\mathcal{P}}^\varepsilon$  is a member of the sequence, but the limit  $\tilde{\mathcal{P}}^0$  is still far away. This means, that the approximation by  $\tilde{\mathcal{P}}^0$  works well, if we additionally assume that  $\bar{\varepsilon}$  is very small. But in this case, porous media fulfilling this condition are nearly an idealisation: Such a porous medium would have to have a porosity extremely close to one, which is not realistic for natural media and also not for textiles. Therefore, the Darcy model obtained with the sequence  $\{\mathcal{P}^\varepsilon\}$  will be valid for a more natural range of obstacle sizes, and if possible, we will try and justify its use by comparison of the solutions  $\mathcal{P}^0$  and  $\mathcal{P}$  throughout this thesis (cf. Chapter 7).

However, the Brinkman model can be rehabilitated as an approximation to Darcy's Law if we use the same Darcy permeability  $\mathbf{K}$  (3.12). This permeability will be very small since  $\bar{\varepsilon}$  will be small compared to the length  $L$  of the porous medium. Thus, the term  $\mu \mathbf{K}^{-1} \mathbf{u}$  may dominate over the viscosity term  $\mu \Delta \mathbf{u}$  in the porous part of the medium and Brinkman's Law will reduce to Darcy's Law there. We discuss this interesting question in Section 7.4.1 for a numerical example.

### 3.6. Homogenisation of the Navier-Stokes Equations

We could also start from a microscopical problem  $\mathcal{P}$ , where flow is governed by the Navier-Stokes instead of the Stokes equations. Here, the viscosity  $\mu$ , which we have always assumed to be constant, plays an important role in identifying the limit flow regimes. In a practical problem,  $\mu$  might take a small value and has to be considered as a parameter in the asymptotic expansion.

### 3.6.1. Homogenisation of the Nonstationary Navier-Stokes Equations

For the moment, assume that  $\mu$  is still constant and that the obstacle size  $a_\varepsilon$  scales with the order of the period  $\varepsilon$ . Let  $Y = ]0, 1[^n$  be the standard unit cell and  $Y_S \subset Y$ , the solid part of the unit cell, be an open set strictly contained in  $Y$  and locally placed on one side of its boundary  $S$ . We define by

$$Y_S^\varepsilon = \bigcup_{i=1}^{N(\varepsilon)} Y_{S_i}^\varepsilon$$

the union of solid parts of the porous medium and their boundaries. Furthermore, let  $\Omega \subset \mathbb{R}^n$  be a bounded domain locally placed on one side of its boundary  $\Gamma$ , let  $\mathbf{u}_\varepsilon$ ,  $p_\varepsilon$  and  $\mu > 0$  denote the velocity, pressure and viscosity of the fluid and let  $\mathbf{f}_\varepsilon$  be an external body force. Then the Navier-Stokes equations read

$$\begin{aligned} \frac{\partial \mathbf{u}_\varepsilon}{\partial t} + (\mathbf{u}_\varepsilon \cdot \nabla) \mathbf{u}_\varepsilon + \nabla p_\varepsilon - \mu \Delta \mathbf{u}_\varepsilon &= \mathbf{f}_\varepsilon & \text{in } \Omega_\varepsilon \times (0, T) \\ \nabla \cdot \mathbf{u}_\varepsilon &= 0 & \text{in } \Omega_\varepsilon \times (0, T) \\ \mathbf{u}_\varepsilon &= 0 & \text{on } \partial\Omega_\varepsilon \times (0, T) \\ \mathbf{u}_\varepsilon(x, 0) &= \mathbf{u}_\varepsilon^0(x) & \text{in } \Omega_\varepsilon, \end{aligned} \quad (3.49)$$

where  $\mathbf{u}_\varepsilon^0$  is a given initial velocity. For a given Banach space  $\mathcal{X}$  we introduce the spaces

$$L^\beta(0, T; \mathcal{X}) := \{u : [0, T] \rightarrow \mathcal{X} \text{ such that } \int_0^T \|u(t, \cdot)\|_{\mathcal{X}}^\beta dt < \infty\}.$$

Further, for a given bounded domain  $\mathcal{D} \subset \mathbb{R}^n$  we define  $H^{1/2}(\partial\mathcal{D})$  as the image of  $H^1(\mathcal{D})$  under the trace operator.

The article [44] is then devoted to the proof of the following Theorem:

**Theorem 3.16**

*There exists an extension  $\tilde{p}_\varepsilon \in L^\infty(0, T; L^\beta(\Omega)/\mathbb{R})$  of the function  $p^\varepsilon$  such that*

$$\begin{aligned} \mathbf{u}_\varepsilon &\rightharpoonup \mathbf{u} & \text{weakly in } L^2(\Omega \times (0, T))^n \\ \varepsilon^2 \frac{\partial}{\partial t} \tilde{p}_\varepsilon &\rightharpoonup p & \text{weakly in } H^{-1}(0, T; L^\beta(\Omega)/\mathbb{R}), \end{aligned}$$

where  $(\mathbf{u}, p)$  is the solution of the homogenised problem

$$\begin{aligned} \mathbf{u} &= \frac{\mathbf{K}}{\mu} (\mathbf{f} - \nabla p) & \text{in } \Omega \times (0, T) \\ \nabla \cdot \mathbf{u} &= 0 & \text{in } \Omega \times (0, T) \\ \mathbf{u} \cdot \boldsymbol{\nu} &= 0 & \text{in } L^2(0, T; H^{1/2}(\Gamma)), \end{aligned} \quad (3.50)$$

and the entries of the permeability tensor  $K_{ij} = \int_Y w_j^i dy$  are given by the standard Unit Cell Problem (3.3).

**Remark:** Actually Mikelić [44] considers the Navier-Stokes equations with a nonhomoge-

neous boundary

$$\begin{aligned} \mathbf{u}_\varepsilon &= 0 && \text{on } \partial\Omega_\varepsilon \setminus \Gamma \times (0, T) \\ \mathbf{u}_\varepsilon &= \mathbf{h} && \text{on } \Gamma \times (0, T), \end{aligned}$$

where  $\mathbf{h}$  is a function satisfying  $\int_\Gamma \mathbf{h}(\cdot, t) \cdot \boldsymbol{\nu} \, d\Gamma = 0$ . Then the Neumann boundary condition in Darcy's Law changes to

$$\mathbf{u} \cdot \boldsymbol{\nu} = \mathbf{h} \cdot \boldsymbol{\nu} \text{ in } L^2(0, T; H^{1/2}(\Gamma)).$$

### 3.6.2. Derivation of the Nonlinear Brinkman Law

In the next setting we consider the homogenisation of the steady-state Navier-Stokes equations for very small obstacles

$$a_\varepsilon \ll \varepsilon \text{ and } \lim_{\varepsilon \rightarrow 0} \frac{a_\varepsilon}{\varepsilon} = 0. \quad (3.51)$$

In this case, the homogenisation proceeds like in the case of the Stokes equations, as the non-linear term can be handled as a perturbation of the Stokes equations. The following theorem and its proof can be found in the works of Allaire [7, 8] respectively. For the definition of the critical obstacle size  $\sigma_\varepsilon$  we refer to Section 3.3.

**Theorem 3.17** [HOMOGENISED NAVIER-STOKES EQUATIONS FOR SMALL OBSTACLES]

*There are three different limit flow regimes depending on the scaling of the obstacles.*

1. *If  $\lim_{\varepsilon \rightarrow 0} \sigma_\varepsilon = +\infty$ , then  $(\mathbf{u}_\varepsilon, p_\varepsilon)$  converges strongly to  $(\mathbf{u}, p)$  in  $[H_0^1(\Omega)]^n \times [L^2(\Omega)/\mathbb{R}]$ , where  $(\mathbf{u}, p)$  is the unique solution of the Navier-Stokes equations*

$$\begin{aligned} \nabla p + \mathbf{u} \cdot \nabla \mathbf{u} - \mu \Delta \mathbf{u} &= f && \text{in } \Omega \\ \nabla \cdot \mathbf{u} &= 0 && \text{in } \Omega \\ \mathbf{u} &= 0 && \text{on } \partial\Omega. \end{aligned} \quad (3.52)$$

2. *If  $\lim_{\varepsilon \rightarrow 0} \sigma_\varepsilon = \sigma > 0$ , then  $(\mathbf{u}_\varepsilon, p_\varepsilon)$  converges weakly to  $(\mathbf{u}, p)$  in  $[H_0^1(\Omega)]^n \times [L^2(\Omega)/\mathbb{R}]$ , where  $(\mathbf{u}, p)$  is the solution of the non-linear Brinkman-type law*

$$\begin{aligned} \nabla p + \mathbf{u} \cdot \nabla \mathbf{u} - \mu \Delta \mathbf{u} + \frac{\mu}{\sigma^2} \mathbf{M} \mathbf{u} &= f && \text{in } \Omega \\ \nabla \cdot \mathbf{u} &= 0 && \text{in } \Omega \\ \mathbf{u} &= 0 && \text{on } \partial\Omega. \end{aligned} \quad (3.53)$$

3. *If  $\lim_{\varepsilon \rightarrow 0} \sigma_\varepsilon = 0$ , then  $(\frac{\mathbf{u}_\varepsilon}{\sigma_\varepsilon}, p_\varepsilon)$  converges strongly to  $(\mathbf{u}, p)$  in  $[L^2(\Omega)]^n \times [L^2(\Omega)/\mathbb{R}]$ , where  $(\mathbf{u}, p)$  is the unique solution of the Darcy equations*

$$\begin{aligned} \mathbf{u} &= \frac{\mathbf{M}^{-1}}{\mu} (f - \nabla p) && \text{in } \Omega \\ \nabla \cdot \mathbf{u} &= 0 && \text{in } \Omega \\ \mathbf{u} &= 0 && \text{on } \partial\Omega. \end{aligned} \quad (3.54)$$

The permeability tensor  $\mathbf{M}$  is given by the same Unit Cell Problem as in the linear case [7].

Again, just like in the case when we considered the Stokes equations, three different limit flow regimes appear: In the first case of Theorem 3.17 the obstacles are too small and the limit flow regime is again Navier-Stokes flow. If the size of the obstacles is critical as in the second case, a supplementary term has to be treated in the Navier-Stokes equations and we obtain the nonlinear Brinkman Law. In the third case, the obstacles are comparably large and the nonlinear Navier-Stokes flow degenerates into linear Darcy flow. Still, also our consideration about the practicality of the above model holds. And again, it might be interesting to rehabilitate the nonlinear Brinkman Law, with the permeability  $\mathbf{K}$  instead of  $\mathbf{M}^{-1}$ , in order to model coupled flow in a porous and a free fluid region provided that additionally  $\mu\mathbf{K}^{-1}\mathbf{u}$  dominates over the convective term (cf. Section 3.5).

### 3.6.3. Homogenisation of the Navier-Stokes Equations with Varying Viscosity

We have always assumed the viscosity to be constant, but it can, of course, also be considered dependent on  $\varepsilon$ . In certain cases for problems with small viscosity in a nonlinear framework, Darcy's Law will also be nonlinear. Thus, we consider the following set of time independent dimensionless (cf. eq. 2.3) Navier-Stokes equations

$$\begin{aligned} (\mathbf{u}_\varepsilon \cdot \nabla)\mathbf{u}_\varepsilon + \nabla p_\varepsilon - \frac{1}{\text{Re}_\varepsilon}\Delta\mathbf{u}_\varepsilon &= \frac{1}{\text{Fr}_\varepsilon}\mathbf{f}_\varepsilon & \text{in } \Omega_\varepsilon \\ \nabla \cdot \mathbf{u}_\varepsilon &= 0 & \text{in } \Omega_\varepsilon \\ \mathbf{u}_\varepsilon &= 0 & \text{on } \partial\Omega_\varepsilon, \end{aligned} \tag{3.55}$$

where we now allow the Reynolds number  $\text{Re}$  and the Froude number  $\text{Fr}$  to behave as powers of  $\varepsilon$ , namely

$$\text{Re}_\varepsilon = \frac{1}{\mu} \cdot \varepsilon^{-\gamma_1} \text{ and } \text{Fr}_\varepsilon = \varepsilon^{\gamma_2},$$

where  $\gamma_1 > 0$  and  $\gamma_2 = 1 - \gamma_1$ . According to Mikelić [45] three typical cases for  $\gamma_1$  can be distinguished.

**Case 1**  $\gamma_1 < 1$ : The case  $\gamma_1 < 1$  is the best-understood of all three. The homogenisation of the Navier-Stokes equations always leads to the same linear Darcy Law as described by Theorem 3.16 by only taking into account the leading order terms in the asymptotic expansion. This also confirms the connection of the Navier-Stokes equations and the Stokes system with two pressures, of which the latter has been shown to be equivalent to Darcy's Law. In addition to the well-known fact that for large viscosity the Stokes equations on the microscale approximate the Navier-Stokes equations, we know now that for large  $\mu$  the Navier-Stokes equations give Darcy-type flow in the limit. Moreover, for the case  $\gamma_1 \ll 1$  it seems to be sufficient to study the homogenisation of the Stokes equations.

On the other hand, in the critical case  $\gamma_1 = 1$  a fully nonlinear system of equations is found in the limit. Furthermore, for  $\gamma_1$  close to 1 the approximation offered by Darcy's Law will no longer be sufficiently accurate. The closer  $\gamma$  approaches 1, the less non-

negligible lower order terms become in the asymptotic expansion of equations (3.55), leading to nonlinear extensions of Darcy's Law (cf. [45] and the references therein).

**Case 2**  $\gamma_1 > 1$ : This choice of  $\gamma_1$  leads to ill-defined homogenisation problems, since this is the turbulent case.

**Case 3**  $\gamma_1 = 1$ : The formal asymptotic expansion of equations (3.55) leads to a Navier-Stokes system with two pressures: Find  $\mathbf{u}^0 = \mathbf{u}^0(x, y)$ ,  $p^1 = p^1(x, y)$  and  $p^0 = p^0(x)$  such that

$$\begin{aligned}
 -\mu\Delta_y \mathbf{u}^0 + (\mathbf{u}^0 \cdot \nabla) \mathbf{u}^0 + \nabla_y p^1 + \nabla_x p^0 &= \mathbf{f}(x) && \text{in } \Omega \times Y_F \\
 \operatorname{div}_y \mathbf{u}^0(x, y) &= 0 && \text{in } \Omega \times Y_F \\
 \mathbf{u}^0(x, y) &= 0 && \text{on } \Omega \times \partial Y_F \\
 \{\mathbf{u}^0(x, y), p^1(x, y)\} &&& \text{is periodic in } y \\
 \operatorname{div}_x \int_{Y_F} \mathbf{u}^0(x, y) dy &= 0 && \text{in } \Omega.
 \end{aligned} \tag{3.56}$$

For the formal asymptotic expansion in this case see [53, pp. 142-144] and [52]. The well-posedness of the problem is studied in both [45] and [52], and a numerical solution of the problem can again be found in [52].

### 3.7. Homogenisation Theory in Textiles

In the beginning of this chapter we stated that some aspects of our homogenisation ansatz require that the fluid part  $Y_F$  of the elementary cell  $Y$  is connected, but that the solid part is strictly contained in  $\bar{Y}$ , which is, of course, not fulfilled in a textile repeat cell, where both the fluid and the solid part are of one piece. In this case, the two-scale convergence ansatz leads to the same Darcy's Law, but the proof for the convergence of the homogenisation process has to be modified. In order to account for connected geometries, a modification of Tartar's proof [57] is given by Allaire in [5].

Therefore, all that is left to do is to verify the assumptions that are made on the geometry for textiles and Allaire's conclusions hold.

We denote by  $E_S \subset \mathbb{R}^n$  the closed set that is obtained by  $Y$ -periodic repetition of  $Y_S$  into the entire space  $\mathbb{R}^n$  and we denote by  $E_F$  its fluid counterpart.  $Y_F$  and  $E_F$  have to satisfy the hypotheses

- i.  $Y_F$  and  $Y_S$  have strictly positive measures in  $\bar{Y}$ .
- ii.  $E_F$  and the interior of  $E_S$  are open sets with  $C^1$  boundaries and are locally located on one side of their boundary, and  $E_F$  is connected.
- iii.  $Y_F$  is an open set with a local Lipschitz boundary.

Let us give the concrete meaning of these hypotheses and how they apply to textiles.

**ad i.**  $Y_F$  and  $Y_S$  have strictly positive measures in  $\bar{Y}$ , if the elementary cell  $Y$  contains both fluid and solid together. This is the usual situation in textiles: one textile repeat cell consists of fabric and fluid.

- ad ii.**  $E_F$  has a  $C^1$  boundary, which implies that  $Y_F$  is  $Y$ -periodic. Furthermore,  $\bar{Y}_F$  has an intersection with each face of the cube  $\bar{Y}$  which has a strictly positive surface measure. If this were not the case,  $E_F$  could not be connected when  $E_F$  and  $E_S$  are locally located on one side of their boundary. In textiles, the unit cell is per definition a periodic repeat cell of the medium, where both the fluid and the fabric part are connected.
- ad iii.** That  $Y_F$  is an open set with a local Lipschitz boundary is a more technical assumption: it means, for example, that the intersection of the boundary of  $Y_S$  and  $Y$  may not only consist of a single point, a situation highly unlikely for textile geometries.

Thus, Allaire's assumptions fit well with textile geometries which concludes the validity of Darcy's Law in textile reinforcements.



## 4. Fictitious Domain Approach for Coupled Flow Problems in Plain and Porous Media

In this chapter we discuss a fictitious domain method for the modeling of viscous flow in a single domain which embeds plain, porous and solid media. The whole domain is governed by a single set of the so-called (Navier-)Stokes/Brinkman equations. Within the fictitious domain the particular medium is taken into account by its characteristic permeability, that is a finite value for porous, infinite for pure fluid and zero for pure solid domains. In addition, the viscosity may vary from its specific value in the pure fluid domain, to some effective value in the porous part and up to infinity in the solid domain. This fictitious domain approach avoids the explicit expression of the transmission conditions at the interface of the different media.

### 4.1. Interface Conditions between Plain and Porous Media

Iliev and Laptev [32] give an overview of the most popular coupling conditions between plain and porous media, which we follow here. Coupling conditions can either be formulated at a microlevel or on a macrolevel between the Darcy or Brinkman model in the porous part and the Navier-Stokes equations in the pure fluid part.

**Microscopic Model** This approach starts from first principles, i.e. the Navier-Stokes equations describe the fluid flow in the microgeometry of the pores and the pure fluid domain, completed with no-slip boundary conditions on the solid skeleton of the pores. In this case coupling conditions are unnecessary as one and the same model, namely the Navier-Stokes equations, is valid all over the computational domain. This is the most physically correct approach, but impractical for numerical applications, since it requires an unrealistic amount of CPU time and memory resources. Nevertheless, in Chapter 7 we compute such a model numerically in order to validate the macroscopic Brinkman penalisation model.

**Macroscopic Model with Darcy's Law** According to Iliev and Laptev [32] this is the most common but mathematically the most difficult case, since the Navier-Stokes equations and Darcy's law are PDEs of different order and thus, need a different amount of interface conditions. One possibility is the Beavers-Joseph condition for the tangential velocity, which can be experimentally and mathematically justified. For detailed information see [32] or [45] and the references therein.

**Macroscopic Model with Brinkman's Law** In this case the PDEs describing flow in the porous and pure fluid part are of same order. In literature, two types of coupling conditions between the Navier-Stokes and the Brinkman equations can be found.

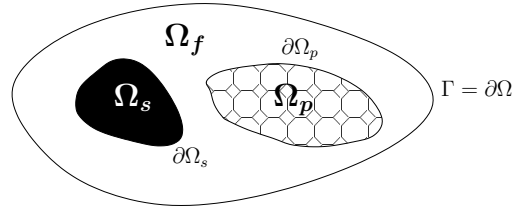


Fig. 4.1.: Embedding in a simple fictitious domain.

Thus, Ochoa-Tapia and Whitaker [51] propose stress jump conditions as opposed to the most common choice of continuous velocity and continuity of the stress tensor's normal component

$$\begin{aligned} u|_{S_p} &= u|_{S_f} \\ \boldsymbol{\nu} \cdot (-p\mathbf{I} + \mu\nabla\mathbf{u})|_{S_p} &= \boldsymbol{\nu} \cdot (-p\mathbf{I} + \mu\nabla\mathbf{u})|_{S_f}, \end{aligned} \quad (4.1)$$

where  $S_p$  and  $S_f$  denote the same interface seen from porous and fluid parts respectively.

The penalised Navier-Stokes/Brinkman system that we propose in this section, can be seen as a reformulation of the third approach, so that a single system of partial differential equations is governing the flow in the pure liquid and the porous domain without explicit implementation of an interface condition such as (4.1).

## 4.2. The Penalisation Approach

Let  $\Omega \subset \mathbb{R}^n$  be a bounded open set that is connected and sufficiently regular. We consider obstacles  $\Omega_p$  and  $\Omega_s$  that can be porous or solid and we decompose  $\Omega$  by

$$\Omega = \Omega_f \cup \Omega_p \cup \Omega_s,$$

where  $\Omega_f$  denotes the pure fluid domain (Fig. 4.1). In the fluid domain  $\Omega_f$  we solve the unsteady incompressible dimensionless Navier-Stokes equations

$$\begin{aligned} \frac{\partial \mathbf{u}}{\partial t} + (\mathbf{u} \cdot \nabla)\mathbf{u} + \nabla p &= \frac{1}{\text{Re}}\Delta\mathbf{u} + \mathbf{f} & \text{in } \Omega_f \times (0, T) \\ \nabla \cdot \mathbf{u} &= 0 & \text{in } \Omega_f \times (0, T), \end{aligned} \quad (4.2)$$

where as usual  $\mathbf{u}(t, x)$  represents the velocity field,  $p(t, x)$  the pressure,  $\text{Re}$  denotes the Reynolds number and  $\mathbf{f}$  stands for external forces. In a next step, we imagine the whole domain  $\Omega$  as a porous medium characterised by its permeability  $\mathbf{K}(x)$ , which can be variable in space. This permeability takes specific values in the respective fluid, solid and porous parts of the domain. Thus, in the porous medium  $\Omega_p$  the permeability is assigned to its specific value  $\mathbf{K}_p$ , whereas the fluid and solid domains are treated as particular porous

media defined by the limits of the Brinkman model. Hence,

$$\mathbf{K}(x) = \begin{cases} \mathbf{K}_f \rightarrow +\infty & \text{if } x \in \Omega_f \\ \mathbf{K}_p & \text{if } x \in \Omega_p \\ \mathbf{K}_s \rightarrow +0 & \text{if } x \in \Omega_s. \end{cases}$$

**Remark:** Note that in the works [12], [13] and [33] that we follow here, the permeability tensor is considered a scalar, as fluid-solid configurations are of main interest there. In the next section, we extend a result to the case that  $\mathbf{K}$  is a diagonal positive definite matrix, which is of most interest for porous media applications. Hence, a statement such as  $\mathbf{K} \rightarrow +\infty$  should be understood in such a way that every entry of the tensor satisfies  $K_{xx} \rightarrow \infty$ ,  $K_{yy} \rightarrow \infty$  and  $K_{zz} \rightarrow \infty$ . Also,  $\mathbf{K}^{-1}\mathbf{u}$  for  $\mathbf{u} = (u, v, w)$  should be thought of as  $(u/K_{xx}, v/K_{yy}, w/K_{zz})^T$ .

Now, we define a single global set of Navier-Stokes/Brinkman equations on the whole domain  $\Omega$

$$\begin{aligned} \frac{\partial \mathbf{u}}{\partial t} + (\mathbf{u} \cdot \nabla) \mathbf{u} - \overbrace{\tilde{\mu} \Delta \mathbf{u} + \nabla p + \mu \mathbf{K}^{-1} \mathbf{u}}^{\text{Classical Brinkman's Law}} = \mathbf{f} \quad \text{in } \Omega \times (0, T) \\ \nabla \cdot \mathbf{u} = 0 \quad \text{in } \Omega \times (0, T), \end{aligned} \quad (4.3)$$

where  $\mu$  denotes the standard viscosity,  $\tilde{\mu}$  the effective ‘Brinkman viscosity’ and the ratio  $\tilde{\mu}/\mu$  depends on the geometry of the porous medium [50]. From these global equations the local equations related to the fluid, porous and solid part can be asymptotically found by the penalty method [33].

- When  $\mathbf{K} = \mathbf{K}_f$ , the term  $\mu \mathbf{K}^{-1} \mathbf{u}$  tends to zero, and we approximately solve the classical Navier-Stokes equations (4.2) in the fluid domain  $\Omega_f$ .
- When  $\mathbf{K} = \mathbf{K}_s$ , the solid is to be considered as a special porous medium with porosity  $\varphi \approx 1$  and hence, with near zero permeability. In this case, the penalisation term  $\mu \mathbf{K}^{-1} \mathbf{u}$  imposes the velocity to tend towards zero in the solid domain, whereby the terms  $\mathbf{u} \cdot \nabla \mathbf{u}$ ,  $\frac{\partial \mathbf{u}}{\partial t}$  and  $\tilde{\mu} \Delta \mathbf{u}$  in (4.3) become negligible. Then, in the solid domain, the classical Darcy’s law is approximately solved.
- When  $\mathbf{K} = \mathbf{K}_p$ , the penalisation term  $\mu \mathbf{K}^{-1} \mathbf{u}$  will again be quite small and we solve a Brinkman type equation in the porous medium. If  $\mu \mathbf{K}^{-1} \mathbf{u}$  is very small compared to the other terms in equation (4.3), we even solve Darcy’s law in the porous part.

A mathematical justification of this penalisation approach is given by Angot in [12] for the linear steady case and by Angot et al. in [13] for the nonlinear unsteady case. Numerical and experimental justification can be found in [33]. In this work, Khadra et al. study steady and unsteady flows around a cylinder and give experimental validation of the computed drag coefficient and reattachment length for various Reynolds numbers. Further, the computed reattachment length for a backward facing step also coincides very well with numerical and experimental results.

In the following, we will focus on the linear steady case applicable to the computation

of textile permeability. As textiles are hierarchically structured materials, our model for fluid flow must take into consideration the possible porosity of the material's yarns. Therefore, we would like to solve a single set of Stokes/Brinkman equations in the textile repeat cell.

### 4.3. Penalisation of the Stokes Equations

In this section we show that we may solve the Brinkman/Stokes equations on the whole domain  $\Omega$  without introduction of explicit transmission conditions for fluid-porous or fluid-solid configurations. The main focus is on the derivation of an error estimate for the fluid-porous case following Angot [12]. We give this estimate in Theorem 4.2 extended to the case that  $\mathbf{K}$  is a positive definite diagonal matrix.

#### 4.3.1. The General Brinkman Model

Let us first introduce the generalised Brinkman model with a result for the existence and uniqueness of its solution. For a fixed viscosity  $\mu > 0$  the Brinkman problem reads

$$\begin{aligned} \tilde{\mu}\Delta\mathbf{u} + \nabla p + \frac{\mu}{\mathbf{K}}\mathbf{u} &= \mathbf{f} & \text{in } \Omega \\ \nabla \cdot \mathbf{u} &= 0 & \text{in } \Omega \\ \mathbf{u} &= 0 & \text{on } \Gamma = \partial\Omega. \end{aligned} \tag{4.4}$$

Furthermore, let us introduce the Hilbert space  $\mathbf{V} = \{\mathbf{v} \in H_0^1(\Omega)^n \text{ such that } \nabla \cdot \mathbf{v} = 0\}$ . Following Angot [12] we cite the following regularity result.

**Lemma 4.1** [EXISTENCE AND UNIQUENESS OF THE BRINKMAN EQUATIONS' SOLUTION] *Let  $f \in H^{-1}(\Omega)^n$  and the permeability  $\mathbf{K} \in L^\infty(\Omega)^{n \times n}$  be a symmetric positive definite second-order tensor. Let the Brinkman viscosity  $\tilde{\mu} \in L^\infty(\Omega)$  and let there exist some  $\mu_0 > 0$  such that  $\tilde{\mu}(x) \geq \mu_0 > 0$  a.e. on  $\Omega$ . Then the generalised Brinkman problem (4.4) admits a unique solution  $(\mathbf{u}, p) \in \mathbf{V} \times L^2(\Omega)/\mathbb{R}$ .*

Later on we will refer to equations (4.4) as to the penalised Brinkman equations (or Brinkman/Stokes equations) which will be specified by the choice of  $\mathbf{K}$ ,  $\mu$  and  $\tilde{\mu}$  according to the decomposition of the domain  $\Omega$  (cf. Table 4.1). In the next subsection we derive an error estimate for the solution of the penalty Brinkman equations compared to the Stokes and Brinkman equations with appropriate transmission conditions in case that a porous domain is embedded in a pure fluid domain (Figure 4.2).

#### 4.3.2. The Fluid-Porous Model

We assume that  $\Omega$  is composed of two subdomains  $\Omega_f$  and  $\Omega_p$  separated by a regular hypersurface  $\Lambda$  such that

$$\Omega = \Omega_f \cup \Lambda \cup \Omega_p.$$

Let  $\Gamma_f$  denote the boundary of  $\Omega_f$  and  $\Gamma_p$  the boundary of  $\Omega_p$ , and let  $\boldsymbol{\nu}$  denote the normal unit vector on  $\Lambda$  oriented from fluid to porous domain. Furthermore,  $(\mathbf{u}, p) \in \mathbf{V} \times L^2(\Omega)/\mathbb{R}$

Configuration	$\mathbf{K}_f$	$\mathbf{K}_p$	$\mathbf{K}_s$	$\tilde{\mu}_f$	$\tilde{\mu}_p$	$\tilde{\mu}_s$	$\tilde{\mu}$
Fluid-Porous	$\frac{1}{\varepsilon}$	$\mathbf{K}$	–	$\mu$	$\tilde{\mu}$	–	–
Fluid-Solid $L^2$	$\frac{1}{\varepsilon}$	–	$\varepsilon$	–	–	–	$\mu > 0$
Fluid-Solid $H^1$	$\frac{1}{\varepsilon}$	–	$\varepsilon$	$\mu > 0$	–	$\frac{\mu}{\varepsilon}$	–

Table 4.1.: Definition of permeability and viscosity in the Brinkman problem (4.4) for the two different domain decompositions Fluid-Porous and Fluid-Solid including the so-called  $H^1$ - as well as the so-called  $L^2$ -penalisation.

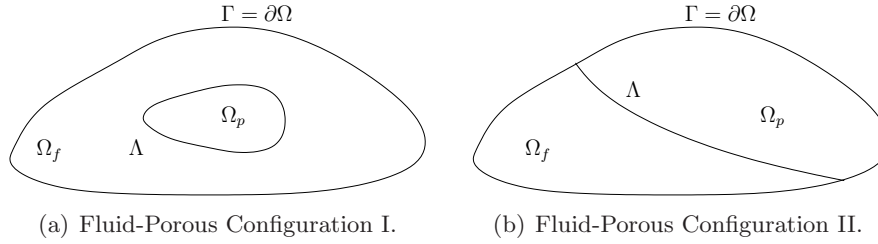


Fig. 4.2.: Two possible domain decompositions.

denotes the solution of the fluid-porous transmission problem whose restriction  $(\mathbf{u}_f, p_f)$  over  $\Omega_f$  satisfies the Stokes problem and whose restriction  $(\mathbf{u}_p, p_p)$  over  $\Omega_p$  satisfies the Brinkman one

$$\begin{array}{ll}
 \text{Brinkman problem} & \text{Stokes problem} \\
 -\tilde{\mu}\Delta\mathbf{u}_p + \nabla p_p + \mathbf{K}^{-1}\mathbf{u}_p = f_p & \text{in } \Omega_p & -\mu\Delta\mathbf{u}_f + \nabla p_f = f_f & \text{in } \Omega_f \\
 \nabla \cdot \mathbf{u}_p = 0 & \text{in } \Omega_p & \nabla \cdot \mathbf{u}_f = 0 & \text{in } \Omega_f \\
 \mathbf{u}_p = 0 & \text{on } \Gamma = \partial\Omega & \mathbf{u}_f = 0 & \text{on } \Gamma = \partial\Omega,
 \end{array} \tag{4.5}$$

with continuity of the velocity and continuity of the normal component of the stress tensor

$$\mathbf{u}_f|_\Lambda = \mathbf{u}_p|_\Lambda \text{ and } \boldsymbol{\nu} \cdot (-p_f\mathbf{I} + \mu\nabla\mathbf{u}_f)|_\Lambda = \boldsymbol{\nu} \cdot (-p_s\mathbf{I} + \mu\nabla\mathbf{u}_s)|_\Lambda \tag{4.6}$$

as transmission conditions on the interface  $\Lambda$ .

**Remark:** In order to derive error estimates we only allow domain decomposition configurations of type Figure 4.2(a). In this case,  $\Omega_f$  and  $\Omega_p$  are of class  $C^2$  and the following regularity result for the solution of the Stokes equations holds (cf. [12] and the references therein): we obtain  $(\mathbf{u}, p) \in H_0^1(\Omega)^n \times L^2(\Omega) \setminus \mathbb{R}$  such that  $(\mathbf{u}_f, p_f) \in H^2(\Omega_f)^n \times H^1(\Omega_f)$  and  $(\mathbf{u}_p, p_p) \in H^2(\Omega_p)^n \times H^1(\Omega_p)$ . Hence the normal component of the stress tensor is in  $H^{1/2}(\Lambda)^n$ .

**Theorem 4.2** [ERROR ESTIMATE FOR THE STOKES/BRINKMAN EQUATIONS]

Let  $\varepsilon > 0$  be a given parameter and let  $(\mathbf{u}_\varepsilon, p_\varepsilon) \in \mathbf{V} \times L^2(\Omega)/\mathbb{R}$  denote the solution of the penalty Brinkman problem (4.4) over the whole fictitious domain  $\Omega$  with a positive definite diagonal second-order tensor  $\mathbf{K}$ . We characterise permeabilities  $\mathbf{K}_f$  and  $\mathbf{K}_p$  by

$$\mathbf{K}_f = \mathbf{K}|_{\Omega_f} = \frac{1}{\varepsilon} \mathbf{I}, \quad \mathbf{K}_p = \mathbf{K}|_{\Omega_p} = \mathbf{K}$$

and define viscosity values  $\mu_f$  and  $\tilde{\mu}_p$  by

$$\tilde{\mu}_f = \mu = \bar{\mu}|_{\Omega_f}, \quad \tilde{\mu}_p = \tilde{\mu} = \bar{\mu}|_{\Omega_p}.$$

Furthermore, let  $\mathbf{u}$  be the solution of the fluid-porous transmission problem (4.5-4.6). Then, if  $f \in L^2(\Omega)^n$  and if  $\Omega_f$  and  $\Omega_p$  are of class  $C^2$ , the error estimate

$$\|\mathbf{u}_\varepsilon - \mathbf{u}\|_{H^1(\Omega)} = \mathcal{O}(\varepsilon)$$

holds for the penalty solution  $\{\mathbf{u}_\varepsilon\}_{\varepsilon>0}$ .

*Proof.* The weak formulation of the Stokes/Brinkman problem reads

$$\mu \int_{\Omega_f} \nabla \mathbf{u}_\varepsilon \cdot \nabla \boldsymbol{\varphi} \, dx + \tilde{\mu} \int_{\Omega_p} \nabla \mathbf{u}_\varepsilon \cdot \nabla \boldsymbol{\varphi} \, dx + \mu \varepsilon \int_{\Omega_f} \mathbf{u}_\varepsilon \cdot \boldsymbol{\varphi} \, dx + \mu \int_{\Omega_p} \mathbf{K}^{-1} \mathbf{u}_\varepsilon \cdot \boldsymbol{\varphi} \, dx = \int_{\Omega} \mathbf{f} \cdot \boldsymbol{\varphi} \, dx$$

for all  $\boldsymbol{\varphi} \in \mathbf{V}$ . Note that the pressure integral cancels out because  $\boldsymbol{\varphi}$  is divergence-free in  $\Omega$ . We denote the diagonal entries of  $\mathbf{K}$  by  $(\kappa_i)_{i=1,\dots,n}$ , choose  $\boldsymbol{\varphi} = \mathbf{u}_\varepsilon$  and divide by  $\mu > 0$

$$\int_{\Omega_f} |\nabla \mathbf{u}_\varepsilon|^2 \, dx + \frac{\tilde{\mu}}{\mu} \int_{\Omega_p} |\nabla \mathbf{u}_\varepsilon|^2 \, dx + \varepsilon \int_{\Omega_f} |\mathbf{u}_\varepsilon|^2 \, dx + \int_{\Omega_p} \sum_{i=1}^n \kappa_i^{-1} u_{\varepsilon_i}^2 \, dx = \int_{\Omega} \mathbf{f} \cdot \mathbf{u}_\varepsilon \, dx. \quad (4.7)$$

Since, we aim at an upper estimate for the left hand side of this equation, we are allowed to leave out the last two positive terms there. Note, that  $\mathbf{K}$  has only positive diagonal entries. On the right hand side we employ the Cauchy-Schwarz and Poincaré's inequality. An overview on the inequalities used in this proof is given in Appendix A.3.

$$\begin{aligned} \int_{\Omega_f} |\nabla \mathbf{u}_\varepsilon|^2 \, dx + \frac{\tilde{\mu}}{\mu} \int_{\Omega_p} |\nabla \mathbf{u}_\varepsilon|^2 \, dx &\leq C \cdot \frac{1}{\mu} \|f\|_{L^2(\Omega)} \|\mathbf{u}_\varepsilon\|_{L^2(\Omega)} \\ &\leq C \cdot \frac{1}{\mu} \|f\|_{L^2(\Omega)} \tilde{C} \cdot \|\nabla \mathbf{u}_\varepsilon\|_{L^2(\Omega)} \\ &= \max(C, \tilde{C})^2 \cdot \frac{1}{\mu} \|f\|_{L^2(\Omega)} \left( \|\nabla \mathbf{u}_\varepsilon\|_{L^2(\Omega_f)} + \|\nabla \mathbf{u}_\varepsilon\|_{L^2(\Omega_p)} \right). \end{aligned}$$

Hence, we have

$$\|\nabla \mathbf{u}_\varepsilon\|_{L^2(\Omega_f)}^2 + \frac{\tilde{\mu}}{\mu} \|\nabla \mathbf{u}_\varepsilon\|_{L^2(\Omega_p)}^2 \leq C \cdot \frac{1}{\mu} \|f\|_{L^2(\Omega)} \left( \|\nabla \mathbf{u}_\varepsilon\|_{L^2(\Omega_f)} + \|\nabla \mathbf{u}_\varepsilon\|_{L^2(\Omega_p)} \right). \quad (4.8)$$

In the next step we apply Young's inequality term by term on the right hand side of (4.8)

$$C \cdot \frac{1}{\mu} \|f\|_{L^2(\Omega)} \|\nabla \mathbf{u}_\varepsilon\|_{L^2(\Omega_f)} \leq \frac{1}{2} \left[ \frac{C^2}{\mu^2} \|f\|_{L^2(\Omega)}^2 + \|\nabla \mathbf{u}_\varepsilon\|_{L^2(\Omega_f)}^2 \right]$$

and "Young's inequality with  $\varepsilon$ "

$$C \cdot \frac{1}{\mu} \|f\|_{L^2(\Omega)} \|\nabla \mathbf{u}_\varepsilon\|_{L^2(\Omega_p)} \leq \frac{1}{\mu} \left[ \frac{C^2}{2\tilde{\mu}} \|f\|_{L^2(\Omega)}^2 + \frac{\tilde{\mu}}{2} \|\nabla \mathbf{u}_\varepsilon\|_{L^2(\Omega_p)}^2 \right].$$

Insertion of these results into equation (4.8) and subtraction of the gradient terms yields

$$\begin{aligned} \frac{1}{2} \|\nabla \mathbf{u}_\varepsilon\|_{L^2(\Omega_f)}^2 + \frac{\tilde{\mu}}{2\mu} \|\nabla \mathbf{u}_\varepsilon\|_{L^2(\Omega_p)}^2 &\leq \frac{C^2}{2\mu^2} \|f\|_{L^2(\Omega)}^2 + \frac{C^2}{2\tilde{\mu}\mu} \|f\|_{L^2(\Omega)}^2 \\ &\leq \frac{C^2}{2\mu} \|f\|_{L^2(\Omega)}^2 \left[ \frac{1}{\mu} + \frac{1}{\tilde{\mu}} \right], \end{aligned}$$

which means

$$\mu \|\nabla \mathbf{u}_\varepsilon\|_{L^2(\Omega_f)}^2 + \tilde{\mu} \|\nabla \mathbf{u}_\varepsilon\|_{L^2(\Omega_p)}^2 \leq C^2 \|f\|_{L^2(\Omega)}^2 \left[ \frac{1}{\mu} + \frac{1}{\tilde{\mu}} \right].$$

Of course, we can now bound every term on the right hand side by the term on the left hand side independently and extract the square root. Renewed addition of both terms yields the result that  $u_\varepsilon$  is uniformly bounded in  $H_0^1(\Omega)^n$  independent of  $\varepsilon$

$$\|\nabla \mathbf{u}_\varepsilon\|_{L^2(\Omega)} \leq C \|f\|_{L^2(\Omega)} \sqrt{\frac{1}{\mu} + \frac{1}{\tilde{\mu}}},$$

or again by Poincaré's inequality

$$\|\mathbf{u}_\varepsilon\|_{H^1(\Omega)} \leq \tilde{C} \|f\|_{L^2(\Omega)} \sqrt{\frac{1}{\mu} + \frac{1}{\tilde{\mu}}}. \quad (4.9)$$

Moreover, let  $\mathbf{u} \in \mathbf{V}$  denote the solution of the coupled problem (4.5-4.6). In variational formulation over the whole domain  $\Omega$  for all  $\boldsymbol{\varphi} \in \mathbf{V}$  this reads

$$-\bar{\mu} \int_{\Omega} \Delta \mathbf{u} \cdot \boldsymbol{\varphi} \, dx + \int_{\Omega} \nabla p \cdot \boldsymbol{\varphi} \, dx + \bar{\mu} \int_{\Omega} \mathbf{K}^{-1} \mathbf{u} \cdot \boldsymbol{\varphi} \, dx = \int_{\Omega} \mathbf{f} \cdot \boldsymbol{\varphi} \, dx.$$

If we take into account the regularity of the solution  $(\mathbf{u}, p) \in H_0^1(\Omega)^n \times L^2(\Omega) \setminus \mathbb{R}$  and integrate by parts, the boundary integrals cancel out and we obtain

$$-\bar{\mu} \int_{\Omega} \nabla \mathbf{u} \cdot \nabla \boldsymbol{\varphi} \, dx + \bar{\mu} \int_{\Omega} \mathbf{K}^{-1} \mathbf{u} \cdot \boldsymbol{\varphi} \, dx = \int_{\Omega} \mathbf{f} \cdot \boldsymbol{\varphi} \, dx \quad (4.10)$$

$$\Leftrightarrow \mu \int_{\Omega_f} \nabla \mathbf{u} \cdot \nabla \varphi \, dx + \tilde{\mu} \int_{\Omega_p} \nabla \mathbf{u} \cdot \nabla \varphi \, dx + \mu \int_{\Omega_p} \mathbf{K}^{-1} \mathbf{u} \cdot \varphi \, dx = \int_{\Omega_f} \mathbf{f} \cdot \varphi \, dx + \int_{\Omega_p} \mathbf{f} \cdot \varphi \, dx. \quad (4.11)$$

The error estimate for  $\mathbf{u}_\varepsilon - \mathbf{u}$  is then given by the difference of both variational formulations (4.7) and (4.11)

$$\begin{aligned} \mu \int_{\Omega_f} \nabla (\mathbf{u}_\varepsilon - \mathbf{u}) \cdot \nabla \varphi \, dx + \tilde{\mu} \int_{\Omega_p} \nabla (\mathbf{u}_\varepsilon - \mathbf{u}) \cdot \nabla \varphi \, dx + \\ \mu \varepsilon \int_{\Omega_f} \mathbf{u}_\varepsilon \cdot \varphi \, dx + \mu \int_{\Omega_f} \mathbf{K}^{-1} (\mathbf{u}_\varepsilon - \mathbf{u}) \cdot \varphi \, dx = 0. \end{aligned}$$

Again, by taking  $\varphi = \mathbf{u}_\varepsilon - \mathbf{u}$  and dividing by  $\mu > 0$  the equation reads

$$\begin{aligned} \int_{\Omega_f} |\nabla (\mathbf{u}_\varepsilon - \mathbf{u})|^2 \, dx + \frac{\tilde{\mu}}{\mu} \int_{\Omega_p} |\nabla (\mathbf{u}_\varepsilon - \mathbf{u})|^2 \, dx + \\ \int_{\Omega_f} \sum_{i=1}^n \kappa_i^{-1} (u_\varepsilon - u)_i^2 \, dx = -\varepsilon \int_{\Omega_f} \mathbf{u}_\varepsilon \cdot (\mathbf{u}_\varepsilon - \mathbf{u}) \, dx, \end{aligned}$$

and has the same form as equation (4.7). Hence, by employing the same inequalities we obtain

$$\|\nabla (\mathbf{u}_\varepsilon - \mathbf{u})\|_{L^2(\Omega)} \leq \varepsilon C \|\mathbf{u}_\varepsilon\|_{L^2(\Omega_f)},$$

and finally by combination with (4.9) we obtain the existence of a constant  $C_0 = C_0(\Omega, \mu, \tilde{\mu}, \mathbf{f})$  such that

$$\|\nabla (\mathbf{u}_\varepsilon - \mathbf{u})\|_{H^1(\Omega)} \leq C_0 \cdot \varepsilon.$$

□

### 4.3.3. An Excursus on the Fluid-Solid Model

We assume that  $\Omega$  is composed of two subdomains  $\Omega_f$  and  $\Omega_s$  denoting the fluid and the solid part separated by a regular hypersurface  $\Lambda$  such that  $\Omega = \Omega_f \cup \Lambda \cup \Omega_s$ . Let  $\Gamma_f$  be the boundary of  $\Omega_f$  and  $\Gamma_s$  the boundary of  $\Omega_s$ . Let  $(\mathbf{u}, p) \in \mathbf{V} \times L^2(\Omega)/\mathbb{R}$  denote the solution of the Stokes problem

$$\begin{aligned} -\mu \Delta \mathbf{u}_f + \nabla p_f &= \mathbf{f}_f & \text{in } \Omega_f \\ \nabla \cdot \mathbf{u}_f &= 0 & \text{in } \Omega_f \\ \mathbf{u}_f &= 0 & \text{on } \Gamma_f, \end{aligned} \quad (4.12)$$

extended by  $(\mathbf{u}_s, p_s) = 0$  inside  $\Omega_s$ .

In [12] Angot presents error estimates for the solution  $\mathbf{u}_\varepsilon$  of the penalised Brinkman problem (4.4) as opposed to the above solution  $\mathbf{u}$  of the Stokes problem. He introduces two different penalisation methods of the Brinkman problem, namely an  $L^2$ - as well as an  $H^1$ -penalisation. Both configurations are given in Table 4.1. If we carry out an  $L^2$ -penalisation, we penalise the velocity by a small parameter  $\varepsilon > 0$  in  $\Omega_s$ . When  $\varepsilon$  goes to zero, the penalised solution  $\mathbf{u}_\varepsilon$  of (4.4) asymptotically satisfies the Darcy equation in the solid domain.

In addition, for the  $H^1$ -penalisation, we also penalise the velocity gradient inside the solid domain. Then, not only the permeability is tending to zero, but also the viscosity is tending to infinity in the solid body, and the according error estimate can be improved up to optimality. In this case, the penalised solution satisfies the Brinkman equations in the solid part. These results are generalised to the non-linear case of the Navier-Stokes/Brinkman equations in [13].

In [13], Angot et al. also differentiate between an  $L^2$ -penalisation and an  $H^1$ -penalisation. In the first case, a damping term on the velocity in the momentum equation is added as described above, and in the latter both the time derivative and the viscous term are perturbed, inducing a Darcy equation or a Brinkman equation in the solid body respectively.



## 5. The Numerical Model

In this chapter we discuss implementational issues of the Navier-Stokes and of the porous media flow equations. After a short presentation of the Navier-Stokes solver NaSt3DGP developed by the research group of Prof. Michael Griebel at the Institute for Numerical Simulation at the University of Bonn [28],[3], we describe the extensions to the code that are necessary for fast permeability computations. One important modification is the semi-implicit solution of the Navier-Stokes equations, which fastens the speed of simulations in the low Reynolds number regime considerably. Therefore, in a last part of this chapter we discuss the numerical validity of the semi-implicit pressure correction method.

### 5.1. Discretisation of the Navier-Stokes Equations

First of all, recall the formulation of the non-dimensional Navier-Stokes equations

$$\frac{\partial \mathbf{u}}{\partial t} + \nabla p = -(\mathbf{u} \cdot \nabla) \mathbf{u} + \frac{1}{\text{Re}} \Delta \mathbf{u} + \mathbf{f} \quad \text{in } \Omega \times (0, T) \quad (5.1)$$

$$\nabla \cdot \mathbf{u} = 0 \quad \text{in } \Omega \times (0, T) \quad (5.2)$$

with boundary conditions

$$\mathbf{u}|_{\Gamma} = \mathbf{u}_b. \quad (5.3)$$

Let us reintroduce  $\Omega \subset \mathbb{R}^3$  as a fixed domain filled with fluid,  $\mathbf{f}$  as volume forces, the velocity field  $\mathbf{u} = (u, v, w)^T : \Omega \rightarrow \mathbb{R}^3$  and the pressure  $p : \Omega \times [0, T] \rightarrow \mathbb{R}$ .

The most common numerical approach for the solution of (5.1-5.3) are the so-called fractional-step methods. First, the momentum equations (5.1) are advanced to give an approximation of the velocity  $\mathbf{u}$  or some provisional velocity field  $\mathbf{u}^*$ . Then, an elliptic equation is solved that enforces the divergence constraint (5.2) and determines the pressure. NaSt3DGP employs a projection method pioneered by Chorin [20], which is based on the observation that the left hand side of the momentum equations (5.1) is a Hodge decomposition, for which an equivalent projection formulation is given by

$$\frac{\partial \mathbf{u}}{\partial t} = \mathbf{P} \left( -(\mathbf{u} \cdot \nabla) \mathbf{u} + \frac{1}{\text{Re}} \Delta \mathbf{u} + \mathbf{f} \right),$$

where  $\mathbf{P}$  denotes the operator which projects a vector field onto the space of divergence-free vector fields [19].

### 5.1.1. Discretisation in Time

Omitting for the moment external forces  $\mathbf{f}$ , we write the Navier-Stokes equations (5.1-5.3) in time-discrete notation as

$$\begin{aligned} \frac{\mathbf{u}^{n+1} - \mathbf{u}^n}{\Delta t} + \nabla p^n &= -[\mathbf{u} \cdot \nabla \mathbf{u}]^n + \frac{1}{\text{Re}} \Delta \mathbf{u}^n & \text{in } \Omega \\ \nabla \cdot \mathbf{u}^{n+1} &= 0 & \text{in } \Omega \\ \mathbf{u}|_{\Gamma}^{n+1} &= \mathbf{u}_b^{n+1}. \end{aligned}$$

Then the Chorin projection method is given by two successive steps.

**Step 1:** Solve the momentum equations for an intermediate velocity field  $\mathbf{u}^*$

$$\frac{\mathbf{u}^* - \mathbf{u}^n}{\Delta t} + [\mathbf{u} \cdot \nabla \mathbf{u}]^n = \frac{1}{\text{Re}} \Delta \mathbf{u}^n \quad (5.4)$$

with boundary conditions

$$\mathbf{u}^*|_{\Gamma} = \mathbf{u}_b^{n+1}. \quad (5.5)$$

**Step 2:** Project the vector field  $\mathbf{u}^*$  on a divergence-free vector field  $\mathbf{u}^{n+1}$

$$\mathbf{u}^* = \mathbf{u}^{n+1} + \Delta t \nabla p \quad (5.6)$$

$$\nabla \cdot \mathbf{u}^{n+1} = 0. \quad (5.7)$$

Application of the divergence operator to (5.6) results in a Poisson equation for the pressure from which we can obtain the pressure implicitly

$$\frac{1}{\Delta t} \nabla \cdot \mathbf{u}^* = \Delta p. \quad (5.8)$$

Then, we compute the velocity field  $\mathbf{u}^{n+1}$  of the next time-step by equation (5.6). For the solution of the Poisson equation, boundary conditions for the pressure are required. By the projection of equation (5.6) onto the outer unit normal of the domain's boundary

$$\left. \frac{\partial p^{n+1}}{\partial \boldsymbol{\nu}} \right|_{\Gamma} = \frac{\mathbf{u}_{\Gamma}^* - \mathbf{u}_{\Gamma}^{n+1}}{\Delta t} \cdot \boldsymbol{\nu},$$

homogeneous Neumann boundary conditions for the pressure are induced, if we set for the intermediate velocity field  $\mathbf{u}^*|_{\Gamma} = \mathbf{u}^{n+1}|_{\Gamma}$  as implied in equation (5.5). Furthermore, we fix the constant up to which the pressure is uniquely defined by imposing

$$\int_{\Omega} p^{n+1} = 0.$$

For the discretisation of time the NaSt3DGP code provides explicit Euler as well as second order Adams-Bashforth or Runge-Kutta schemes. We solve the pressure Poisson equation (5.8) iteratively by methods like SOR, Red-Black Gauss-Seidel or BiCGStab [64], [21].

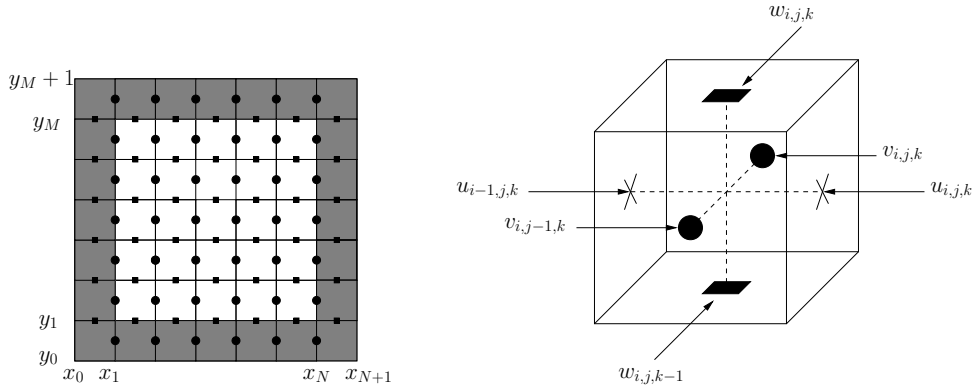


Fig. 5.1.: Example of a 2D staggered grid and a 3D staggered grid cell

### 5.1.2. Discretisation in Space

The Navier-Stokes equations are resolved on a regular staggered grid (Fig. 5.1) by a finite volume discretisation. On the staggered grid the pressure  $p_{i,j,k}$  is discretised at the centre of the cells, while the velocities  $u_{i+\frac{1}{2},j,k}$ ,  $v_{i,j+\frac{1}{2},k}$ ,  $w_{i,j,k+\frac{1}{2}}$  are discretised at the centre of the cell surfaces. This discretisation leads to a strong coupling between pressure and velocities, and therefore avoids the occurrence of unphysical oscillations in the pressure.

Here and in the following, we denote by cells the rectangular subdomains  $[x_i, x_{i+1}] \times [y_j, y_{j+1}] \times [z_k, z_{k+1}]$ , and we define the discrete computational domain  $\Omega_h$  as a union of such cells. For  $\{i, j, k\} \in \mathbb{Z}$  we use the notation

$$\Delta x_i = x_i - x_{i-1} \text{ and } \Delta x_{i+1/2} = x_i + x_{i+1/2},$$

where  $\Delta y_j$ ,  $\Delta y_{j+1/2}$ ,  $\Delta z_k$  and  $\Delta z_{k+1/2}$  are defined analogously. Thus, the velocity and pressure values are defined on the following nodes.

$[u_{i,j,k}]$  is defined on  $[x_i, y_{j+1/2}, z_{k+1/2}]$  at the right/left side surface centre.

$[v_{i,j,k}]$  is defined on  $[x_{i+1/2}, y_j, z_{k+1/2}]$  at the back/front side surface centre.

$[w_{i,j,k}]$  is defined on  $[x_{i+1/2}, y_{j+1/2}, z_k]$  at the upper/lower side surface centre.

$[p_{i,j,k}]$  is defined on  $[x_{i+1/2}, y_{j+1/2}, z_{k+1/2}]$  at the box centre.

NaSt3DGP provides several second order Total Variation Diminishing upwind schemes for the spatial discretisation of the convective terms, including Donor-Cell (1st/2nd order), QUICK (2nd-order), HLLP (2nd-order), SMART (2nd-order) and VONOS (2nd/3rd-order)

[21]. The diffusive terms in equation (5.4) can be discretised directly by

$$\begin{aligned} [u_{xx}]_{i,j,k} &= \frac{1}{\Delta x_{i+1/2}} \left[ \frac{u_{i+1,j,k} - u_{i,j,k}}{\Delta x_i} - \frac{u_{i,j,k} - u_{i-1,j,k}}{\Delta x_{i-1}} \right] \\ [u_{yy}]_{i,j,k} &= \frac{1}{\Delta y_j} \left[ \frac{u_{i,j+1,k} - u_{i,j,k}}{\Delta y_{j+1/2}} - \frac{u_{i,j,k} - u_{i,j-1,k}}{\Delta y_{j-1/2}} \right] \\ [u_{zz}]_{i,j,k} &= \frac{1}{\Delta z_k} \left[ \frac{u_{i,j,k+1} - u_{i,j,k}}{\Delta z_{k+1/2}} - \frac{u_{i,j,k} - u_{i,j,k-1}}{\Delta z_{k-1/2}} \right]. \end{aligned} \quad (5.9)$$

The velocities  $v$  and  $w$  are discretised in a similar way. As opposed to the discretisation of the convective terms [21], a special treatment of the boundary is unnecessary, since the discretisation stencil needs three grid cells only. Further, the convergence error remains at second order as long as we choose an equidistant grid.

### 5.1.3. Time-Step Control

Explicit treatment of the time-advancement of the momentum equations (5.4) yields a time-step restriction for the convective terms, as well as for the diffusive terms and for volume forces. This restriction guarantees the numerical stability of the method and is obtained by a stability analysis of the linearised Navier-Stokes equations [65].

The time-step restriction for the convective terms, generally known as Courant-Friedrich-Levy (CFL) condition, ensures that convection can take effect only on one further grid cell per time-step

$$\Delta t_c \leq \min_{\Omega} \left\{ \frac{\partial x}{|u|_{\max}}, \frac{\partial y}{|v|_{\max}}, \frac{\partial z}{|w|_{\max}} \right\}, \quad (5.10)$$

where  $|\cdot|_{\max}$  denotes the discrete absolute maximum of the respective velocity components. In the same manner, we restrict the diffusion to act no further than one grid cell per time-step

$$\Delta t_d \leq \left[ \frac{1}{Re} \left( \frac{2}{(\partial x)^2} + \frac{2}{(\partial y)^2} + \frac{2}{(\partial z)^2} \right) \right]^{-1}. \quad (5.11)$$

Volume forces can be included in the stability constraint for the diffusive terms [21]. Then the CFL condition for one velocity component  $u$  reads

$$\Delta t_{g_x}^u \leq \left[ \frac{|u|_{\max}}{\partial x} + \sqrt{\left( \frac{|u|_{\max}}{\partial x} \right)^2 + \frac{4|g_x|}{\partial x}} \right]^{-1}. \quad (5.12)$$

In permeability computations for textiles we usually deal with Reynolds numbers of  $Re \approx 1$  or smaller. In this low Reynolds number regime the CFL condition for the convective terms (5.12) usually allows for a much larger time-step than (5.11), since the time step restriction for the diffusive terms depends strongly on the magnitude of the viscosity. Therefore, we find it desirable to treat the diffusive terms implicitly.

## 5.2. Semi-Implicit Solution of the Navier-Stokes Equations

We opt for a second-order semi-implicit discretisation of the Navier-Stokes equations (5.1-5.3) which in time-discrete notation is given by

$$\frac{\mathbf{u}^{n+1} - \mathbf{u}^n}{\Delta t} + \underbrace{\left[ \frac{3}{2} \mathbf{u}^n \cdot \nabla \mathbf{u}^n - \frac{1}{2} \mathbf{u}^{n-1} \cdot \nabla \mathbf{u}^{n-1} \right]}_{\mathcal{H}^n(\mathbf{u})} + \nabla p^{n+\frac{1}{2}} = \frac{1}{2\text{Re}} \Delta (\mathbf{u}^{n+1} + \mathbf{u}^n) \quad \text{in } \Omega$$

$$\nabla \cdot \mathbf{u}^{n+1} = 0 \quad \text{in } \Omega$$

$$\mathbf{u}|_{\Gamma}^{n+1} = \mathbf{u}_b^{n+1}.$$

In this representation the convective derivative is computed by a second-order Adams-Bashforth approximation  $\mathcal{H}(\mathbf{u})$  and the diffusive terms are discretised with the Crank-Nicolson scheme and are treated implicitly. With this implementation we avoid the restriction of the time step (5.11) as well as the solution of a nonlinear system of equations (by the explicit treatment of the convective terms). Again, we employ a fractional step method to solve the Navier-Stokes equations. In order for  $\mathbf{u}^*$  to be a good approximation of the divergence-free velocity field  $\mathbf{u}^{n+1}$ , the pressure gradient is included in the momentum equations resulting in the following pressure-correction scheme as proposed by Bell et al. [15].

**Step 1:** Solve the momentum equations for the intermediate velocity field  $\mathbf{u}^*$

$$\left( I - \frac{\Delta t}{2\text{Re}} \Delta \right) \mathbf{u}^* = \mathbf{u}^n - \Delta t \cdot \left( \mathcal{H}^n(\mathbf{u}) + \nabla p^{n-\frac{1}{2}} - \frac{\Delta t}{2\text{Re}} \Delta \mathbf{u}^n \right) \quad (5.13)$$

with boundary conditions  $\mathbf{u}^*|_{\Gamma} = \mathbf{u}_b^{n+1}$ .

**Step 2:** Recover  $\mathbf{u}^{n+1}$  from the projection of  $\mathbf{u}^*$  by solving

$$\begin{aligned} \mathbf{u}^* &= \mathbf{u}^{n+1} + \Delta t \nabla \phi^{n+1} \\ \nabla \cdot \mathbf{u}^{n+1} &= 0. \end{aligned} \quad (5.14)$$

**Step 3:** The new pressure is now found by computing

$$p^{n+\frac{1}{2}} = p^{n-\frac{1}{2}} + \phi^{n+1} - \frac{\Delta t}{2\text{Re}} \Delta \phi^{n+1} \quad (5.15)$$

We can find the form (5.15) of the pressure update by a backward substitution of equation (5.14) into equation (5.13). This is introduced by Brown et al. in [19]. The authors find the accuracy for both the velocity and the pressure to be  $\mathcal{O}(\Delta t^2)$  in some test examples.

Altogether, this kind of implicit treatment of the Navier-Stokes equations yields three modified Helmholtz equations (5.13) for the velocities in addition to the Poisson equation for the pressure. For the solution of these equations we employ an SSOR Preconditioned Conjugate Gradient Method. The step size is now only limited by the CFL condition and by accuracy considerations. Compared to the explicit solver, the extra computational costs

per iteration for the semi-implicit solver do not outrun the gain due to the larger time steps: computations of the permeability can be obtained much faster with this method as will be shown later on in this thesis.

For our purposes it is very important that the pressure is included in equation (5.13) from the beginning. For the computation of Stokes flow in a textile repeat cell, we set periodic boundaries for the velocities and periodic boundary conditions up to a constant gradient for the pressure. Thus, flow is driven by this fixed pressure gradient, and if it is not included in the Helmholtz type equation (5.13), we actually solve a different problem. All in all the associated algorithm to the semi-implicit implementation reads:

---

**Algorithm 5.2.1:** BASIC SEMI-IMPLICIT ALGORITHM( $\mathbf{u}, p$ )

---

```

{ Set boundary conditions for the  $\Delta$  part of Helmholtz matrix.
  Set  $t=0$ .
  Assign initial values to  $\mathbf{u}, p$ .
main
while  $t \leq t_{\text{end}}$ 
  { Select  $\Delta t$ .
    Set boundary conditions for  $\mathbf{u}, p$ .
    Compute  $F^{(n)}, G^{(n)}, H^{(n)}$  as the RHS of eq. (5.13).
    Set necessary runtime boundary conditions for  $\mathbf{u}^*$ .
  do { Solve the Helmholtz system for  $\mathbf{u}^*$  according to eq. (5.13).
      Compute RHS of pressure Poisson equation (5.14).
      Solve pressure Poisson equation (5.14) for pressure difference  $\phi^{(n+1)}$ .
      Compute  $\mathbf{u}^{(n+1)}$  according to eqs. (5.14).
      Compute  $p^{(n+1/2)}$  according to eq. (5.15).
       $t = t + \Delta t$ .
  }

```

---

**Remark:** Let us mention that the implementation of a Stokes solver is, of course, a simple reduction of a given Navier-Stokes solver. Thus, we use the same temporal and spatial discretisation, and can also solve the Stokes equations implicitly via equation (5.13) and the pressure correction method.

### 5.2.1. Implementation of the Intermediate Velocity Field's Boundary Conditions

The discretisation of the boundary conditions for the intermediate velocity field

$$\mathbf{u}^*|_{\Gamma} = \mathbf{u}_b^{n+1} \quad (5.16)$$

has to be included by appropriate manipulations in the matrix  $(I - (\Delta t/2\text{Re})\Delta)$  of the Helmholtz equation (5.13) or by modification of its right hand side. In general, it is not sufficient to simply set  $\mathbf{u}^*|_{\Gamma} = \mathbf{u}_b^n$  as an approximation of equation (5.16), as allowable in the explicit case. Since  $\mathbf{u}^*$  is solved to be a good approximation of  $\mathbf{u}^{n+1}$ , inconsistencies arise if the intermediate velocity field's boundary conditions are still related to the old time-step  $n$ . This difference becomes less significant the more the steady state is approached.

However, the better but more complicated method is to discretise the boundary conditions directly by matrix manipulation. In this case, we require more memory, as three matrices for the three Helmholtz equations (5.13) have to be stored. Of course, these matrices are sparse, which is why all in all we only store 9 vectors. As an advantage, most kinds of boundary conditions have to be set only once during the matrix initialisation phase, since they do not change throughout the computation.

All in all, there are five different combinations of tangential and normal boundary conditions on obstacles or outer boundaries to be considered.

1. One solid cell in normal direction (Fig. 5.2(a)).
2. One solid cell in tangential direction (Fig. 5.2(b)).
3. One solid cell in tangential and one solid cell in normal direction (Fig. 5.2(c)).
4. Two solid cells in tangential directions (Fig. 5.2(d)).
5. Two solid cells in tangential directions and one solid cell in normal direction (Fig. 5.2(e)).

In the following, we describe the implementation of the boundary conditions by considering the velocity component  $u$ . We suppose that we are dealing with a very general discretisation of the Laplacian of  $u$  which reads

$$\begin{aligned} [u_{xx}]_{i-1,j,k} &= \omega_{l,i-1}u_{i-2,j,k} + \omega_{m,i-1}u_{i-1,j,k} + \omega_{r,i-1}u_{i,j,k} \\ [u_{yy}]_{i,j,k} &= \omega_{l,j}u_{i,j-1,k} + \omega_{m,j}u_{i,j,k} + \omega_{r,j}u_{i,j+1,k}, \end{aligned}$$

where  $\omega_{t,s}$  with  $t \in \{l, m, r\}$  and  $s \in \mathbb{Z}$  denotes the respective weights ( $l$ =left,  $m$ =middle,  $r$ =right) of the star. These weights, which are combinations of grid spacings  $\Delta x_i$ ,  $\Delta y_i$ , etc. (cf. eq. 5.9), form the matrix entries for the solution of the linear equation  $((I - (\Delta t/2\text{Re})\Delta)u = rhs)$  and have to be modified for the modeling of different boundary conditions. In the following, we write  $\omega_t = \omega_{t,i}$  and  $\tau_t = \omega_{t,j}$  for  $t \in \{l, m, r\}$  and  $i, j \in \mathbb{Z}$  and denote the modified weights by  $\omega_{t,\text{new}}$  and  $\tau_{t,\text{new}}$  respectively. Also, for simplicity, we do not specify the manipulations needed for the discretisation of  $((I - (\Delta t/2\text{Re})\Delta)u = rhs)$  but for its Poisson equation part  $\Delta u = rhs$ .

### No-Slip Boundary Conditions

Suppose no-slip boundary conditions have to be set, so the velocity vector has to vanish at the boundaries. Let us consider the possible fluid-solid combination described above.

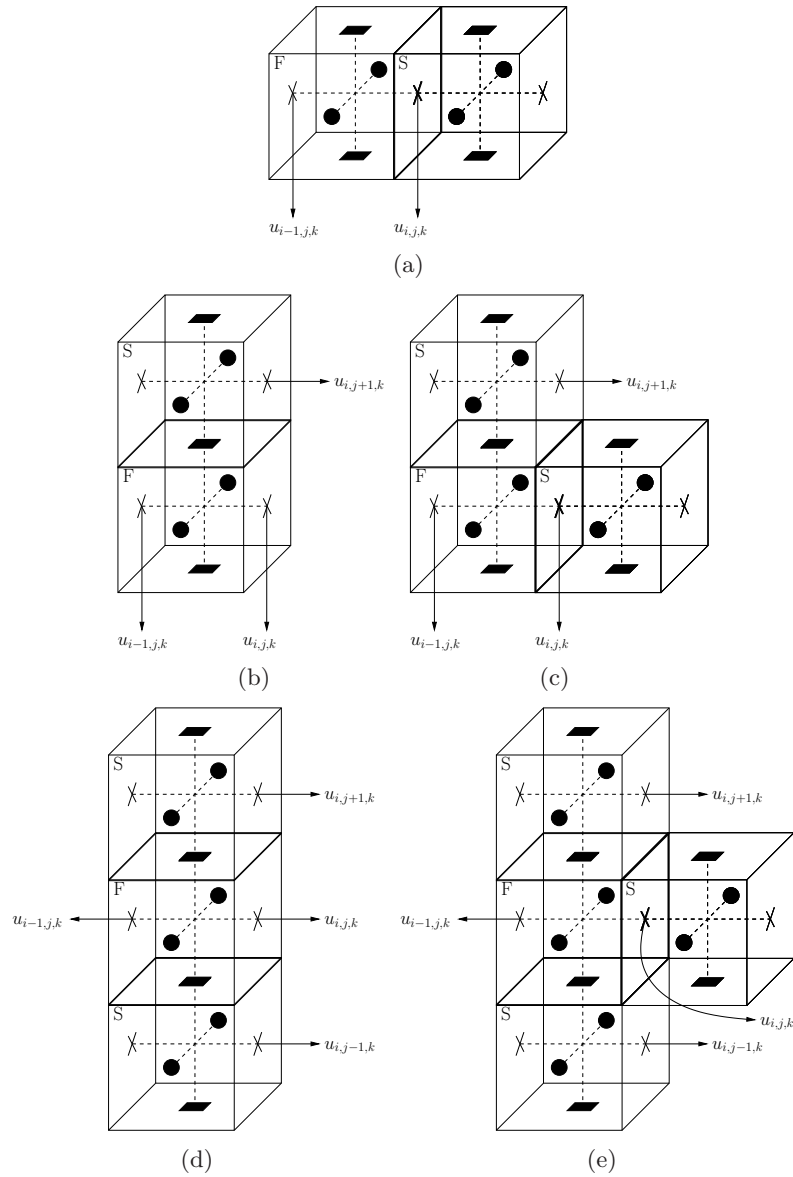


Fig. 5.2.: Possible combinations of tangential and normal boundary cells.  $S$  denotes solid and  $F$  denotes fluid cells.

- ad 1.** We want to impose  $u_{i,j,k} = 0$  at the border of the solid domain. Hence, we set the appropriate weight  $\omega_{r,\text{new}} = 0$  in the matrix.
- ad 2.** We want to impose  $u_{i,j+1,k} + u_{i,j,k}/2 = 0 \Rightarrow u_{i,j+1,k} = -u_{i,j,k}$ . This leads to a modification of the Laplacian

$$\begin{aligned} [u_{yy}]_{i,j,k} &= \tau_l u_{i,j-1,k} + \tau_m u_{i,j,k} + \tau_r u_{i,j+1,k}, \\ &= \tau_l u_{i,j-1,k} + (\tau_m - \tau_r) u_{i,j,k}, \end{aligned}$$

for which it is equivalent to set  $\tau_{m,\text{new}} = \tau_m - \tau_r$  and  $\tau_{r,\text{new}} = 0$ .

- ad 3.** We want to impose  $u_{i,j,k} = 0$ , as well as  $u_{i,j+1,k} + u_{i,j,k}/2 = 0$ . We set  $\omega_{r,\text{new}} = 0$ , as well as  $\tau_{r,\text{new}} = 0$ , since  $u_{i,j+1,k} = -u_{i,j,k} = 0$ .
- ad 4.** We want to impose  $u_{i,j+1,k} + u_{i,j,k}/2 = 0$ , as well as  $u_{i,j,k} + u_{i,j-1,k}/2 = 0$ . This means

$$\begin{aligned} [u_{yy}]_{i,j,k} &= \tau_l u_{i,j-1,k} + \tau_m u_{i,j,k} + \tau_r u_{i,j+1,k}, \\ &= (\tau_m - \tau_r - \tau_l) u_{i,j,k}, \end{aligned}$$

and can be achieved by setting  $\tau_{m,\text{new}} = \tau_m - \tau_r - \tau_l$ , as well as  $\tau_{r,\text{new}} = 0$  and  $\tau_{l,\text{new}} = 0$ .

- ad 5.** Again, set  $\omega_{r,i-1} = 0$  which leads to  $u_{i,j,k} = 0$ . Further, in application of (4), set  $\tau_{r,\text{new}} = 0$  and  $\tau_{l,\text{new}} = 0$ .

### Slip Boundary Conditions

Slip boundary conditions are modeled in a similar way. In this case the velocity component normal to the boundary should vanish, along with the normal derivative of the velocity component that is tangent to the boundary.

- ad 1.** Just like for no-slip boundaries.

- ad 2.** The normal derivative of the tangential velocity may be discretised as

$$(u_{i,j+1,k} - u_{i,j,k}) / \Delta x_i.$$

For this derivative to be zero, we have to ensure  $u_{i,j+1,k} = u_{i,j,k}$ . Then the Laplacian reads

$$\begin{aligned} [u_{yy}]_{i,j,k} &= \tau_l u_{i,j-1,k} + \tau_m u_{i,j,k} + \tau_r u_{i,j+1,k} \\ &= \tau_l u_{i,j-1,k} + (\tau_m + \tau_r) u_{i,j,k}, \end{aligned}$$

for which we modify the matrix by  $\tau_{m,\text{new}} = \tau_m + \tau_r$  and  $\tau_{r,\text{new}} = 0$ .

- ad 3.** We want to impose  $u_{i,j,k} = 0$ , as well as  $u_{i,j+1,k} = u_{i,j,k}$ . We set  $\omega_{r,\text{new}} = 0$  which would lead to  $u_{i,j+1,k} = 0$ . Therefore, we have to set  $\tau_{r,\text{new}} = 0$ .
- ad 4.** Similar to the no-slip case we set  $\tau_{m,\text{new}} = \tau_m + \tau_r + \tau_l$ , as well as  $\tau_{r,\text{new}} = 0$  and  $\tau_{l,\text{new}} = 0$ .
- ad 5.** Here, like in (3) we set  $\omega_{r,\text{new}} = 0$ , which leads to  $\tau_{r,\text{new}} = 0$ , as well as  $\tau_{l,\text{new}} = 0$ .

### Inflow Boundary Conditions

On an inflow boundary the velocities are explicitly given. This is enforced by imposing a fixed value for the velocities normal to the boundaries, while on tangential boundaries a linear interpolation between the velocities is required. Let us denote by  $u$  the given velocity at the boundary. Here, only cases (1) and (2) are of importance, since inflow conditions are specified on tangential or normal boundaries of the domain, not on obstacles.

**ad 1.** We want to impose  $u_{i,j,k} = u$  at the border of the solid domain. This condition is impossible to fulfil by mere matrix manipulation. Let us have a look at one part of the linear equation

$$\begin{aligned}
& [u_{xx}]_{i-1,j,k} + [u_{yy}]_{i-1,j,k} + [u_{zz}]_{i-1,j,k} = rhs_{i-1,j,k} \\
\Leftrightarrow & \omega_l u_{i-2,j,k} + \omega_m u_{i-1,j,k} + \omega_r u_{i,j,k} + [u_{yy}]_{i-1,j,k} + [u_{zz}]_{i-1,j,k} = rhs_{i-1,j,k} \\
\Leftrightarrow & \omega_l u_{i-2,j,k} + \omega_m u_{i-1,j,k} + \omega_r u + [u_{yy}]_{i-1,j,k} + [u_{zz}]_{i-1,j,k} = rhs_{i-1,j,k} \\
\Leftrightarrow & \omega_l u_{i-2,j,k} + \omega_m u_{i-1,j,k} + [u_{yy}]_{i-1,j,k} + [u_{zz}]_{i-1,j,k} = rhs_{i-1,j,k} - \omega_r u.
\end{aligned}$$

Hence, we shift the value  $u$  with the appropriate weight  $\omega_r$  and have to remember to fill the slot with  $\omega_{r,new} = 0$  in the matrix.

**ad 2.** We fix the tangential velocity by  $(u_{i,j+1,k} + u_{i,j,k})/2 = u$ , which means  $u_{i,j+1,k} = 2u - u_{i,j,k}$ . Then the equation can be modified to

$$\begin{aligned}
& [u_{xx}]_{i-1,j,k} + [u_{yy}]_{i-1,j,k} + [u_{zz}]_{i-1,j,k} = rhs_{i-1,j,k} \\
\Leftrightarrow & [u_{xx}]_{i-1,j,k} + \tau_l u_{i,j-1,k} + \tau_m u_{i,j,k} + \tau_r u_{i,j+1,k} \Leftrightarrow + [u_{zz}]_{i-1,j,k} = rhs_{i-1,j,k} \\
\Leftrightarrow & [u_{xx}]_{i-1,j,k} + \tau_l u_{i,j-1,k} + \tau_m u_{i,j,k} + \tau_r (2u - u_{i,j,k}) + [u_{zz}]_{i-1,j,k} = rhs_{i-1,j,k} \\
\Leftrightarrow & [u_{xx}]_{i-1,j,k} + \tau_l u_{i,j-1,k} + (\tau_m - \tau_r) u_{i,j,k} + [u_{zz}]_{i-1,j,k} = rhs_{i-1,j,k} \\
& \qquad - 2\tau_r u.
\end{aligned}$$

In addition to the modification of the right hand side, we set  $\tau_{m,new} = \tau_m - \tau_r$  and  $\tau_{r,new} = 0$ .

### Natural Outflow Boundary Conditions

For outflow boundary conditions the normal derivatives of both the tangential and normal component of the velocity are set to zero to model the continuity of the velocity in direction of the boundary. In the discrete case this can be achieved by setting the velocity values in the boundaries equal to the velocity values inside the fluid domain. This also means, that the tangential component of the velocity is discretised in the same manner as done in the slip case. Like for the inflow case, we only have to specify (1) and (2).

**ad 1.** We want to impose  $u_{i,j,k} = u_{i-1,j,k}$  at the border of the solid domain.

$$\begin{aligned}
[u_{xx}]_{i-1,j,k} &= \omega_l u_{i-2,j,k} + \omega_m u_{i-1,j,k} + \omega_r u_{i,j,k} \\
&= \omega_l u_{i-2,j,k} + (\omega_m + \omega_r) u_{i-1,j,k}
\end{aligned}$$

Hence, we set  $\omega_{m,\text{new}} = \omega_m + \omega_r$  and  $\omega_{r,\text{new}} = 0$ .

**ad 2.** Just like for slip-conditions.

**Periodic Boundary Conditions**

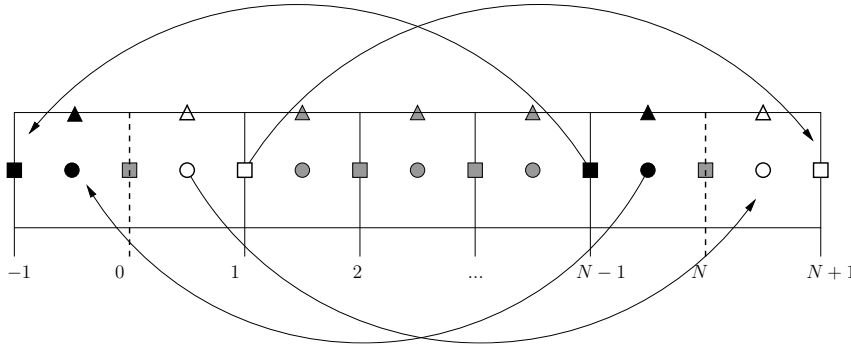


Fig. 5.3.: Simplified diagram of the exchange of periodic boundary conditions. Depicted is the exchange of values in  $x$ -direction for the 2D-case. Circles represent the discretisation of the pressure values, triangles the velocity  $v$  and squares the velocity  $u$ . The dashed line is where the first and last cells can be imagined to be glued to each other to model periodicity.

Periodic boundary conditions model a cubical simulation box that is replicated throughout space to form an infinite lattice. Their discretisation poses an entirely different problem than the conditions described above. In the explicit case periodic values at the boundary are exchanged as demonstrated in Figure (5.3).

Let  $N$  and  $M$  denote the maximum number of grid cells in  $x$ - and  $y$ -direction. In order to show how periodic boundaries should be discretised in the implicit case, let us consider a one-dimensional Poisson problem  $\Delta u = rhs$ . A first intuitive guess based on Figure (5.3) could be to write the associated matrix and vector as

$$\begin{pmatrix} \omega_{m,1} & \omega_{r,1} & 0 & \dots & \dots & \dots & \omega_{l,0} \\ \omega_{l,2} & \omega_{m,2} & \omega_{r,2} & 0 & \dots & \dots & \dots \\ 0 & \omega_{l,3} & \omega_{m,3} & \omega_{r,3} & 0 & \dots & \dots \\ \dots & \ddots & \ddots & \ddots & \dots & \dots & \dots \\ \dots & 0 & \omega_{l,N-2} & \omega_{m,N-2} & \omega_{r,N-2} & 0 & \dots \\ \dots & \dots & 0 & \omega_{l,N-1} & \omega_{m,N-1} & \omega_{r,N-1} & \dots \\ \omega_{r,N} & 0 & \dots & 0 & \omega_{l,N} & \omega_{m,N} & \dots \end{pmatrix} \begin{pmatrix} u_1 \\ u_2 \\ u_3 \\ \vdots \\ u_{N-2} \\ u_{N-1} \\ u_N \end{pmatrix}$$

Thus, we imply  $u_{N+1} = u_1$ , as well as  $u_0 = u_N$ . This last value has to be exchanged before and after the solution of the Helmholtz system, in addition to the exchange of the two velocity values in the explicit case. If we solve for  $u$  in some tangential direction, the

matrix has exactly the same structure and we solve again from  $j = 1, \dots, M$  to ensure that  $u_M + 1 = u_1$  and  $u_0 = u_M$ , but no third value has to be exchanged as necessary in the normal direction of  $u$ .

### 5.3. Discretisation of the Brinkman Equations

The penalised Brinkman equations (4.3) are very similar to the Navier-Stokes equations (5.1-5.3), and the same discretisation methods are used. We solve the Brinkman equations on the whole domain with  $\mathbf{K} = \infty$  at fluid points, while on the microscale  $\mathbf{K}$  typically varies between  $10^{-4} \leq \mathbf{K} \leq 10^{-9}$  in our computations. With the inclusion of the Brinkman terms, the Adams-Bashforth-Crank-Nicolson discretisation of the equations reads

$$\begin{aligned} \frac{\mathbf{u}^{n+1} - \mathbf{u}^n}{\Delta t} + \mathcal{H}^n(\mathbf{u}) + \nabla p^{n+\frac{1}{2}} &= \frac{1}{2\text{Re}} \Delta(\mathbf{u}^{n+1} + \mathbf{u}^n) - \frac{\mathbf{K}}{2\text{Re}}(\mathbf{u}^{n+1} + \mathbf{u}^n) \\ \nabla \cdot \mathbf{u}^{n+1} &= 0. \end{aligned} \quad (5.17)$$

Thus, we discretise the additional Brinkman term implicitly with the Crank-Nicolson scheme. Therefore, no additional time-step restriction for the stability of the Navier-Stokes/Brinkman equations is necessary. In the projection method, it is only the first step that has to be modified.

**Step 1:** Solve the momentum equations for the intermediate velocity field  $\mathbf{u}^*$ :

$$\begin{aligned} \left( I - \frac{\Delta t}{2\text{Re}} (\mathbf{K}^{-1} + \Delta) \right) \mathbf{u}^* &= \\ \mathbf{u}^n - \Delta t \cdot \left( \mathcal{H}^n(\mathbf{u}) + \nabla p^{n-\frac{1}{2}} - \frac{\Delta t}{2\text{Re}} (\mathbf{K}^{-1} - \Delta) \mathbf{u}^n \right). \end{aligned} \quad (5.18)$$

### 5.4. Implementation of Darcy's Law

Recall that we use Darcy's Law only for the computation of permeability. Hence, we solve the Stokes or Navier-Stokes equations, and use the steady-state solutions  $\mathbf{u}^s$  and  $p^s$  to solve Darcy's Law for  $\mathbf{K}$ . Thus, we discretise  $\mathbf{u}$  and  $p$  in Darcy's Law on the same staggered grid. As explained in Section 2.2.2, we solve the Stokes- or Navier-Stokes equations three times imposing periodic boundary conditions up to a constant gradient for the pressure once in  $x$ -, once in  $y$ - and once in  $z$ -direction. Since in all the computations in this thesis the pressure gradients that evolve in all other directions are negligible, we compute  $\mathbf{K}$  from

$$\begin{aligned} K_{xx} &= \left( \frac{\partial p^{s_x}}{\partial x} \text{Re} \right) / \left( \frac{L^2}{|\Omega_h|} \int_{\Omega_h} u^{s_x} dx \right) \\ K_{yy} &= \left( \frac{\partial p^{s_y}}{\partial y} \text{Re} \right) / \left( \frac{L^2}{|\Omega_h|} \int_{\Omega_h} v^{s_y} dy \right) \\ K_{zz} &= \left( \frac{\partial p^{s_z}}{\partial z} \text{Re} \right) / \left( \frac{L^2}{|\Omega_h|} \int_{\Omega_h} w^{s_z} dz \right), \end{aligned} \quad (5.19)$$

where the subscripts  $x$ ,  $y$  and  $z$  denote the solutions computed by the imposed pressure gradient in the respective direction.

---

**Algorithm 5.4.1:** DARCY AND BRINKMAN IN SEMI-IMPLICIT ALGORITHM( $\mathbf{u}, p$ )

---

```

{ Set boundary conditions for the  $\Delta$  part of Helmholtz matrix.
  Set  $t=0$ .
  Assign initial values to  $\mathbf{u}$ ,  $p$ ,  $\mathbf{K}_B$ .
main
while  $t \leq t_{\text{end}}$ 
  { Select  $\Delta t$ .
    Set boundary conditions for  $\mathbf{u}$ ,  $p$ .
    if CompBrinkman
      then Compute  $F^{(n)}$ ,  $G^{(n)}$ ,  $H^{(n)}$  as the RHS of eq. (5.17).
      else Compute  $F^{(n)}$ ,  $G^{(n)}$ ,  $H^{(n)}$  as the RHS of eq. (5.13).
    Set necessary runtime boundary conditions for  $\mathbf{u}^*$ .
    do if CompBrinkman
      then Solve the Helmholtz system for  $\mathbf{u}^*$  according to eq. (5.17).
      else Solve the Helmholtz system for  $\mathbf{u}^*$  according to eq. (5.13).
    Compute RHS of pressure Poisson equation (5.14).
    Solve pressure Poisson equation (5.14) for pressure difference  $\phi^{(n+1)}$ .
    Compute  $\mathbf{u}^{(n+1)}$  according to eqs. (5.14).
    Compute  $p^{(n+1/2)}$  according to eq. (5.15).
     $t = t + \Delta t$ .
  Solve Darcy's Law (5.19) for the permeabilty  $\mathbf{K}_D$ 

```

---

## 5.5. Implementation of the Unit Cell Problem

Recall that the cell problem in homogenisation theory is to find  $(\mathbf{w}_i, \pi_i) \in H_{\text{per}}^1(Y)^n \times L^2(Y)$  for  $1 \leq i, j \leq n$  such that

$$\begin{aligned}
 -\Delta \mathbf{w}^i + \nabla \pi^i &= \mathbf{e}^i && \text{in } Y_F \\
 \nabla \cdot \mathbf{w}^i &= 0 && \text{in } Y_F \\
 \mathbf{w}^i &= 0 && \text{on } \partial Y_F \setminus \partial Y \\
 \mathbf{w}^i, \pi^i &&& Y - \text{periodic.}
 \end{aligned}$$

where  $\mathbf{e}^i$  denotes the vector with components  $e_j^i = \delta_{ij}$ . Then the permeability tensor is defined by

$$K_{ij} = \int_{Y_F} \nabla_y \mathbf{w}^i \nabla_y \mathbf{w}^j dy \text{ for } 1 \leq i, j \leq n.$$

Looking at this problem from a numerical point of view, its solution amounts to three Stokes equations with external forces  $(\mathbf{e}^i)_{1 \leq i \leq 3}$  from which we obtain “the velocities”  $(\mathbf{w}^i)_{1 \leq i \leq 3}$  for the input of  $\mathbf{K}$ . The discretisation of the Unit Cell Problem is then equivalent to the discretisation of the Stokes equations.

## 5.6. Numerical Analysis of the Semi-Implicit Solver

### 5.6.1. Lid-Driven Cavity Flow

The lid-driven cavity flow is considered a classical problem for the assessment of numerical methods and the validation of Navier-Stokes codes [27]. The fluid motion is usually studied in the two-dimensional domain  $\Omega = ]0, 1[ \times ]0, 1[$ . Since we would like to test the implemented flow solver in three dimensions, we modify the domain to  $\Omega_h = ]0, 1[ \times ]0, 1[ \times ]0, 0.5[$  and set periodic boundary conditions in  $z$ -direction, of which we assume that they do not disturb the flow field in  $x$ - and  $y$ -direction. The associated boundary conditions for the other side surfaces are  $\mathbf{u} = (1.0, 0.0, 0.0)$  on  $y = 1$  and no-slip conditions on the remaining boundary surfaces. The discrete domain is resolved by  $128 \times 128 \times 6$  grid cells.

For a Reynolds number  $\text{Re} = 100$ , we test the correctness of the solution procedure by comparing the results of our semi-implicit pressure correction method to those by Ghia, Ghia and Shin [27]. The convective terms are discretised by the VONOS scheme [21], we employ an SSOR Preconditioned Conjugate Gradient method for the solution of the Helmholtz equations of the velocities and the BiCGStab method for the solution of the pressure Poisson equation.

Thus, we plot the velocity component  $u$  along the  $y$ -line passing through the geometric centre of the cavity compared to typical points along this line as computed in [27]. These computations coincide exceedingly well (Fig. 5.4). In the same figure, the stream function  $\Psi$  is plotted, whose values at any two points gives the volumetric flow rate through a line connecting the two points

$$u = -\frac{\partial \Psi}{\partial y} \quad \text{and} \quad v = \frac{\partial \Psi}{\partial x}.$$

The vorticity contours in Figure 5.4 correspond to the streamline patterns and agree well in number and location compared to figures in [27]. They show, for instance, the offset of the centre of the primary vortex towards to the top right centre - for higher Reynolds numbers these vortices move back to the geometric centre of the cavity [27].

### 5.6.2. Convergence Analysis

In this section we establish that the solution of the Navier-Stokes equations by the semi-implicit pressure correction method fulfils the important properties of consistence, stability and convergence. Thus, a numerical scheme is consistent if its discrete operator converges

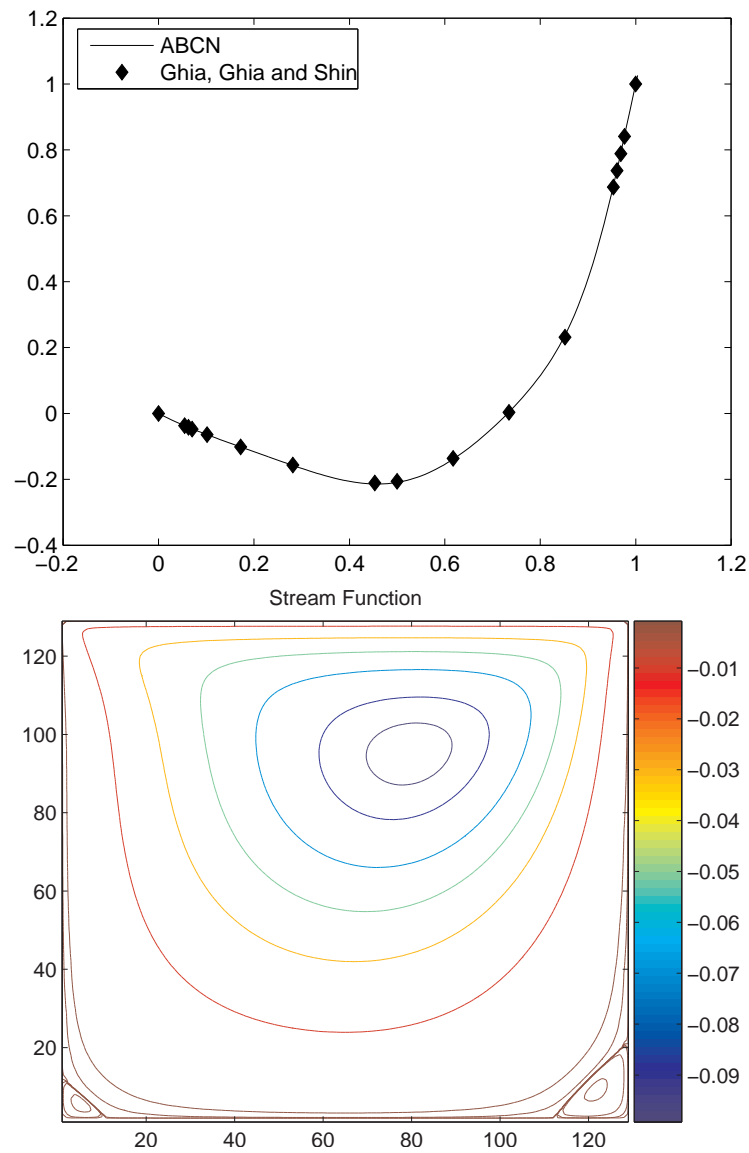


Fig. 5.4.: Results for the velocity component  $u$  along the vertical line through the geometric centre of the cavity (above). Streamline pattern for primary, secondary, and additional vortices (below).

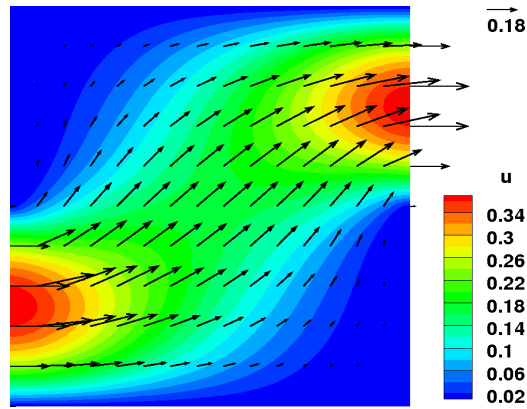


Fig. 5.5.: 2D cut of the flow and vector field of the parabolic inflow numerical experiment at  $t = 0.02$ . On the left, we set a parabolic inflow profile up to half of the box height, on the right an equally parabolic outflow profile on the upper half of the box side is specified

towards the continuous operator of the PDE for time-step and mesh size tending to zero, which means that in this limit the truncation error has to vanish. Further, a numerical solution method is stable, if it does not magnify errors that appear in the course of the numerical solution process, which states that the solution has to be bounded for temporal problems and that it may not diverge for iterative methods [25]. In addition, the numerical method is said to be convergent if the solution of the discretised equation tends to the exact solution of the PDE for the grid spacing tending to zero.

For these important properties, the Lax equivalence theorem states, that if a finite difference discretisation of a linear initial value problem satisfies the consistency condition, stability is the necessary and sufficient condition for convergence [25]. However, for non-linear problems, stability and convergence of a method are difficult to establish, since they are strongly influenced by the boundary conditions. Therefore, we check convergence by numerical experiments, in which the numerical computation is repeated on a series of successively refined grids. Convergence to a grid-independent solution can be found, if the method is stable and if all approximations used in the discretisation process are consistent.

Thus, for sufficiently fine grids, the discretisation error can be estimated from the difference between solutions on refined grids, and we estimate the order  $o$  of the scheme as

$$o = \frac{\log \left( \frac{\|\psi_{2h} - \psi_{4h}\|_k}{\|\psi_h - \psi_{2h}\|_k} \right)}{\log 2}, \quad (5.20)$$

where  $\Psi_h$ ,  $\Psi_{2h}$  and  $\Psi_{4h}$  denote the solution on the grid with mesh size  $h$ ,  $2h$  and  $4h$  respectively,  $\Psi$  stands for the components of the velocity or the pressure, and  $k$  represents the norm in which these magnitudes are measured.

We measure the convergence rate of the semi-implicit pressure correction scheme in a domain  $\Omega = [0.5]^3$  discretised on three refined grids with  $30^3$ ,  $60^3$  and  $120^3$  grid cells. On

	$o$ by $L_h^1$ -norm	$o$ by $L_h^{\max}$ -norm
$u$	1.23	1.02
$v$	2.00	2.00
$w$	1.52	1.41
$p$	1.20	1.10

Table 5.1.: Convergence rates for the parabolic inflow problem (Fig 5.5).

the side face  $x = 0.0$ , we set a parabolic inflow profile up to half of the box height. On the side face  $x = 0.5$  we specify an equally parabolic outflow profile on the upper half of the box side and solve until specified time  $t = 0.02$ . For this example, the convective terms are discretised by the SMART scheme [21]. The resulting flow field in a 2D cut of  $\Omega$  is depicted in Figure 5.5.

The convergence rates are listed in Table 5.1 and were computed with the CFD analyzer package of the Tecplot software, which performs both the interpolation from coarse to fine grid and the computation of the order of the scheme via (5.20). Theoretically, all components of the discretisation are second-order accurate in time and space. Since we use a regular grid, the diffusive terms are discretised up to second order in space, and the SMART scheme, used for the convective terms, has the same discretisation error. Moreover, both the Adams-Bashforth as well as the Crank-Nicholson scheme are second order accurate in time. Such a convergence rate in the discrete  $L^1$ -norm could not be established in any of the employed test problems, which might indicate that some inconsistency in the implementation still exists. Instead, the convergence rate varies between 1 and 2 both in the  $L_h^1$ - and in the  $L_h^\infty$ -norm.

On a different note, a higher convergence rate cannot be expected in geometries with solid obstacles, especially not in complicated textile geometries, because of the first order approximation of the boundaries. Hence we expect, that the larger the boundary surface, the lower becomes the convergence rate. We demonstrate this in the unit cell of a parallel square array of cylinders, whose setup we explain in Section (8.3) in detail. Depending on their radii, these cylinders have different volume fractions, which is the fraction of the unit cell that is filled by solid. The Stokes equations are solved in the unit cells of the cylinders for three different volume fractions, each on three successively refined grids with  $40^3$ ,  $80^3$  and  $160^3$  grid cells. Figure 5.6 shows the resulting flow field in a 2D cut of the geometry. The cylinders in this figure, point into the  $x$ -direction of the domain and are represented well by the zero velocity contour lines.

For a lower cylinder volume fraction, the boundary surface is smaller, and accordingly, the convergence rate for the depicted velocity component  $u$  (Fig. 5.6) in the  $L_h^1$ -norm ranges from 1.136 for 62%, to 1.45 for 35% to 1.77 for 8% volume fraction.

### 5.6.3. Speed-Up Compared to Explicit Computations

Semi-implicit and explicit time-stepping are compared for an impermeable array of cylinders with a fixed volume fraction of 60% (Table 5.2). Permeability calculations are carried out

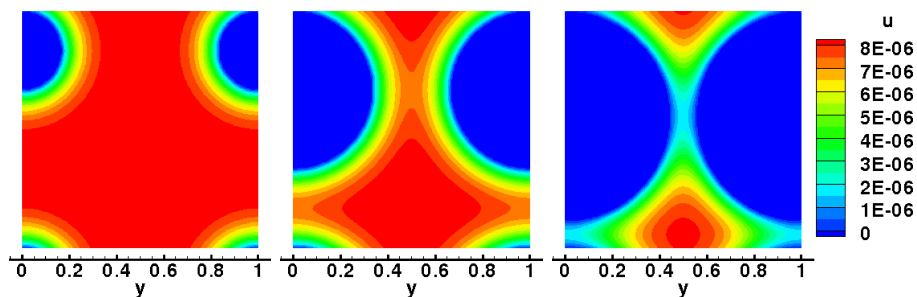


Fig. 5.6.: 2D cut of the flow field of a parallel square array of cylinders, from left to right with 8%, 35% and 62% volume fraction.

	Explicit	Semi-Implicit
#iter. Poisson	187713	14309
#iter. Helmholtz	–	893
$\Delta t$	$3.12 \cdot 10^{-5}$	$9.37 \cdot 10^{-4}$
$K_x(mm^2)$	$3.784 \cdot 10^{-3}$	$3.774 \cdot 10^{-3}$
Comp. Time	50m23s	03m37s

Table 5.2.: Computational results of the semi-implicit Adams-Bashforth-Crank-Nicolson vs. the explicit Forward Euler method.

on a  $(40^3)$  grid. Stopping criterion is convergence of the permeability. Both calculations are performed on an Intel(R) Xeon(TM) CPU, 3.20GHz.

The time-step size for the semi-implicit calculations is 30 times larger than for the explicit case. This does not result in a speed up in computational time of the same factor because of the extra costs of solving three Helmholtz equations per time-step. Still, in this case, the implicit solver is about 14 times faster than the explicit solver. Both methods result in accurate permeability values, whose difference is shown to vanish for finer grid spacings in Section 8.4.

## 6. Parallelisation

We have already made the serial version of our flow solver very efficient, by treating the momentum equations implicitly, by implementing a fast solver for the resulting Helmholtz matrices and by setting the associated boundary conditions preferably only once in the whole algorithm. We now want to accelerate our computations further by parallelisation. Thus, we aim at a reduction of the total computing time by dividing the work between several processors, which perform their computations to a certain extent simultaneously. In addition, memory requirements will be divided between the processors, which is desirable for the semi-implicit computations, where more vectors have to be stored for the Helmholtz matrices and their respective boundary conditions. In this chapter we address a number of parallel implementation aspects for our flow simulation model.

### 6.1. Parallelisation Strategy

NaSt3DGP [3] already works completely in parallel and employs the most natural ansatz for the parallelisation of the Navier-Stokes equations: the Cartesian grid is decomposed into  $p$  overlapping subdomains, which are in turn treated by one of the  $p$  processors. Therefore, individual processes no longer require access to the entire data structure and the solution of iterative algorithms can be divided among them. In addition, memory requirements for each processor reduce to the memory requirements of the processes running on it.

Furthermore, we can assure the convergence of the parallelised algorithm by an exchange of relevant data between processes treating adjacent subdomains (neighbouring processes). Each of the subdomains is extended by an artificial boundary, which guarantees the well-definedness of the equations on every process [21, 28]. The velocity and pressure values in these boundary strips are updated by communication with neighbours in every time step. Additionally, the pressure has to be communicated for each iteration of the Poisson solver. Unfortunately, the increased communication of a parallelised algorithm reduces the increase in speed provided by the simultaneous execution of the code.

Optimal speed-up can only be achieved if the computing load is distributed as evenly as possible among the processors. This can be done by dividing the domain into subdomains of nearly equal size, so that each processor treats approximately the same number of unknowns. Thus, to keep the communication costs as low as possible, the discrete domain  $\Omega_h$  is decomposed by minimisation of the cost functional

$$C(p^x, p^y, p^z) = \frac{N}{p^x} \frac{M}{p^y} + \frac{N}{p^x} \frac{P}{p^z} + \frac{M}{p^y} \frac{P}{p^z}$$

restricted by the side condition

$$p = p^x \cdot p^y \cdot p^z,$$

for  $p^x, p^y, p^z \in \mathbb{N}$  [21]. Here,  $N, M, P$  denote the number of grid cells in  $x$ -,  $y$ - and  $z$ -direction and  $p^x, p^y, p^z$  the number of processes in these directions. If  $p^x, p^y, p^z$  are factors of  $N, M, P$ , a domain decomposition into uniform cuboids results. However, if the domain is filled with obstacles, this strategy will only be of moderate success, since we cannot always guarantee the uniform distribution of the obstacles onto the processes.

For the communication between processes the computer communications protocol Message Passing Interface (MPI) is employed [4]. MPI was designed for high performance on both massively parallel machines and on workstation clusters and is a standard for communication among nodes in a parallel program. The implementation consists of a library of routines that can be called from C, C++ and other programs. MPI is both portable and fast, since it has been implemented on almost every distributed memory architecture and is optimised for each hardware on which it runs.

All computations are performed on the parallel computer Himalaya of the Institute of Numerical Simulation and the Sonderforschungsbereich 611 at the University of Bonn. The cluster has its own Myrinet infrastructure, allowing fast communication between the 128 compute nodes separated from the service ethernet and without the TCP/IP protocol overhead. Himalaya performs 1269 GFlop/s in the Linpack benchmark test. Each cluster node (Dell PowerEdge 1850) contains two Xeon EM64T 3.2 Ghz processors and 2 GBytes of main memory. Further, each node is equipped with Myrinet/XP network interfaces connected to a Clos256 switch.

## 6.2. Parallelisation of the Semi-Implicit Solver

The parallel implementation of the semi-implicit solver requires further communication as opposed to the explicit case. Regarding the employed Conjugate Gradient Method, parallelisation is straightforward, and we do not explain it in detail here. However, we note, that the SSOR preconditioner could only be applied block by block, producing minor  $p$  dependent inconsistencies. Instead, we opt for a simple to parallelise Jacobi preconditioner. In the CG algorithm a matrix-vector multiplication is used, which also accesses boundary values. Therefore, in every iteration, these values have to be communicated to neighbouring processes.

Further communication for the implicit solver is required to account for periodic boundary conditions. Remember that in this case, in the sequential semi-implicit algorithm, the exchange of the values  $u_0 = u_N$  became necessary. This exchange carries over to the parallel case and the respective situation is shown in Figure 6.1: the dashed line represents the boundaries of the processes' subdomains, to which another grid cell has to be added for local boundary conditions. On these overlapping grid cells, communication is necessary to ensure that each process obtains the most up-to-date values. The rectangular array depicts the same extra boundary value exchange as necessary in the sequential case. However, in the parallel case, this value has to be further communicated from process  $p$  to the neighbouring process  $p - 1$ .

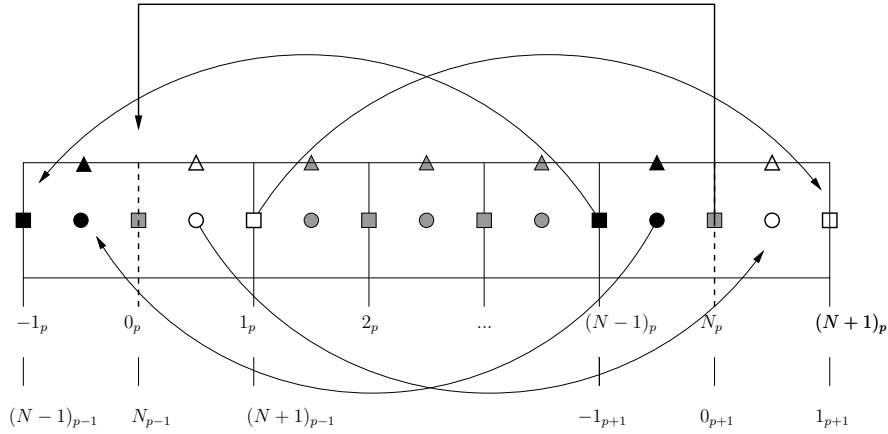


Fig. 6.1.: Simplified 2D diagram for the exchange of periodic boundary conditions. Depicted is the exchange of values in  $x$ -direction. Circles represent the discretisation of pressure values, triangles the velocity  $v$  and squares the velocity  $u$ . Round arrows denote the exchange of boundary values in the explicit case, the angular array denotes the further necessary exchange in the semi-implicit case. All of these values have to be communicated to the processes  $p - 1$  and  $p + 1$  as well.

### 6.3. Speed-Up and Efficiency of the Parallelised Solver

Efficiency of the parallelisation depends on how well the computing load is distributed across the processors, and on how low the communication costs can be kept compared to the gain in speed. Given that the grid is sufficiently fine and that enough processors are employed, we might achieve considerable increase in computing speed. This acceleration is measured in terms of speed-up and efficiency

$$S(p) \equiv \frac{T(1)}{T(p)} \quad \text{and} \quad E(p) \equiv \frac{T(1)}{p \cdot T(p)} = \frac{S(p)}{p}, \quad (6.1)$$

with  $p$  again the number of processors and  $T(p)$  the execution time of the parallel algorithm running on  $p$  processors.

In the following we investigate two different settings in order to measure the effectiveness of our parallelisation strategy. First, we consider a fixed geometry which is divided among an increasing number of processors. In a second step, we increase the size of the geometry along with the number of processors, since in textile applications, we often have to compute the permeability of multi-layered media (Fig. 6.2). With this last variant we measure the so-called scale-up.

We calculate speed-up and efficiency of the parallelised code in the fixed geometry of a unit cell with a sphere of radius  $r = 0.25$ , which is resolved by  $60 \times 60 \times 60$  grid cells. We employ periodic boundary conditions except for one direction, where a constant gradient for the pressure is specified. Computations are performed until time  $t = 0.026264$ , which takes the semi-implicit solver exactly 64 time steps. The pressure Poisson equation is solved

$p$	$T(p)$ in sec.	$S(p)$	$E(p)$ in %
1	2583.49	1.00	100
2	1337.33	1.93	96.60
4	670.27	3.85	96.36
8	341.78	7.56	94.49
16	214.87	12.02	75.15
32	98.76	26.16	81.75
64	56.20	45.97	71.38

Table 6.1.: Speed-up and efficiency measurements with the Helmholtz system solved by a Jacobi preconditioned CG method.

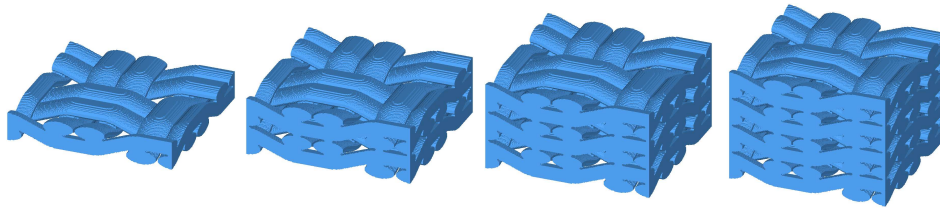


Fig. 6.2.: Non-nested layering of the Monofilament Fabric Natta 2115.

by a Jacobi preconditioned BiCGStab method and the semi-implicit system is solved by a Jacobi preconditioned Conjugate Gradient Method (Table 6.1). Note that due to the costs for communications, the optimal values  $S(p) = p$  and  $E(p) = 100\%$  are unachievable.

In Table 6.1 we observe that the efficiency decreases with the number of processors, which is to be expected, since communication becomes more and more costly. However, for 64 processors we still get an efficiency of 71.38% which is good considering that each processor's subdomain consists of only  $15 \times 15 \times 15$  grid cells then.

In case of 16 processors there is a sudden decrease in efficiency and speed-up. For 16 processors the domain is not decomposed into cuboids, but into rectangles, where each processor treats  $30 \times 30 \times 15$  grid cells. Thus, a larger surface between the processors' subdomains evolves, which results in increased communication on this interface. On a different note, the load balances might also be sub-optimal, since we do not take into consideration obstacles for the decomposition of the domain. Thus, due to the decomposition into cuboids or rectangles, it might even be possible, that one of the processors is "doing nothing", since its respective subdomain is wholly enclosed in a solid obstacle.

Textile engineers often require computations in multi-layered textiles, since permeability strongly depends on the packing of a textile. Consider as an academic example, the non-nested layering of the Monofilament Fabric Natta 2115 (Fig. 6.2). In this case, the same permeability  $\mathbf{K}$  should be obtained for all five computed layers, whereas in a maximally nested setup the permeability would decrease for two or more layers. The number of grid

Layers	time	$p$	$\mathbf{K}_{xx}$	# z-cells
1	2h 19m	8	3.289e-04	40
2	2h 31m	16	3.289e-04	80
3	2h 22m	24	3.289e-04	120
4	2h 32m	32	3.289e-04	160
5	2h 38m	40	3.289e-04	200

Table 6.2.: Parallel execution times in a geometry of up to five layers of Natte Monofilament fabric.

cells in  $x$ - and  $y$ -direction remains constant (226 and 216), while the number of grid cells in  $z$ -direction is successively increased, so that for each additional layer the domain is decomposed into cuboids of the same size. Table 6.2 shows that such layered geometries can be computed in nearly the same time by a respective increase in processors. Again, good parallel execution lacks for  $p = 16$ . However, computing five layers in parallel takes only 8% additional time compared to the computation of one layer.



## 7. Numerical Homogenisation

In Chapter 3 of this thesis we used the analytic method of homogenisation to derive fluid flow equations that hold on the macroscale of a porous medium, and considered in a next step how these equations can be solved numerically. In this chapter we address the following validation issues of our numerical computations:

- Comparison of the numerically computed permeability with other semi-analytical and numerical methods (numerical computation of permeability is scarce in literature).
- Numerical equivalence of solving Darcy's Law for the permeability in a repeat cell of the porous medium and of solving the Unit Cell Problem arising from homogenisation theory (theoretically, they should give the same results).
- Comparison of direct numerical simulation on the microscale as opposed to the numerical solution of homogenised equations and of the Stokes/Brinkman equations (since the latter are merely an approximation of the first).

Furthermore, we give numerical evidence that in simple periodic as well as in textile geometries, the solution of the Stokes equations as opposed to the Navier-Stokes equations is sufficient, and in a last step, we shortly discuss the question if the Stokes/Brinkman equations really satisfy Darcy's Law in the porous part of the coupled fluid/porous domain.

The packed beds of spheres, which are considered in this chapter, are employed in the numerical simulation of filters, catalytic packs or heat exchangers. Furthermore, we note here for later application, that the porosity of a medium depends strongly on its packing structure. For example, in beds of solid spheres the porosity varies between the limits 0.2545 for rhombohedral packing and 0.4764 for quadratic/cubic packing (Fig. 7.1).



Fig. 7.1.: 2D cut of a packed bed of spheres with cubic packing (left) and rhombohedral packing (right).

## 7.1. Validation of Permeability Computations in a Cubic Array of Spheres

We validate our numerical permeability computations in porous media consisting of cubic arrays of spheres. Figure 7.4 shows such a medium in three dimensions for two different sphere radii. In the two-dimensional case, we compare our computations to numerical permeability solutions by Neuss [48] and by Bang and Lukkassen [14], whereas in the three-dimensional case semi-analytical permeability data by Sangani and Acrivos [54] is available for comparison.

Note, that a sphere is an isotropic geometrical object, so the permeability tensor takes the form  $\mathbf{K} = K_{xx}\mathbf{I}$ , which is why we are only interested in the first permeability tensor entry. Also, in this case Darcy's Law can be simplified to

$$K_{xx} = -\frac{q_x}{\frac{\partial p}{\partial x}}. \quad (7.1)$$

### 7.1.1. The Two-Dimensional Case

In order to perform the necessary 2D computations we implemented the Unit Cell Problem in the freely available flow solver NaSt2D [28]. For a fixed sphere radius  $r = 0.25$  and an increasing number of grid cells the calculated permeabilities are given in Table 7.1.

Numerical solutions for the permeability are also computed by Neuss [48], who employs a multigrid solver and obtains the first entry of the permeability tensor as  $K_{xx} = 1.9901$  on 256 cells. A result, which was unobtainable in three dimensions, because of the multigrid solver's memory consuming implementation [48]. Bang and Lukkassen [14] employ the software Flow3D to compute permeability results in two and three dimensions. Unfortunately, they do not specify their results to more than two digits, so we cannot conclude much concerning the quality of their solver.

Note, that we are already very close to Neuss' result, but as was to be expected, the convergence of the permeability is very slow employing the NaSt2D finite difference solver. In this respect, spheres are already a quite demanding example, since on the one hand, solid cells at the sphere surface are deleted if they are inconsistent with the boundary conditions, and on the other hand, boundary conditions on the sphere surface can only be approximated to first order accuracy<sup>1</sup>.

### 7.1.2. The Three-Dimensional Case

In this section we compare three-dimensional numerical results of the permeability of a cubic array of spheres with analytical results. For this geometry Sangani and Acrivos [54] found general solutions of the Stokes equations in series formulation, whose coefficients are determined numerically. For several volume fractions the authors compute the dimensionless drag force  $F$  to which the first entry of the permeability tensor is related by  $K_{xx} = \frac{1}{6}\pi r F$ ,

---

<sup>1</sup>However, the simple cell decomposition and enumeration technique of the approximation by voxels has the great advantage that even more complex geometries can be handled without difficult and time consuming mesh generations.

Resolution	$K_{xx}$ Cell Problem	$K_{xx}$ Bang et al. [14]
$10^2$	2.079e-02	2.5e-02
$20^2$	1.647e-02	2.3e-02
$40^2$	1.804e-02	2.1e-02
$60^2$	1.837e-02	2.1e-02
$80^2$	1.885e-02	2.1e-02
$100^2$	1.899e-02	2.0e-02
$140^2$	1.933e-02	–
$300^2$	1.960e-02	–

Table 7.1.: Numerical approximation of the permeability  $K_{xx}$  in the 2D case with different grid resolutions, compared to results by Bang and Lukkassen [14].

with  $r$  the sphere radius.

Darcy’s Law holds on the macroscale of the porous medium, so it must also be valid in a periodic repeat cell of the medium, i.e. in the unit cell. That means, we compute the flow field with the Stokes equations in the unit cell and obtain  $\mathbf{K}$  from the applied pressure drop and the average velocity field in Darcy’s Law (7.1). In contrast, the same permeability is obtained by solving the Unit Cell Problems (3.13) as defined by homogenisation theory.

Both the permeabilities from numerical simulations as well as the semi-analytical ones are listed in Table 7.2 for various values of  $\chi = (V_f/V_{f\max})^{1/3}$ , which are scaled sphere volume fractions: the volume fractions  $V_f$  denotes the total fraction of the unit cell that is occupied by solid, which is here  $V_f = 4\pi r^3/3L^3$ . Further,  $V_{f\max} = \pi/6$  corresponds to the case when the spheres are in contact. We only present a selection of values in Table 7.2 - but the computed permeabilities for in between volume fractions are plotted in Figure 7.2 in comparison to the semi-analytical ones. Note, that the different resolution for  $\chi = 1.00$  was a priori chosen to guarantee a sufficient number of fluid cells between sphere surface and domain boundary to ensure the stability of the solution.

First of all, we note that all the values are in good agreement with those obtained analytically by Sangani and Acrivos [54] and deviate no more than 2% from them. Furthermore, the results obtained by the solution of the Unit Cell Problems and by Darcy’s Law are equal. This was to be expected as in homogenisation theory the cell problem is just an auxiliary problem for the definition of the permeability tensor and the derivation of Darcy’s Law.

Although the permeability by Darcy’s Law and by the Unit Cell Problem are equivalent, there is a difference in the evaluation of the computational data that forms the input of  $\mathbf{K}$ , if the medium is anisotropic. In both cases we have to solve three Stokes problems, but for the Unit Cell Problems all entries of the permeability tensor are directly available via the more general relationship  $K_{ij} = \int_{Y_F} \nabla_y \mathbf{w}^i \cdot \nabla_y \mathbf{w}^j d\mathbf{y}$  for  $1 \leq i, j \leq 3$ , whereas the relationship via Darcy’s Law  $\mathbf{q} = \mathbf{K} \cdot \nabla p$  demands the solution of a linear system of equations as described in section 2.2.

Resolution	$\chi$	$K_{xx}$ Darcy's Law	$K_{xx}$ Cell Problem	$K_{xx}$ Sangani [54]
$60^3$	0.20	3.8135e-01	3.8135e-01	3.8219e-01
$60^3$	0.40	1.2314e-01	1.2314e-01	1.2327e-01
$60^3$	0.60	4.4280e-02	4.4280e-02	4.4501e-02
$60^3$	0.80	1.3118e-02	1.3118e-02	1.3197e-02
$100^3$	1.00	2.5083e-03	2.5083e-03	2.5203e-03

Table 7.2.: Computation of the permeability  $K_{xx}$  in a 3D array of spheres for different scaled volume fractions  $\chi$  and comparison to semi-analytical results.

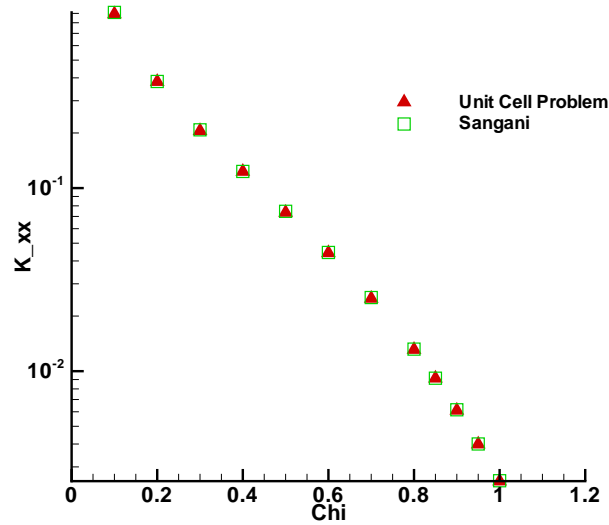


Fig. 7.2.: Computation of the permeability  $K_{xx}$  versus different scaled volume fractions  $\chi$  compared to semi-analytical results by Sangani and Acrivos [54].

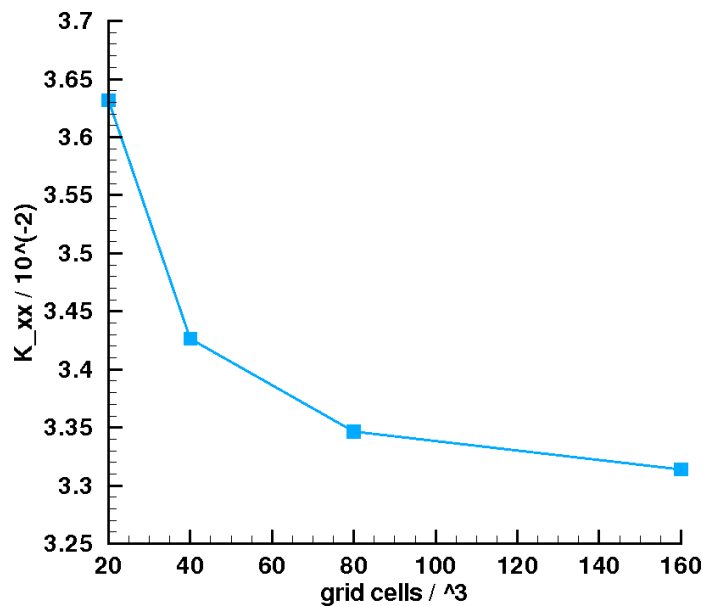


Fig. 7.3.: Computation of the permeability  $K_{xx}$  in a square array of boxes.

## 7.2. 3D Stokes versus Navier-Stokes Equations in an Array of Boxes

In this section we compare permeability computations by the Stokes and by the Navier-Stokes equations. Thus, we compute the permeability tensor in a square array of boxes for different grid resolutions, but as opposed to before, we now solve the Navier-Stokes equations and insert the resulting velocity and pressure into Darcy's Law at steady state. The computed permeabilities are depicted in Figure 7.3.

Furthermore, we measure the  $L_h^{\max}$ -norm of the convective term, which is the only term that distinguishes the Navier-Stokes and the Stokes equations. We find that its maximum for all resolutions in all computations was still less than  $3e-07$ , which is smaller than the minimum discretisation error on the finest grid  $1/160^2 = 4e-05$ . In textile applications, the observed magnitude of the convective terms was even less, and a number of tests showed their neglectability [60]. In Table 7.3, we further see a comparison between the computation of permeability via Darcy's Law and the Unit Cell Problems in complex textiles geometries. Here as well, they give the same results, which establishes also numerically, that homogenisation theory holds in the connected textile domain<sup>2</sup>. A thorough description of the different textile models can be found at the end of this thesis in Chapter 8.

<sup>2</sup>These results also confirm, that it is acceptable to neglect evolving pressure gradients for the computation of Darcy's Law via the Stokes or Navier-Stokes equations, since both Darcy's Law and the Unit Cell Problems give the same results (cf. Section 2.2.2) in the considered geometries.

Method for $K_{xx} / mm^2$	PSA $V_f$ 62%	Monofilament Fabric	Carbon Woven Fabric
Navier-Stokes & Darcy	3.4e-03	3.3e-04	4.2e-04
Stokes & Darcy	3.4e-03	3.3e-04	4.2e-04
Unit Cell Problem	3.4e-03	3.3e-04	4.2e-04

Table 7.3.: Computation of the permeability  $K_{xx}$  by different mathematical models in textiles.

### 7.3. Validation of Darcy's Law in a Cubic Array of Spheres

Let us compare the solution of the Stokes equations on the microscale and the solution of Darcy's Law on the macroscale in a cubic array of spheres for scaled sphere volume fractions  $\chi = 0.8$  and  $\chi = 0.4$ . The microscales are depicted in Figure 7.4 with their corresponding unit cells.

The solution of the Stokes equations in the microgeometries is time consuming, as it requires the resolution of every single sphere. The oscillations of the velocities arising from the periodic structure can be seen in Figure 7.5, where the velocity field in a 2D cut of the microgeometry is plotted. The averaging of these oscillations is the main aim of homogenisation theory, so we expect that the solution of Darcy's Law in the macrogeometry will approximately be the average value of the microscale velocities.

The resolution of the first geometry ( $\chi = 0.4$ ) is chosen as  $400 \times 200 \times 200$  gridcells and for the second ( $\chi = 0.8$ )  $200 \times 100 \times 100$  gridcells. As an example for the complexity of the computation consider that the solution of the Stokes equations in the first geometry on 40 processors on the parallel computer Himalaya still takes about 4 hours.

What would Darcy's Law in this case give? The Stokes equations are augmented with a constant pressure gradient  $\Delta P/L \approx 0.1$ . Further, the solution of the Unit Cell Problems yields the dimensionless  $K_{xx} = 1.2314e - 01$  if  $\chi = 0.4$  and  $K_{xx} = 1.3118e - 02$  if  $\chi = 0.8$  as shown in Table 7.2. Recall, that the dimensionless Darcy's Law in its very basic form reads

$$\mathbf{q} = \text{Re} \cdot \mathbf{K} \frac{\Delta p}{L} \quad (7.2)$$

and that we have to transform the dimensionless permeability  $K_{xx}$  by  $L^2$ , where  $L = 0.005$  denotes the length scale of the dimension-dependent unit cell of the microscopic medium (cf. Section 2.2.1). Hence we obtain for the effective velocity in  $x$ -direction

$$\begin{aligned} q_x^1 &= 1 \cdot 1.2314e - 01 \cdot 0.005^2 \cdot 0.1 = 3.08e - 07 \\ q_x^2 &= 1 \cdot 1.3118e - 02 \cdot 0.005^2 \cdot 0.1 = 3.30e - 08 \end{aligned} \quad (7.3)$$

On the other hand, computation of the mean velocity  $\bar{u}$  of the Stokes equations' solution in the microgeometry yields

$$\begin{aligned} \bar{u}^1 &= 3.05e - 07 \\ \bar{u}^2 &= 3.18e - 08, \end{aligned} \quad (7.4)$$

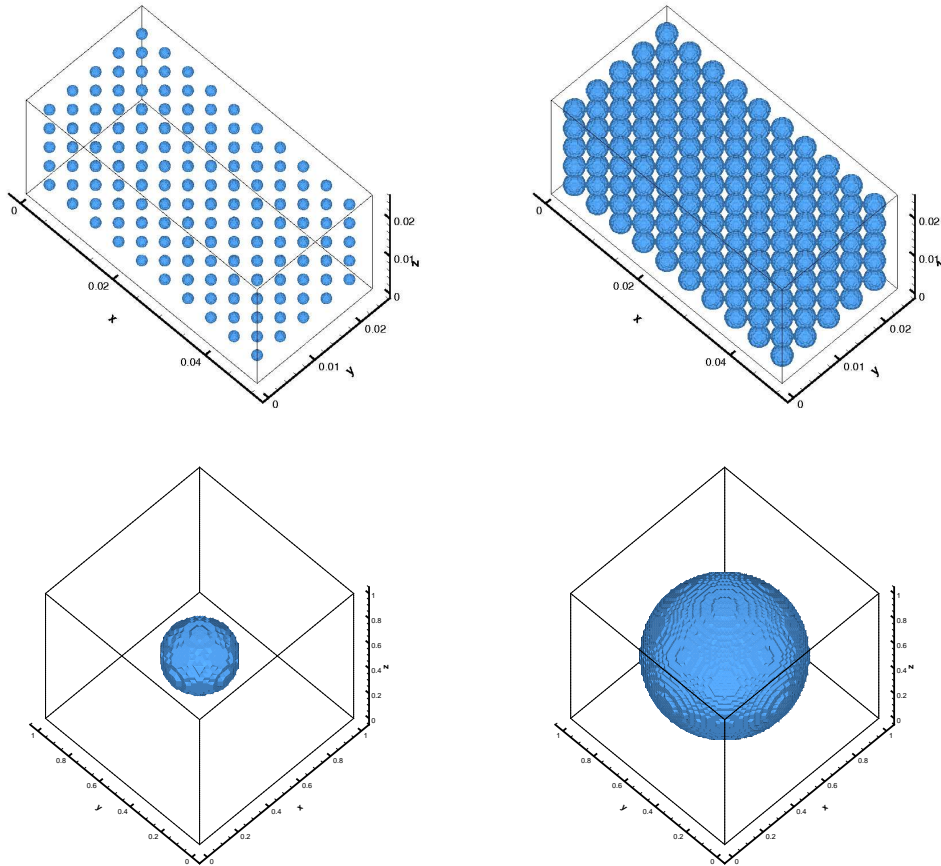


Fig. 7.4.: Microgeometries of the cubic array of spheres for  $\chi = 0.4$  and  $\chi = 0.8$  and their corresponding unit cells.

which is approximated well by the solution of Darcy's Law. All in all, this can be seen as a confirmation that Darcy's Law is a good approximation for the Stokes equations in a periodic porous medium.

## 7.4. Validation of the Stokes/Brinkman Equations

In this section we consider a fluid domain partially filled by the porous medium of Figure 7.4 for  $\chi = 0.8$ . On the macroscale, we apply the Stokes/Brinkman equations according to the fictitious domain approach, penalising the Stokes equations by  $K_{xx} = K_{yy} = K_{zz} = 1.384102e - 02 \cdot 0.005^2$  in the porous medium. Note, that we do not take the value  $K_{xx} = 1.3118e - 02$  from last section, since the sphere is resolved on a much coarser grid: although we resolve the microscale already very highly with  $600 \times 200 \times 200$  grid cells, this still leaves only about  $10^3$  grid cells for a single sphere.

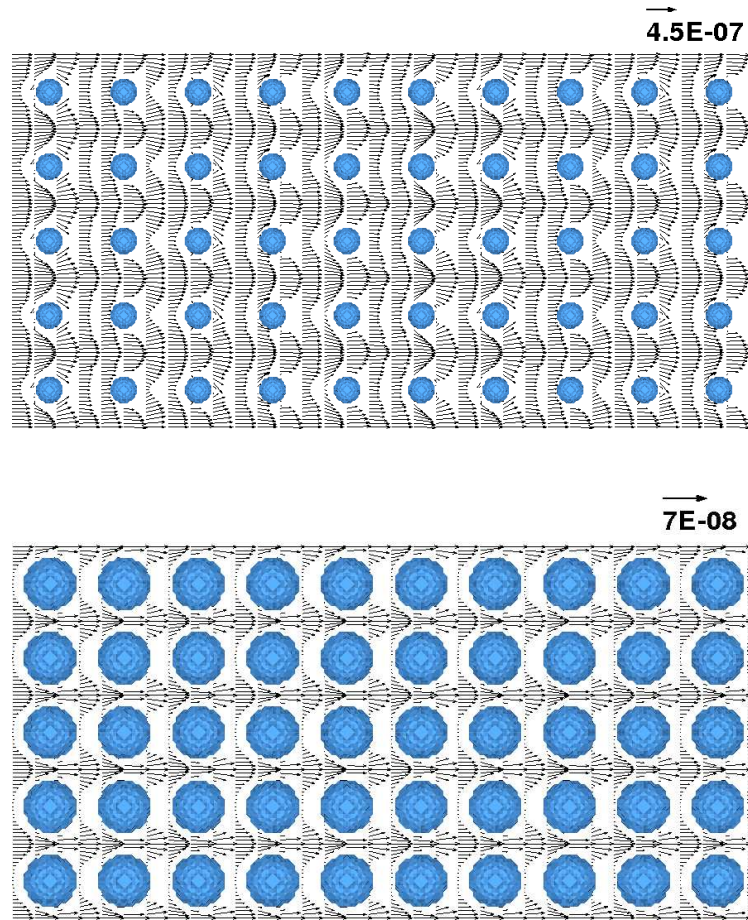


Fig. 7.5.: Velocity field of the Stokes equations in a 2D cut of the microgeometries.

This coarseness is accounted for by solving the Unit Cell Problem with the same coarseness, resulting in the higher permeability  $K_{xx} = 1.384102e - 02$ . Hereby, we minimise the interaction of the discretisation errors resulting from the numerical solution of the Unit Cell Problem for the permeability  $K_{xx}$ , and from the solution of the Stokes equations on the microscale.

Thus, we solve the Stokes equations both in the fluid and in the porous domain on the microscale. For both problems an inflow boundary condition on the wall  $x = 0$  is specified with natural outflow at the opposite wall. As already mentioned, the Stokes problem needs a very fine discretisation, whereas we choose an increasing number of grid cells for the Brinkman problem (Table 7.4).

Note, that we elongated all domains artificially by one third to account for unphysical influences from the natural outflow boundary. This last third of the domain is neither depicted in the plots nor taken into account for the later computation of the norms. However, the given grid cell numbers include the resolution of both visible and the non-visible parts.

In Table 7.4, we compare the discrete  $L_h^2$ -norms of the velocities. In case of the Stokes/

Problem	Resolution	$\ u\ _{L_h^2} / 1e-06$	$\ v\ _{L_h^2} / 1e-05$	$\ w\ _{L_h^2} / 1e-05$
Stokes/Brinkman equations	$045 \times 045 \times 045$	1.0557	5.0790	5.0487
	$270 \times 090 \times 090$	1.0526	6.3609	6.3402
	$360 \times 120 \times 120$	1.0518	6.3928	6.3771
	$540 \times 180 \times 180$	1.0510	6.4214	6.4108
Stokes equations	$600 \times 400 \times 400$	1.0466	6.2209	6.2123

Table 7.4.: Discrete  $L_h^2$ -norms of the velocities computed at steady state for the Stokes and for the Stokes/Brinkman equations.

Brinkman equations, we observe a convergence process with finer grid resolution. If we focus on the velocity component  $u$  only, one could argue, that the norm approximates the one of the Stokes equations, but regarding both other velocity components, this does not seem to be the case. Here, the norm converges to a value larger than the one of the Stokes equations.

All in all, we have to keep in mind, that the Stokes/Brinkman equations on the macroscale are merely an approximation of the Stokes equations on the microscale, so we always make a small but distinguishable error in solving them - instead of the microscopic problem directly.

Interestingly, however, we observe that - even for a much coarser resolution - the Stokes equations are very well approximated by the Stokes/Brinkman equations, which we deduce from the similarity in the norms, as well as from the flow fields depicted in Figure 7.6 and Figure 7.7. In the microscopic case the geometry is explicitly given and the flow field evolves accordingly. In the macroscopic case the rectangle specifies the porous domain, in which information about the geometry is now only kept via the permeability tensor. Still, the flow field evolves in a very similar way around the porous inclusion.

In Figure 7.6 and Figure 7.7 2D cuts of the velocity component  $u$  and of the velocity component  $w$  are depicted, which are the solutions of three numerical setups: the Stokes equations on the microscale as well as the Stokes/Brinkman equations on the finest and on the coarsest grid of Table 7.4.

In the velocity component  $u$ , we hardly observe any difference, apart from the fact that the velocity on the coarsest grid still seems to be slightly affected by the outflow boundary condition on the right. Contrary, the shape and size of the vortices of the velocity component  $w$  on the edges of the porous medium differ a bit. Nevertheless, it is nearly indistinguishable if the fine grid solution offers a better approximation than the one on the coarse grid. Note, that we omit the velocity component  $v$  in our considerations here, since - in this example - it behaves very similar to its counterpart  $w$ .

In conclusion, these results speak for the application of the Stokes/Brinkman equations. We avoid the high resolution and long time that we need for the solution on the microscale and obtain accurate and fast solutions on the macroscale instead.

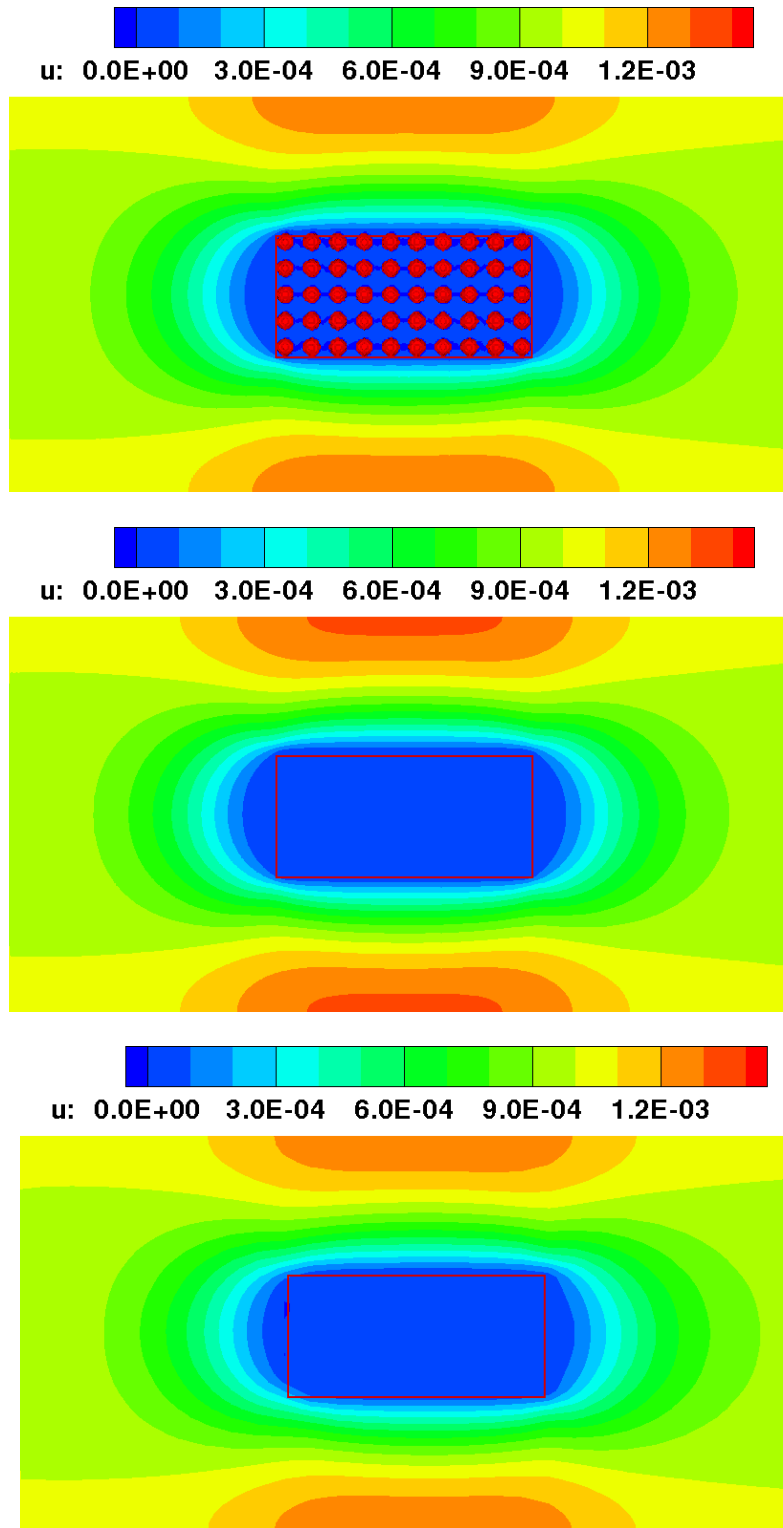


Fig. 7.6.: Comparison of the contours of the velocity component  $u$ : computed in the micro-geometry with the Stokes equations (above) and computed in the macro-geometry with the Brinkman/Stokes equations with  $540 \times 180 \times 180$  grid cells (middle) and  $45 \times 45 \times 45$  grid cells (below). The rectangle denotes the porous part of the domain.

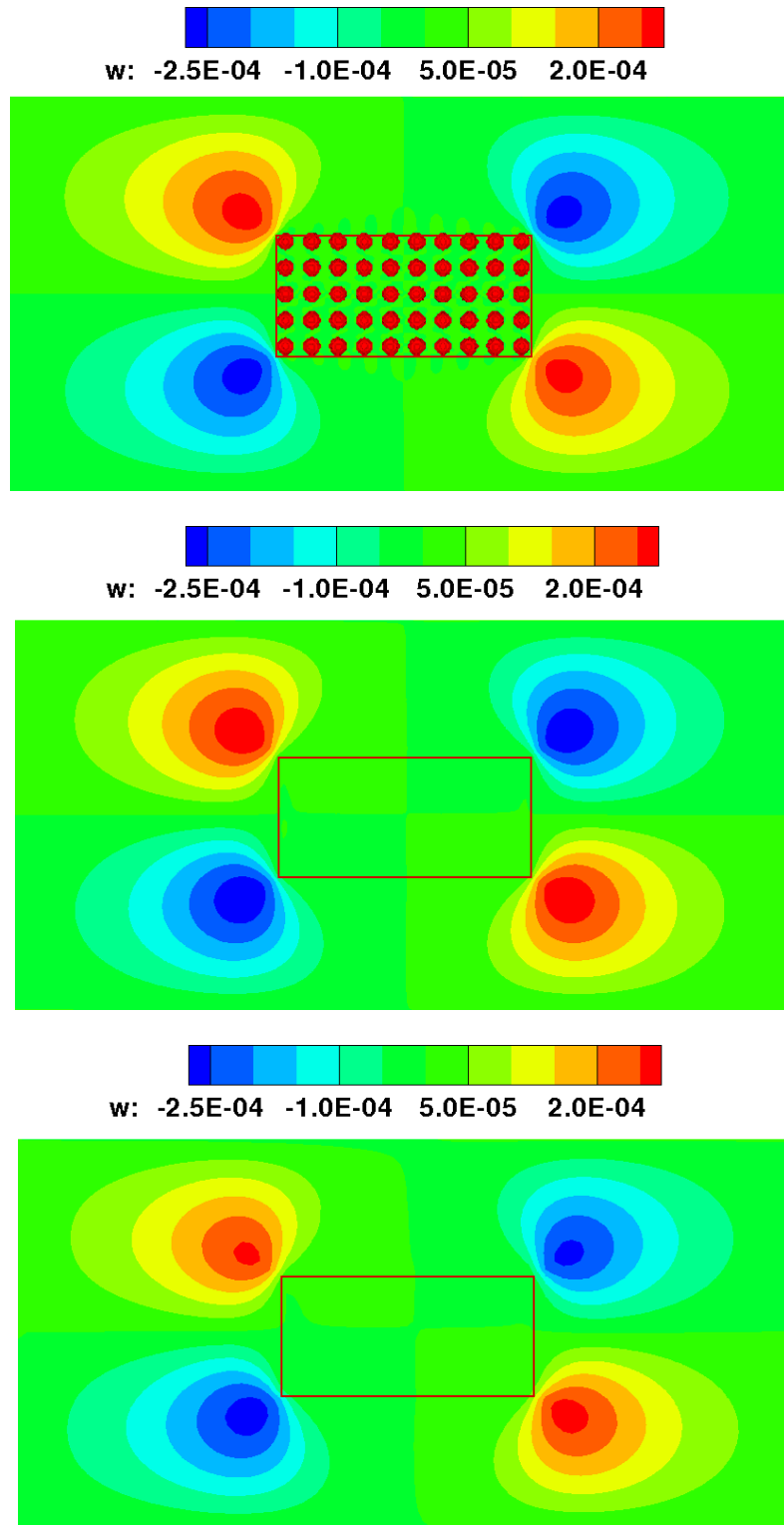


Fig. 7.7.: Comparison of the contours of the velocity component  $w$ : computed in the micro-geometry with the Stokes equations (above) and computed in the macrogeometry with the Brinkman/Stokes equations with  $540 \times 180 \times 180$  grid cells (middle) and  $45 \times 45 \times 45$  grid cells (below). The rectangle denotes the porous part of the domain.

### 7.4.1. Are the Stokes/Brinkman Equations Darcy's Law in the Porous Part?

At this point, we have merely started the numerical experiments concerning the question, if it can be shown numerically that the Brinkman term  $\mu \mathbf{K}_{\text{tow}}^{-1} \mathbf{u}$  dominates over the viscous term  $\mu \Delta \mathbf{u}$  in the Stokes/Brinkman equations and hence, satisfies again Darcy's Law in the porous part. This is certainly not to be expected at interfaces, but could be expected in the internal part, where  $\mathbf{u}$  is sufficiently smooth.

Thus, in the porous part of the fluid/porous domain described in the last section, we compute the least difference between the diffusive and the Brinkman term numerically on the finest grid. At the interface, both the diffusive and the Brinkman term are found to be very high. Their least difference is computed when the Brinkman term  $\mu \mathbf{K}_{\text{tow}}^{-1} \mathbf{u} = 1.8e + 02$  and the diffusive term  $\mu \Delta \mathbf{u} = 1.8e + 02$ . A bit further away from the boundaries, the magnitude of both terms decreases, but they are still approximately equal. However, if we take into account even further away inner points, the Brinkman term  $\mu \mathbf{K}_{\text{tow}}^{-1} \mathbf{u} = 1.89e + 00$  dominates over the diffusive term  $\mu \Delta \mathbf{u} = 1.52e - 04$  considerably.

However, it seems too early to make any more statements about this seldom studied problem. Different geometries, different alignments of the porous inclusions and certainly contour plots of both terms mirroring this behaviour are necessary to confirm and strengthen the above results. Note, that on the interfaces, also the assumptions for Darcy's Law to hold break down, since we always assume no-slip or slip boundaries, not continuity of stress and velocity, in homogenisation theory. Further research will certainly shed more light on this interesting subject.

## 8. Computation of Textile Permeability

In this chapter, we apply our mathematically and numerically developed models on textiles. We present the existing WiseTex [63] and LamTex software for the modelling of textile geometries and provide an insight into the computation of the yarn's permeability on the textile microscale. These semi-analytically computed permeabilities can also be computed numerically by the solution of Darcy's Law, since yarns in a textile are approximated as parallel square arrays of cylinders.

In addition, we present three realistic types of textile reinforcements and compare numerical permeability computations to experimental data. The permeabilities, predicted by our numerical scheme, coincide extremely well with those of real experiments. Note that, in the remainder of this chapter we denote by  $\Delta x$ ,  $\Delta y$  and  $\Delta z$  the local mesh size in  $x$ ,  $y$  and  $z$ -direction respectively.

### 8.1. Textile Architecture

Textiles are hierarchically structured materials, and the hierarchy of the scales ranges from the fibres ( $10^{-5}\text{m}$ ) to the yarns ( $10^{-3}\text{m}$ ) to the fabric ( $10^{-1}\text{m}$ ) to the whole composite part ( $10^0\text{m}$ ) (cf. Fig. 8.1). A key task in permeability modelling is the characterisation of the reinforcement. For the creation of a single layer model of the reinforcement, we use the WiseTex software [63] developed at the Katholieke Universiteit Leuven in Belgium. In practice however, often the permeability of a multi-layered reinforcement is required. Building the geometry model of a multi-layered reinforcement is a complex additional step, for which the LamTex software has been developed.

The results of WiseTex and LamTex provide the input for the flow simulation tool. The software package WiseTex implements a generalised description of the internal structure of textile reinforcements on the unit cell level. The description integrates mechanical models of the relaxed and deformed state of 2D and 3D woven [36, 37, 38, 39], two- and three-axial braided [40], weft-knitted [46] and non-crimp warp-knit stitched [35] fabrics (NCF) and laminates [41] (Fig. 8.2). All these models, including the models of deformed fabrics, use a unified description format of the geometry of the reinforcement unit cell. This format allows the calculation of physical and mechanical parameters of the fibres near an arbitrary point in the unit cell, as well as the fibres' volume fraction and their direction. The reader is referred to [63] for more details.

Furthermore, for an accurate description of the models, the change of the internal geometry of the reinforcement in shear, tension and compression can be calculated, accounting for local variations of the preform in the mould. It is also possible to assess the non-uniformity of the textile structure, creating a sampling of models with randomly perturbed parameters [22, 23]. In this thesis we show computational results for woven and NCF fabrics, but the method can be applied to practically any of the above mentioned types of reinforcements.

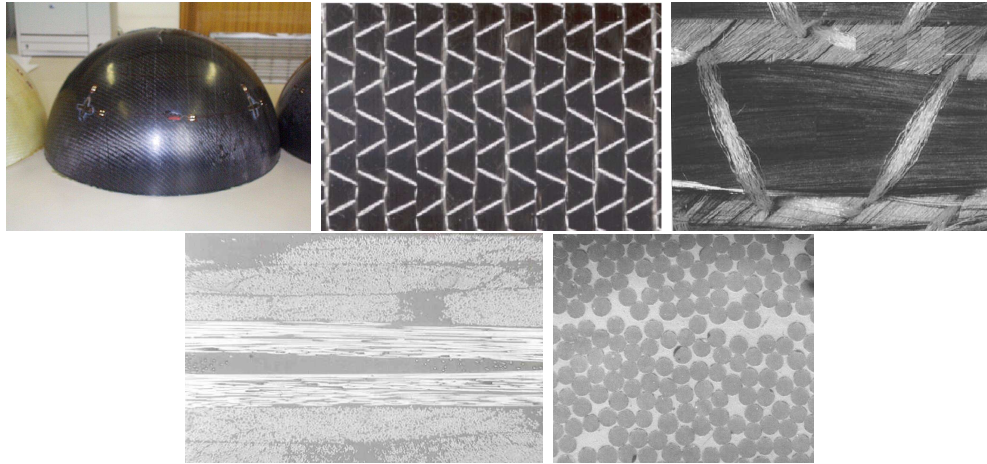


Fig. 8.1.: A hierarchy of textile structures: the part (1m), the reinforcement (0.1m), the unit cell (0.01m), the fibrous structure (0.001m) and the fibres (0.0001m) [Pictures: S.V. Lomov].

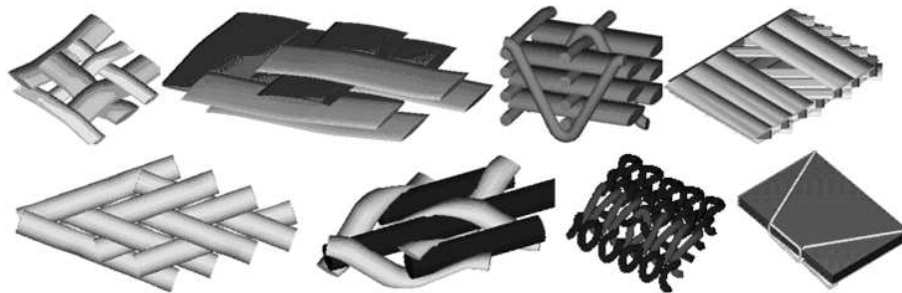


Fig. 8.2.: Examples of models of textile reinforcements: 2D woven; 2D woven laminate; 3D woven; UD laminate; 2-axial braid; 3-axial braid; weft-knitted; Non Crimp Fabric.

## 8.2. The Applied Mathematical Model

We now aim at the application of the in this thesis developed mathematical model on textiles. Again, we consider three porous media scales, i.e. the macroscale, the mesoscale and the microscale (Fig. 8.3). The macroscale is the scale of the fabric part, on which tools like PAM-RTM or LIMS [55, 59] model the injection stage of Resin Transfer Moulding, which is the low-pressure injection of resin into a closed cavity filled with fibre preforms. These tools require the permeability at different positions in the preform model, which we compute on the mesoscale, in a periodic repeat cell of the textile. The different positions in the preform model are accounted for by a large number of computations in unit cells with varying orientation.

On the one hand, the yarns on the mesoscale can be assumed to be solid and thus, do not allow for intra-yarn flow. Then we compute the Stokes or Navier-Stokes equations and insert the computed velocity field  $\mathbf{u}$  and the pressure  $p$  into Darcy's Law for the calculation of  $\mathbf{K}$  as described in Section 2.2.2. In this case, a further possibility is to compute the permeability via the Unit Cell Problem, of which we have shown by homogenisation theory that it is equivalent to Darcy's Law. On the other hand, the yarns can be considered to be porous themselves. Then we compute the Navier-Stokes/Brinkman or Stokes/Brinkman equations in the repeat cell, and again, insert the computed velocity field  $\mathbf{u}$  and the pressure  $p$  into Darcy's Law for the calculation of  $\mathbf{K}$ .

The question remains, how to compute the yarn permeability  $\mathbf{K}_{\text{tow}}$  on the microscale. We could, of course, use the same procedure as on the mesoscale, i.e. solve Darcy's Law or the Unit Cell Problem for the permeability. However, we would like to avoid the complex numerical modelling of a further scale of the textile composite. Instead, we present analytical structure property relations for the computation of  $\mathbf{K}_{\text{tow}}$ , of which two formulas are already employed in the FlowTex software.

## 8.3. Computation of the Local Yarn Permeability

Scanning electron microscopy shows that fibres are arranged in bundles looking like cylinders with ellipsoidal cross-sections [26]. Thus, to compute the local permeability tensor  $\mathbf{K}_{\text{tow}}$  of the yarns, the fibres in the yarns are locally approximated as a regular array of cylinders. The components of  $\mathbf{K}_{\text{tow}}$ , as implemented in the FlowTex software, can then be calculated according to the formulas of Berdichevsky [18] and Gebart [26]:

$$\begin{aligned} K_{\parallel} &= \frac{R^2}{8V_f} \left[ \ln \frac{1}{V_f^2} - (3 - V_f)(1 - V_f) \right] \\ K_{\perp} &= \frac{16}{9\pi\sqrt{2}} \left( \sqrt{\frac{V_{f\text{max}}}{V_f}} - 1 \right)^{\frac{5}{2}} R^2, \end{aligned} \tag{8.1}$$

with  $V_f$  the local fibre volume fraction,  $R$  the radius of the cylinders and  $V_{f\text{max}} = \pi/4$  the maximum fibre volume fraction for a quadratic arrangement of cylinders. In the following we shortly present the main ideas of Gebart and Berdichevsky for the analytic derivation

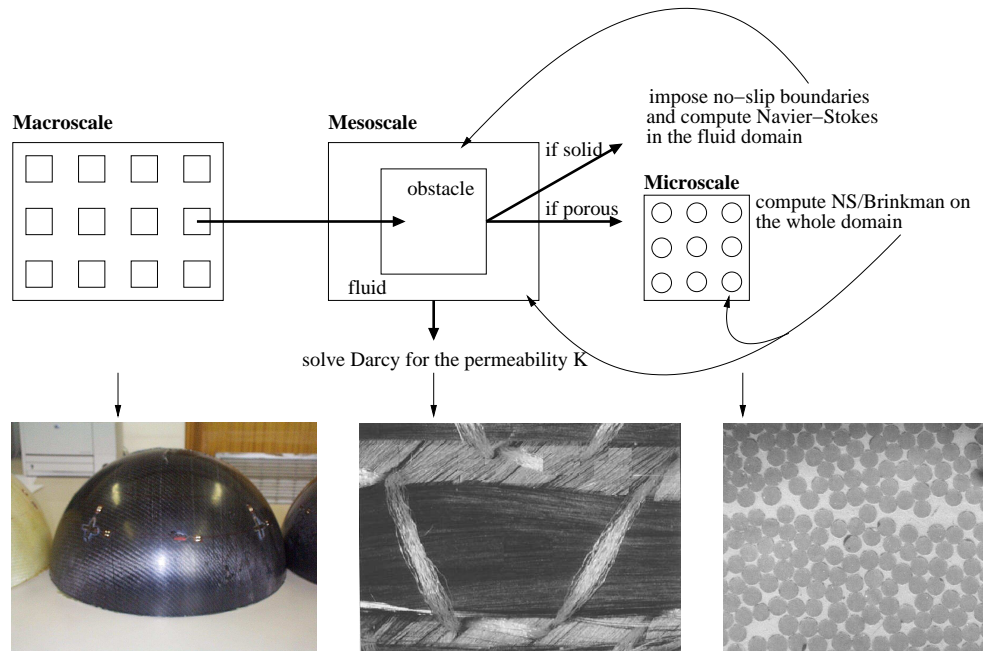


Fig. 8.3.: The interplay of flow equations in the hierarchy of porous media scales transferred onto textile reinforcements.

of the yarn permeability, since both show considerable differences. By a numerical computation of the local fibre permeability and a comparison of possible approximate analytic formulas, we establish why equations (8.1) were chosen for the FlowTex software. Furthermore, we present another formula, which is also given by Berdichevsky and Cai [17] and is supposed to improve their results of [18].

### 8.3.1. Derivation of Yarn Permeability According to Gebart

Two models for the computation of permeability are presented by Gebart for flow along and perpendicular to a perfect arrangement of fibres [26]. In one case, a quadratic packing

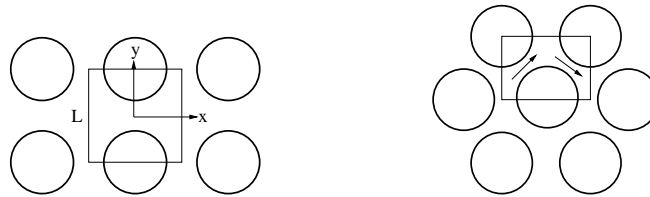


Fig. 8.4.: Definition sketch of the idealised unidirectional reinforcement and its representative cell for quadratic (left) and hexagonal fibre packing (right).

of cylinders is assumed, and in the other a hexagonal packing structure (Fig. 8.4). Since these cylinders are arranged in a periodic pattern, it is sufficient to consider flow in a representative cell of the fibres.

### Flow Perpendicular to the Fibres

Most of the resistance to flow perpendicular to the fibres, can be assumed to come from a small region close to the narrow gap which is formed between the fibres. If the fibres are close to each other, they form a channel whose angle between the wall and the channel centre line is small at all points along the channel (Fig. 8.4). Such a formation is called a slowly-varying channel and is well-understood in fluid dynamics (cf. [26] and the references therein). Thus, if a constant pressure gradient is applied, the pressure difference will vary slowly with the streamwise position. Further, the velocity profile  $v(y)$  will approximately be parabolic along the streamwise coordinate  $x$  giving

$$v(y) = \frac{h^2}{2\mu} \frac{dp}{dx} \left( \frac{y^2}{h^2} - 1 \right), \quad (8.2)$$

with  $h(x)$  the channel half height,  $p$  the pressure,  $\mu$  the viscosity and  $y$  the vertical coordinate.

The volumetric flow rate  $q$  is then found by an integration over the channel half height, which in turn gives an expression for the pressure gradient in terms of geometrical and physical quantities. Combined with Darcy's Law, and rewritten in terms of the fibre volume fraction  $V_f$  and the maximum fibre volume fraction  $V_{f\max}$  for a quadratic fibre arrangement we obtain

$$K_{\perp\text{quad}} = -\frac{16}{9\pi\sqrt{2}} \left( \sqrt{\frac{V_{f\max}}{V_f}} - 1 \right)^{5/2} R^2. \quad (8.3)$$

In a next step, Gebart discusses the same perpendicular flow for a hexagonal arrangement of fibres. The main difference between the computations is that there are now three fibres with two slots through which the fluid might pass (Fig. 8.4), and the equations have to be modified accordingly.

### Flow Along the Fibres

Let us shortly give an idea about Gebart's description of flow along the fibres, which can be expressed in terms of the frictional loss along a duct with an arbitrary cross-section  $A'$ , formed between the fibres. The friction factor or resistance coefficient  $\lambda$  is then defined by

$$\lambda = \frac{\Delta p}{L} \frac{2D_h}{\rho U^2}, \quad (8.4)$$

	Fibre Arrangement	$C_1$	$V_{f\max}$	$c$
Gebart	Quadratic	$\frac{16}{9\pi\sqrt{2}}$	$\frac{\pi}{4}$	57
Gebart	Hexagonal	$\frac{16}{9\pi\sqrt{6}}$	$\frac{\pi}{2\sqrt{3}}$	53

Table 8.1.: Numerical values of the parameters in equations (8.6) and (8.7).

with  $\rho$  the density of the fluid,  $U$  the mean velocity over the cross section and  $D_h$  the hydraulic diameter

$$D_h = \frac{4A'}{O}, \quad (8.5)$$

Again, some of these terms can be expressed in terms of the fibre volume fraction, and a final combination with Darcy's Law yields the formula for the permeability of cross flow.

In summary, permeability as given by Gebart [26] is

$$K_{\parallel} = \frac{8R^2}{c} \frac{(1 - V_f)^3}{V_f^2} \quad (8.6)$$

$$K_{\perp} = C_1 \left( \sqrt{\frac{V_{f\max}}{V_f}} - 1 \right)^{\frac{5}{2}} R^2 \quad (8.7)$$

where equation (8.6) describes the permeability along the fibres and equation (8.7) the permeability of cross flow (transversal to the fibres). The parameters  $C_1$  and the volume fraction  $V_{f\max}$  depend on the fibre arrangement only, while the parameter  $c$  depends on both the fibre arrangement and the fibre volume fraction. These values are listed in Table 8.1.

### 8.3.2. Derivation of Yarn Permeability According to Berdichevsky and Cai

Berdichevsky and Cai [18] present formulas for the computation of the permeability which check

$$K_{\parallel} = \frac{R^2}{8V_f} \left[ \ln \frac{1}{V_f^2} - (3 - V_f)(1 - V_f) \right] \quad (8.8)$$

$$K_{\perp} = \frac{R^2}{8V_f} \left[ \ln \frac{1}{V_f} - \frac{1 - V_f^2}{1 + V_f^2} \right]. \quad (8.9)$$

Their approach is based on the so-called Self-Consistent Method. The major idea is to substitute the effect of the tow on one particular fibre by the effect of some continuum medium with unknown properties. These have to satisfy consistency conditions which give the necessary equations for the unknown properties' determination. The most usual consistency condition is the equivalence of the average flow rate near the fibre and the flow rate in the fibre mat.

Thus, we assume that a circular insertion is placed into a homogeneous porous medium. This insertion contains a fibre and the open space between fibre and circle boundary, which gives two distinct regions: the region outside the insertion, where a homogeneous porous medium resides, and the region inside the insertion, where flow is governed by the Stokes or Navier-Stokes equations. In this case, the consistency conditions demand that the total amount of flow and dissipation energy remains the same with and without the insertion. For instance, in the transversal flow case, Darcy's Law and the continuity equations are employed in the porous medium, and the Stokes equations inside the insertion. These equations have to be matched to the consistency requirements and to the interface and boundary conditions, which results in equation (8.9).

Equations (8.8) and (8.9) lack empirical constants, whereas numerical simulation results clearly show that permeability may vary considerably with the packing structure [18]. Therefore, in another paper [17], Berdichesvsky and Cai aim at an improvement of the presented formulas, and investigate the influence of the maximum volume fraction, and of an additional index for the disturbance status of flow in longitudinal direction. This gives the formulas

$$K_{\perp} = 0.229 \left( \frac{1.814}{V_{f\max}} - 1 \right) \left( \frac{1 - \sqrt{V_f/V_{f\max}}}{V_f/V_{f\max}} \right)^{2.5} \quad (8.10)$$

$$K_{\parallel} = c_1 \frac{1}{V_f} \ln \left( \frac{1}{V_f} \right) \exp(c_2 V_f + c_3 V_f^2), \quad (8.11)$$

with  $c_1 = 0.111$ ,  $c_2 = -1.54$  and  $c_3 = -2.82$  for hexagonal packing. The values of  $c_1$ ,  $c_2$  and  $c_3$  for quadratic packing are not given by the authors, the values for  $V_{f\max}$  can again be found in Table 8.1. Later on in this section, we see a comparison between these improved formulas by Beridchevsky and the original ones.

### 8.3.3. Transformation of the Permeability Tensor

In the afore presented formulas the intra-tow region is assumed to be transversely isotropic [49]. That means, the local  $x$ -axis is located along the direction of the fibre filament and the local  $y$ - and  $z$ -axes point in the cross-filament directions. In this case, the permeabilities  $K_{yy}$  and  $K_{zz}$  are equal, and the local permeability tensor of the intra-tow region reads

$$\mathbf{K}_{\text{tow}}^{\text{loc}} = \begin{bmatrix} K_{\parallel} & 0 & 0 \\ 0 & K_{\perp} & 0 \\ 0 & 0 & K_{\perp} \end{bmatrix}.$$

Of course, in most realistic situations, the local coordinates of the intra-tow region do not align with the global coordinates of the global unit cell. Then, the permeability tensor has to be transformed accordingly. Suppose we have two Euclidean coordinate systems: the local one determined by a set of orthonormal basis vectors  $(\mathbf{e}_1, \mathbf{e}_2, \mathbf{e}_3)$  and the global one by  $(\mathbf{e}'_1, \mathbf{e}'_2, \mathbf{e}'_3)$ . In this case a point  $\mathbf{x}$  with coordinates  $x_1, x_2, x_3$  or  $x'_1, x'_2, x'_3$  respectively

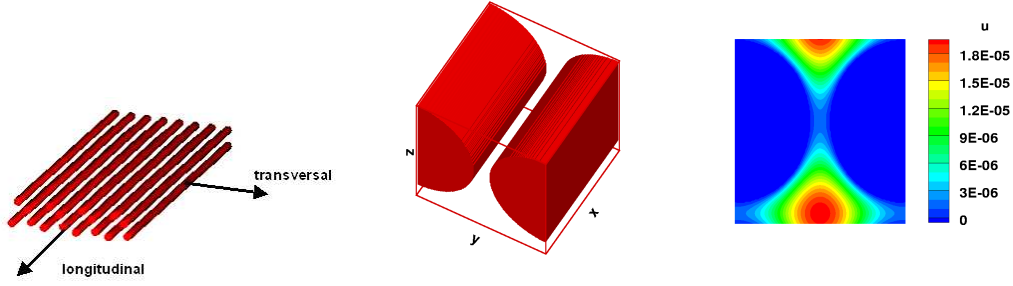


Fig. 8.5.: An impermeable parallel square array of cylinders (left), its unit cell with 62% volume fraction (middle) and a 2D cut of the computed velocity field (right),  $\Delta x = 0.00562$ .

is given by

$$\mathbf{x} = \mathbf{O} + \sum_{i=1}^3 x_i \mathbf{e}_i = \mathbf{O}' + \sum_{i=1}^3 x'_i \mathbf{e}'_i,$$

where  $\mathbf{O}$  and  $\mathbf{O}'$  denote the origins of the coordinate systems. Hence, the transformation from the local to the global system is given by

$$x_i = \mathbf{e}_i(\mathbf{O}' - \mathbf{O}) + \sum_{j=1}^3 R_{ij} x'_j,$$

where  $\mathbf{R}$  denotes the rotation matrix  $R_{ij} = \mathbf{e}_i \mathbf{e}'_j$  with  $\mathbf{R} \mathbf{e}_i = \mathbf{e}_j$ . Thus, we obtain the global permeability tensor by multiplication by such transformation matrices

$$\mathbf{K}_{\text{tow}} = \mathbf{K}_{\text{tow}}^{\text{glob}} = \mathbf{R} \mathbf{K}_{\text{tow}}^{\text{loc}} \mathbf{R}^T.$$

### 8.3.4. Comparison to Finite Volume Numerical Results

Of course, we can also compute the permeability tensor of the tow numerically by either solving Darcy's Law or the Unit Cell Problems in a repeat cell of the packing structure, and compare with the theoretical results by Gebart [26] and Berdichevsky [17, 18].

#### Impermeable Array

We solve the Navier-Stokes equations in a representative cell of a parallel square array of cylinders, and insert the computed velocity field  $\mathbf{u}$  and the pressure  $p$  into Darcy's Law for the computation of  $\mathbf{K}_{\text{tow}}$ . Figure 8.5 shows the computed velocity field in a 2D cut of the representative cell.

For the example of two volume fractions, Table 8.2 gives the calculated permeabilities for different grid spacings: the permeability decreases with  $\Delta x$ . The increase in iterations for the Poisson solver has two reasons. First, a finer mesh requires a smaller time-step, and

$V_f$	$\Delta x$	#gridpoints	#iterations	$K_{along}$
20	0.1	1000	1200	0.05876
	0.05	8000	3900	0.04881
	0.03	35937	10100	0.04626
	0.025	64000	19100	0.04537
62	0.1	729	350	0.004906
	0.05	5832	850	0.003374
	0.03	27000	2100	0.003337
	0.025	46656	2950	0.003178

Table 8.2.: Finite Volume Navier-Stokes solver: results for the parallel square array setup: number of required iterations for the Poisson solver and computed permeability for different fibre volume fractions and mesh sizes.

therefore, more time-steps have to be taken. Second, the preconditioned BiCGStab scheme for the Poisson equation converges more slowly to a solution on a finer mesh, so in each time-step more iterations are required.

In a next step, we increase the volume fraction by a successive increase in the radius  $R$  of the cylinders and compute the permeability of the resulting geometries numerically. Then, we insert the radius and volume fractions into Gebart’s and Berdichevsky’s formulas for an approximate analytical computation of  $\mathbf{K}_{tow}$ . A comparison of the results is plotted in Figure 8.6. First, we note that for the permeability along the fibres, the curves of the analytical formulas show comparable results, although the one given by Gebart yields a higher permeability. Berdichevsky’s formula matches better with the numerical results for the flow along the fibres, although not for higher volume fractions. However, for the flow in the transversal direction, clearly the formula of Gebart gives better results. In this case Gebart’s and Berdichevsky’s formulas differ considerably for higher volume fractions. The FlowTex software calculates the local permeability in (and transversal to) the direction of the fibres according to these observations by equations (8.7) and (8.8).

Additionally, we plot Berdichevsky’s improved formula (8.10) for the transversal permeability in Figure 8.7. There, we compare its results to our numerical permeability computations as well as to those theoretical formulas, that gave the closest results to our numerics in Figure 8.6. Gebart’s and Berdichevsky’s improved formula resemble for higher volume fractions only.

Furthermore, in Figure 8.8, we compare our numerical results to those obtained by a Lattice Boltzmann method [16] developed at the KU Leuven. Both models yield similar permeabilities for all volume fractions<sup>1</sup>.

---

<sup>1</sup>A disadvantage of the Lattice Boltzmann method is the prescribed constant lattice step in all directions, which results in unnecessary large lattice sizes - especially for real world textile reinforcements.

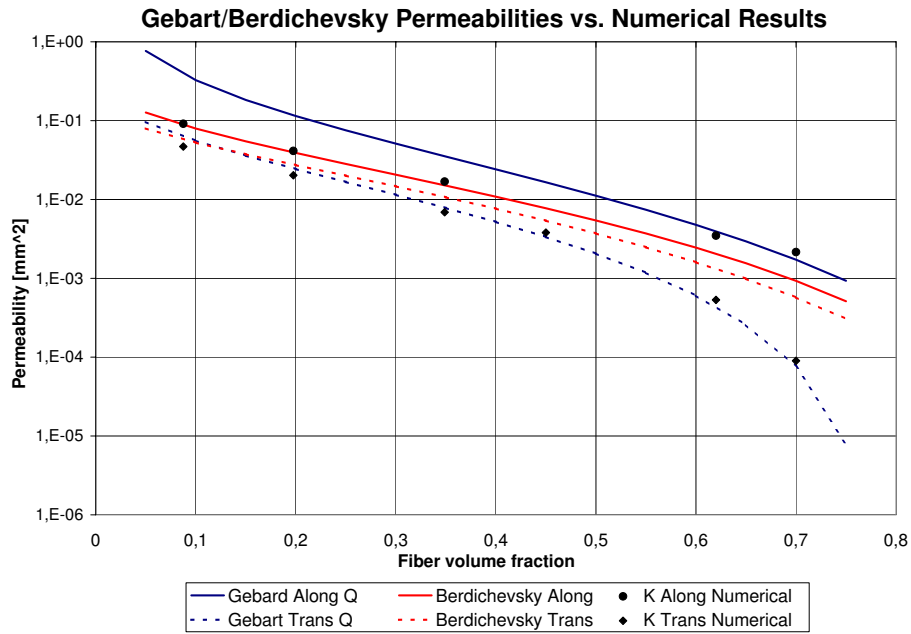


Fig. 8.6.: Comparison of Gebart's and Berdichevsky's formulas for the permeabilities of flow along and transversal to a quadratic packing of cylinders and numerical results.

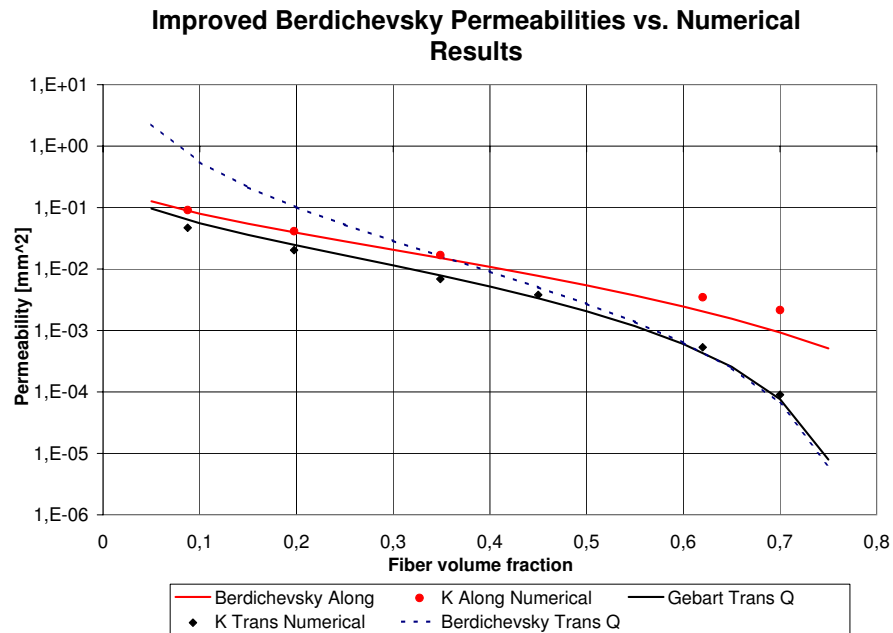


Fig. 8.7.: Gebart's and Berdichevsky's best fitted formulas to numerical results compared to Berdichevsky's "improved" formula for a quadratic packing of cylinders.

### Permeable Array

Since we have now seen a great variety of formulas for the computation of yarn permeability, it seems reasonable to ask, how these different theoretical models affect permeability computations on the mesoscale. Therefore, we compute the Stokes/Brinkman equations in a unit cell of a permeable parallel square array of cylinders, which thus, are assumed to consist out of quadratically packed cylinders themselves. In the following, we have to differentiate between the fibre volume fraction, which we discussed in the previous sections, and the volume fraction of the permeable cylinder in the unit cell.

Again, we insert the computed velocity field  $\mathbf{u}$  and the pressure  $p$  into Darcy's Law for the computation of  $\mathbf{K}$ . For a fixed unit cell cylinder volume fraction of 60%, we vary the fibre volume fraction, and thereby the local cylinder permeability  $\mathbf{K}_{\text{tow}}$ . The theoretical tow permeabilities shall be given by the formulas of Gebart (eqs. 8.6-8.7) and Berdichevsky (eqs. 8.8-8.9). Furthermore, we increase the fibre volume fraction until the cylinder is nearly impermeable and compare to the permeability of an impermeable array of cylinders.

In Figure 8.9 we observe, that when the fibre volume fraction increases (the cylinders become more and more solid), the unit cell permeability converges to the permeability of an impermeable array, independently of all applied theoretical formulas. Furthermore, although Gebart's and Berdichevsky's formulas for the tow permeability of cross flow differ considerably for higher volume fractions (Fig. 8.6), they give nearly the same results in the permeability computations by the Stokes/Brinkman equations and Darcy's Law. Strikingly, in spite of a similar trend of the two tow permeability curves for longitudinal flow (Fig. 8.6), a very different result is obtained for the permeability on the mesoscale (Fig. 8.9).

We have reached a very interesting point here, whose further discussion goes beyond the scope of this thesis. How do two permeabilities on different scales in the same porous medium affect each other? Concerning our observations in Figure 8.9, this question does not seem to have an easy answer. Numerically, a straightforward answer becomes even more difficult, since we do not know how the discretisation errors on both scales interact. Theoretically, we are in an edge zone of homogenisation theory, because it is still unclear that homogenisation of the Stokes/Brinkman equations on the mesoscale really yields Darcy's Law on the macroscale. Clearly, these considerations are worth further discussion and more detailed research.

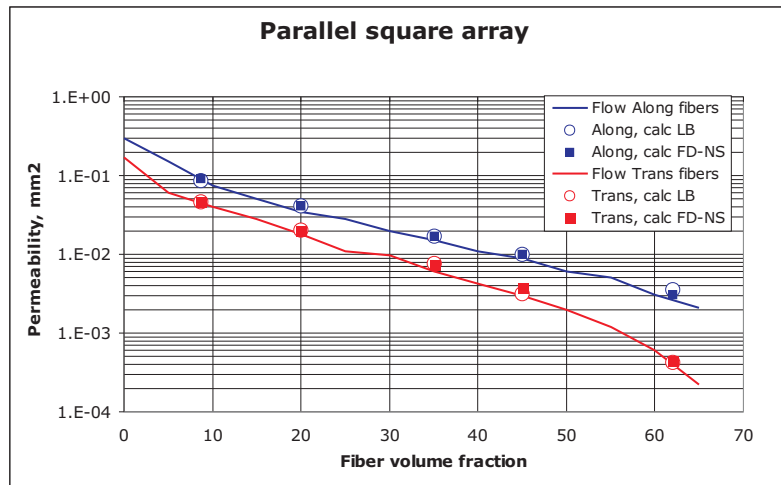


Fig. 8.8.: Permeability for the parallel square array setup with different fibre volume fractions. Full lines: theoretical permeability; circles: lattice Boltzmann results; squares: finite volume Navier-Stokes results.

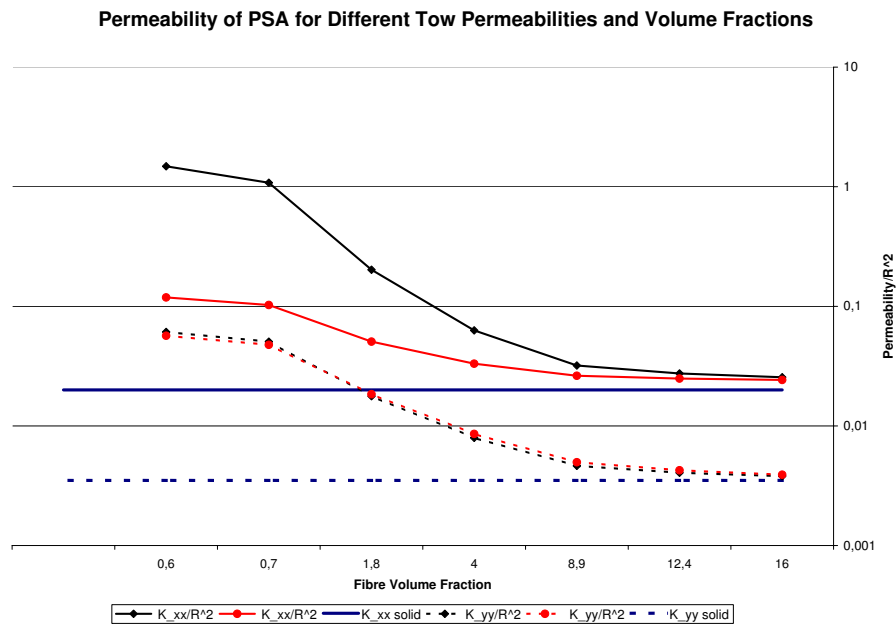


Fig. 8.9.: Computation of the permeability of a parallel square array of cylinders based on different tow permeabilities. The red lines are based on the formulas presented by Berdichevsky for flow along (straight line) and transverse (dashed line) to the fibre, the black ones are based on Gebart's formulas respectively. The horizontal blue lines represent the permeability of an impermeable cylinder. The  $x$ -axes is the fibre volume fraction computed in relation to the whole unit cell, which is why it varies from 0% to 16% only.

## 8.4. Monofilament Fabric

The Monofilament Fabric Natte 2115 is a realistic structure designed as a test fabric for permeability measurements on actual textile reinforcements. For this fabric experimental permeability data is available. The full description of the Monofilament Fabric can be found in [29, 30].

Figure 8.10 shows a photograph of one layer of the real textile geometry. In the middle, we see two layers of the LamTex model of the textile with no nesting and with maximum nesting, and below, we see both models approximated by the voxel geometry of NaSt3DGP with a very high resolution ( $\Delta x = \Delta y = \Delta z = 0.01$ ). The computed flow field of the velocity component  $u$  in the Monofilament Fabric is shown in Figure 8.11 along with a 2D cut, which mirrors the textile geometry exceedingly well.

The yarns of the Monofilament Fabric are impermeable, which is why we solve the Navier-Stokes equations and insert the resulting velocity and pressure into Darcy's Law for the computation of the permeability. We compare the results of our numerical calculations on a two layer model with maximum and minimum nesting and on a single layer model of the reinforcement with the experimental result (Table 8.3).

First of all, both the permeability computations on one layer and on two layers with minimum nesting give the same results, which is to be expected because of the periodicity of the textile structure. The practical experiments were performed with several layers of Natte to fit into the experimental setup: the layers are compressed in the mould cavity, which leads to a random nesting. As a first approximation of such a setup, we compute the average permeability between minimum and maximum nesting. This averaged value and the experimental one coincide very well (Table 8.3). However, permeability does not depend linearly on the volume fraction, which is why further computations in between maximum and minimum nesting would be necessary to confirm this result.

Furthermore, we compute the permeability for a single layer of the Natte fabric with decreasing grid spacing (Fig. 8.12): clearly, the numerically predicted permeability depends strongly on the grid spacing. Thus, for low resolutions, the first order discretisation of the geometry leads to a slightly different actual geometry, which permits a higher flow rate. Hence, on a coarse grid, we actually solve a different problem, which explains the higher permeability. In addition, Figure 8.12 shows calculations that are carried out with semi-implicit as well as with explicit time integration. With semi-implicit time stepping the calculated permeability is slightly smaller than in the explicit case, but for a finer mesh this difference tends to zero.

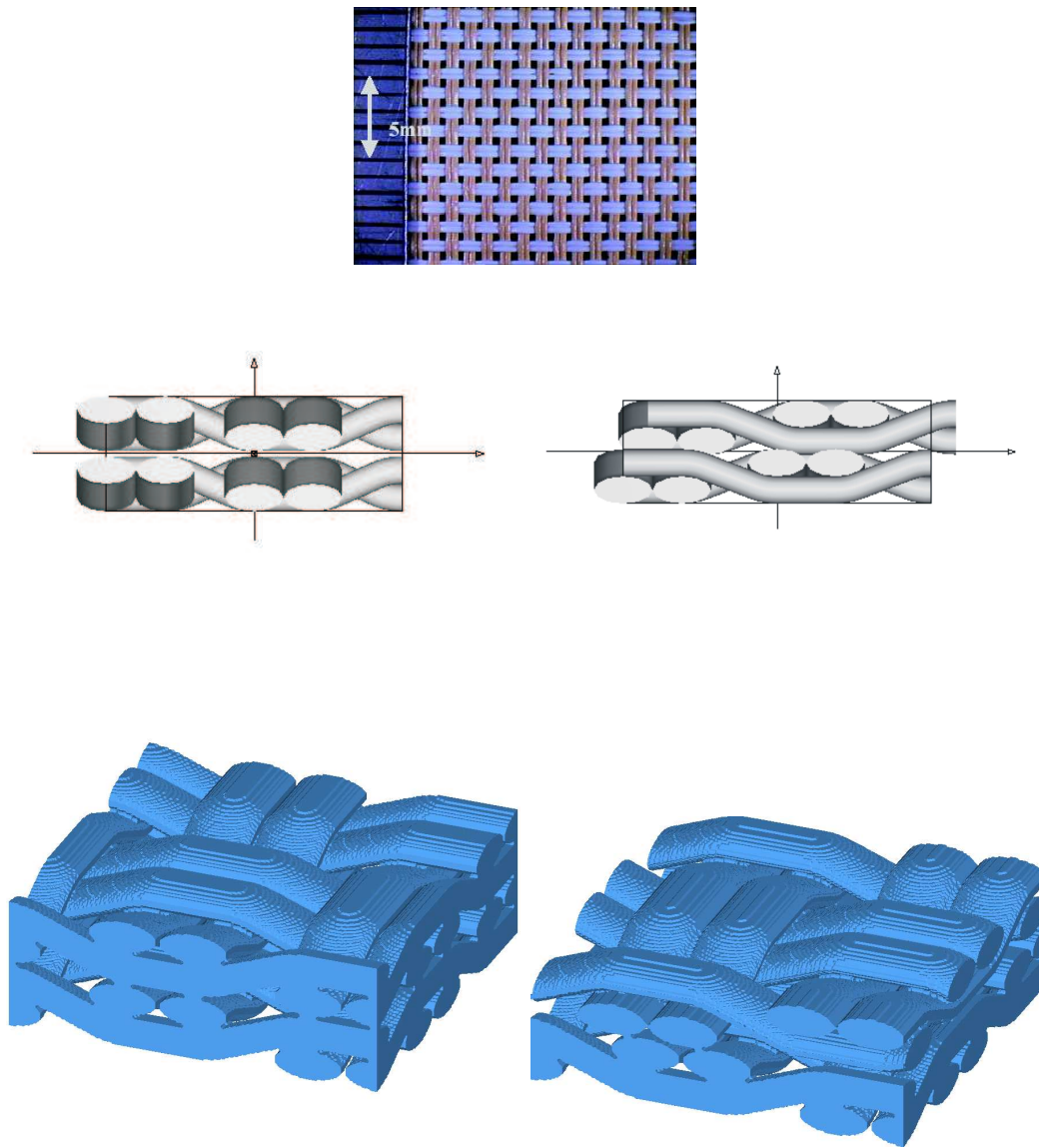


Fig. 8.10.: Two layers of the Monofilament Fabric; left: no nesting, right: maximum nesting. Above: a photograph of a single layer of the real fabric; middle: the textile modelled by the LamTex software; below: the discretisation by NaSt3DGP with grid cell size 0.01.

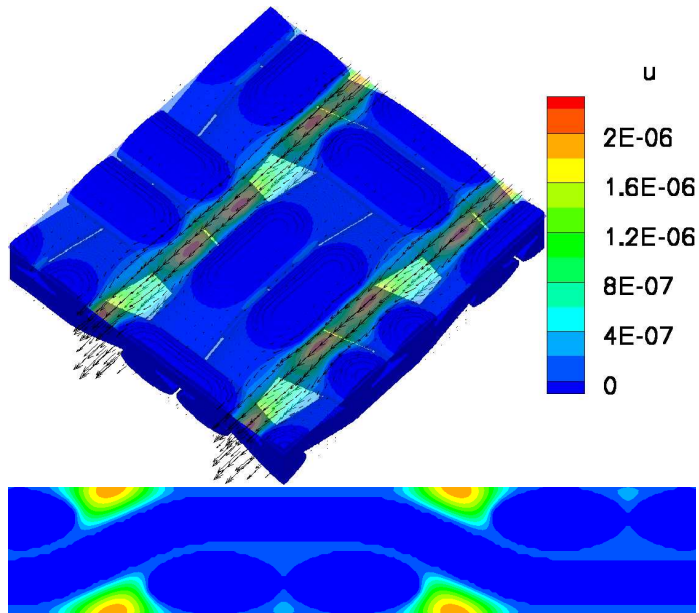


Fig. 8.11.: 3D image and a 2D cut of the calculated flow field in the Monofilament Fabric.

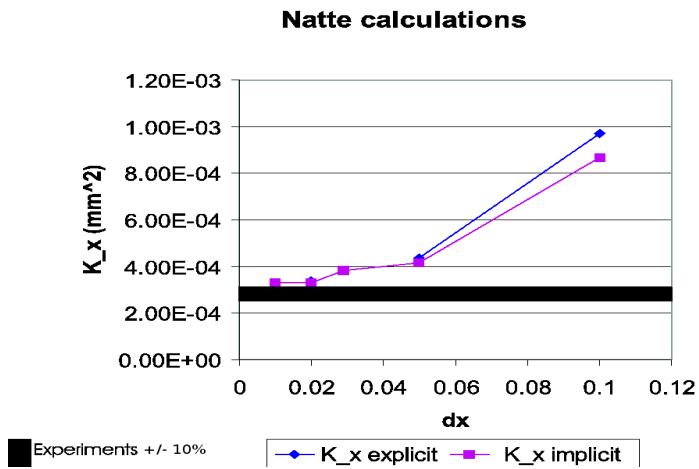


Fig. 8.12.: Permeability  $K_x \equiv K_{xx}$  of the Natte Monofilament Fabric as a function of the grid spacing  $\Delta x$ .

Model	$K_{xx}$ ( $mm^2$ )	$L_x$ ( $mm$ )	$L_y$ ( $mm$ )	$L_z$ ( $mm$ )	Resolution
Single layer	3.289e-04	2.26	2.16	0.4	$226 \times 216 \times 40$
Minimum nesting	3.289e-04	2.26	2.16	0.8	$226 \times 216 \times 80$
Maximum nesting	2.023e-04	2.26	2.16	0.78	$226 \times 216 \times 78$
Average	2.656e-04				
Experimental	$2.7e-04 \pm 10\%$				

Table 8.3.: Permeability results for the Monofilament Fabric with different nesting compared to experiments.  $L$  denotes the total length of the fabric unit cell.

## 8.5. Non Crimp Carbon Fabric

In this section we present experimental validation for a Non Crimp Fabric (Fig. 8.14). Here, we can either take intra-yarn flow into account and solve the Navier-Stokes/Brinkman equations, or we treat the yarns as impermeable and solve the Navier-Stokes equations. In both cases, the permeability is computed via Darcy's Law. Furthermore, we consider two different types of Non Crimp Carbon Fabrics: a biaxial and a quadriaxial carbon fabric, of which Table 8.4 shows the most important parameters - for a more detailed description we refer to [35].

The practical experiments on the biaxial structure were performed by three institutes: MTM (K.U. Leuven), EPFL (Lausanne) and Ecole des Mines (Douai). The results of these experiments are compared to the two numerically computed permeabilities by solving the Navier-Stokes/Brinkman equations for a volume fraction of 38% for the biaxial and of 40% for the quadriaxial Non Crimp Fabric (Fig. 8.13). The numerical parameters of the computational unit cells are summarised in Table 8.5. Experimental and numerical results coincide well for both the biaxial as well as for the quadriaxial fabric, considering that the experimental results themselves show some fluctuations. Unfortunately, numerical results for other volume fractions have been unobtainable so far, since the appropriate WiseTex textile models do not exist.

In Table 8.5 we also see a comparison between the permeabilities computed in the case that intra-yarn flow is taken into account (the Navier-Stokes/Brinkman equations are solved) and in case that the yarns are treated as impermeable (the Navier-Stokes equations are solved). As expected, the permeability in the latter case is slightly lower.

Fabric name	Number of plies	Orientation of plies (degrees)	Mass of the fabric ( $g/m^2$ )	Stitching pattern
Biaxial	2	+45;-45	$322 \pm 16$	Tricot
Quadriaxial	4	0;-45;90;-45	$629 \pm 31$	Tricot-warp

Table 8.4.: Parameters of the Non Crimp Carbon Fabrics.

Preform name	$K_{xx}$ NS	$K_{xx}$ NS/B	$\Delta x$	$\Delta y$	$\Delta z$	$L_x$	$L_y$	$L_z$
Biaxial	2.78e-04	5.04e-04	0.04	0.04	0.03	3.4	4.92	0.45
Quadriaxial	5.27e-04	9.44e-04	0.055	0.0554	0.045	8.195	5.06	0.945

Table 8.5.: Parameters of the Non Crimp Fabrics' unit cells and computational results with the Navier-Stokes (NS) and Navier-Stokes/Brinkman (NS/B) equations. Units are  $mm$  and  $mm^2$ .

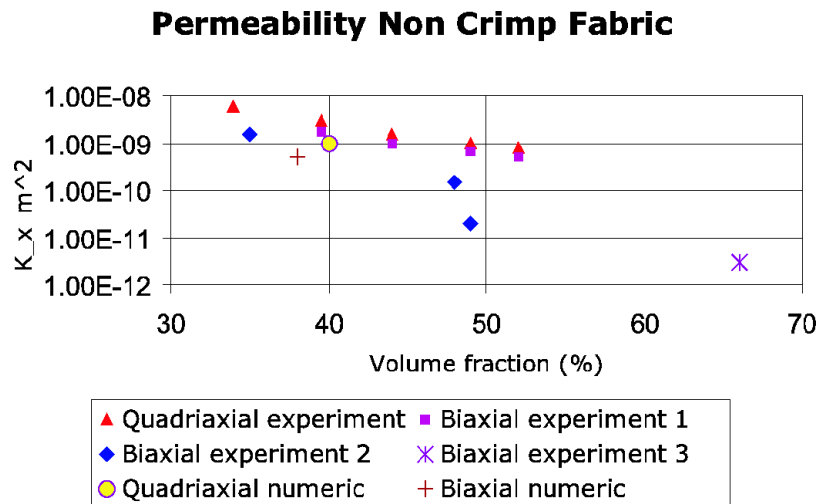


Fig. 8.13.: Permeabilities of the Non Crimp Fabric: two numerical values and the results of experiments.



Fig. 8.14.: WiseTex model of the Non Crimp Fabric.

Model	$K_{xx}$ ( $mm^2$ )	$L_x$ ( $mm$ )	$L_y$ ( $mm$ )	$L_z$ ( $mm$ )	Resolution
Single Layer	2.078e-04	11.7	11.7	0.35	$234 \times 234 \times 70$
Maximum Nesting	1.191e-04	11.7	11.7	0.96	$234 \times 234 \times 192$
Average	1.646e-04				
Experimental	1.0e-04				

Table 8.6.: Results for the Carbon Woven Fabric with different nesting compared to experiments.

## 8.6. Carbon Woven Fabric

In this section, we consider the Carbon Woven Fabric<sup>2</sup> illustrated in Figure 8.15. The fabric models on which calculations are performed, are provided by the LamTex and WiseTex software and contain three layers, which are maximally nested, as well as a single layer of the Carbon Woven Fabric. On the fabric, pressure can be applied, which leads to different volume fractions of the textile.

Table 8.6 shows the results of the permeability calculations for a volume fraction of 50% compared to the experimental result. Again, the experiments were performed with several layers of the Carbon Woven Fabric to fit into the experimental setup. Hence, we compute the average permeability between a single layer and maximum nesting, as an approximation of such a setup. The averaged permeability value slightly overestimates the experimental one, but is still remarkably close to it.

A possible explanation for the overestimation is the first order approximation of the geometry. Certain cells containing a solid fraction of the textile are deleted, if they lead to inconsistent boundary conditions. Thus, since the Carbon Woven Fabric is very compressed (Fig. 8.16), a too rough discretisation leads to many deleted solid cells, a different geometry and a higher flow rate.

For the computations on the Carbon Woven Fabric in this thesis, we already chose a very fine discretisation ( $\Delta z = 0.005$ ) in  $z$ -direction of the fabric. However, an even finer resolution of the whole fabric should lead to even more accurate results.

---

<sup>2</sup>Carbon Woven Fabric has a weave twill 2/2, warp/weft yarns 6K HR carbon flat rovings, ends/picks 3.5 yrns/cm and a (calculated) areal density of  $282g/m^2$ .

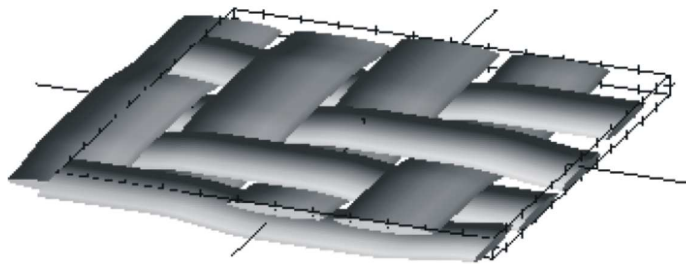


Fig. 8.15.: WiseTex model of the Carbon Woven Fabric.



Fig. 8.16.: 2D cut of three layers maximally nested Carbon Woven Fabric resolved by NaSt3DGP. Red denotes the solid part of the fabric, blue the plain fluid part.



## 9. Conclusion

One of the main aims of this thesis was the fast and accurate prediction of textile permeability by parallel numerical simulation in three dimensions. To this end we applied the theory of homogenisation to the Stokes and Navier-Stokes equations, which lead to Darcy's Law on the textile macroscale and gave a straightforward definition for the computation of permeability via the so-called Unit Cell Problems. The dual porosity of textiles was accounted for by the fictitious domain approach in form of the Navier-Stokes/Brinkman equations, which was extended to allow for non-scalar permeabilities.

We have chosen to solve the Navier-Stokes and Navier-Stokes/Brinkman equations with a finite volume method, based on the software NaSt3DGP. For the implementation, we first employed explicit time advancement of the momentum equations. However, due to the very fine grids for the resolution of complex textile geometries and due to the low Reynolds numbers in textile applications, only very small time steps could ensure the stability of the solution process.

In order to speed up our permeability computations we implemented a semi-implicit pressure-correction method for the finite volume Navier-Stokes(/Brinkman) solver. Due to this substantial implementational improvement, we obtained a dramatic reduction of computation time in all calculations. However, for even finer required resolutions, which are needed by engineers for complicated industrial applications, the semi-implicit sequential simulation - although faster than in the explicit case - was still too time and memory consuming, which challenged us to parallelise the code using a domain decomposition method. By a respective increase in processors, additional textile layers could now be handled extremely efficiently in practically no additional wall clock time. Also, single layers of textiles could now be resolved much more realistically.

In a first step, we numerically computed permeabilities via Darcy's Law, in which velocity and pressure of the steady state Stokes equations are inserted to determine the permeability. However, Darcy's Law does not offer a straightforward definition of all entries of the permeability tensor. Therefore, we showed the numerical equivalence of solving Darcy's Law for the permeability and the scarcely numerically solved Unit Cell Problems - even in more complicated textile structures.

In an idealised porous medium, we presented rare to find comparisons between direct numerical simulation on the microscale and the solution of the Stokes/Brinkman equations on the macroscale in three dimensions. To our knowledge, such comparisons have up to now been carried out in two dimensions only [34]. Although theoretically expectable, it was amazing to observe the strikingly similar evolving flow fields and the truly remarkable coincidence of the kinetic energies in both approaches.

The textile models used in this thesis were designed by the WiseTex or LamTex software developed at the KU Leuven. Employing these models, flow simulations were performed to predict textile permeability. To evaluate the quality of our permeability calculations

for real textiles, we presented validation results for a Monofilament Fabric Natte, a Non Crimp Fabric fabric and a Carbon Woven Fabric, for which practical experimental data is available.

We validated our permeability computations by semi-analytical as well as by other numerical results. However, Neuss' [48] numerical permeability results are given in two dimensions only, and the ones by Bang and Lukkassen [14] do not have the required precision. If a comparison was possible, all results were very close to our predictions.

In addition, the permeability computed in real-world textile reinforcements was in excellent agreement with experiments, which makes the developed software an indispensable tool for textile designing purposes, as for instance needed in Resin Transfer Moulding. Note, that due to our parallelisation strategy, the now feasible fine resolution for the Carbon Woven Fabric, resulted for the first time in more than acceptable permeability predictions for this type of reinforcement.

Even though the above mentioned encouraging results are already a significant improvement over other approaches, there is much room for further research and possible mathematical and numerical extensions.

First of all, we showed permeability results for woven and NCF fabrics, but the method can be applied to practically any types of textile reinforcements. In addition, it should pose no problem to apply the software on, for example, filtration processes, or other porous materials with periodic structures.

At the beginning of this thesis, we mentioned that fluid flow models in porous media applications have to take into account multiple phases, thermal effects, as well as for example, chemical reactions. On this note, thermal effects are already implemented in the NaSt3DGP software. Therefore, we can model these effects in porous media, for instance, to study convection in insulation materials. Furthermore, an extension of NaSt3DGP to free surface and two-phase flows already exists [21] and is ready to be applied to flow simulations in textiles.

Moreover, the extensively studied homogenisation theory in this thesis has already pointed in the direction of non-linear problems. If we allow for a very high viscosity, the convective terms in the Navier-Stokes equations can no longer be neglected, leading in the homogenised limit to the Navier-Stokes system with two pressures. Here, due to the non-linearity, the fast and the slow scale can no longer be treated separately as in the linear case. The arising Navier-Stokes system with two pressures has been solved numerically for the first time in two dimensions only very recently for the application of paper making [52]. However, an extension to the three-dimensional case still lacks.

On a totally different note, the remarkable results of the Navier-Stokes/Brinkman equations encourage us to delve deeper into the subject of the fictitious domain method. We already mentioned its possible applicability in fluid-solid domains, where the solid part is then accounted for by a near zero permeability. Thus, we avoid “flagging problems”, which normally lead to deleted solid cells, if these are inconsistent with the boundary conditions.

However, we can also always improve the applied numerical model. Textile design engineers not only need correct permeability results, they also need them as fast as possible, preferably even on a single workstation. Here, a promising approach to speed up the calculations is a custom-built, sophisticated Stokes solver, that is currently under development at the KU Leuven. In addition, first tests with a parallel algebraic multigrid solver [43],

have already shown to speed up the Navier-Stokes code remarkably.

The presented results for textiles are in excellent agreement with the experimental results. Sometimes, however, textile permeability is slightly overestimated. This may be due to the employed mathematical models, which ignore some physical phenomena (e.g. moving textile boundaries), as well as to the first order discretisation of the boundary conditions. An extension towards higher-order boundary conditions may solve part of this problem. Additionally, the no-slip conditions on the textile boundary do not account for roughness variations with different textiles. Thus, an inclusion of said roughness would lead to a slowing effect on the fluid and to a lower permeability.

In summary, the presented numerical method is only a first, yet very important step, toward efficient permeability prediction and much exciting work remains to be done.

I would like to thank Prof. Michael Griebel for suggesting the topic of this thesis and for his helpful ideas and support in its development. Special thanks to both my supervisors Roberto Croce and Martin Engel, who assisted me in many mathematical and technical questions with great expertise and patience. In writing this thesis, I was strongly encouraged by Dr. Marc Alexander Schweitzer, who offered more than once constructive suggestions and advice.

Part of the research for this thesis was conducted during my stay at the Katholieke Universiteit Leuven in Belgium in March 2006. I would like to thank Prof. Dirk Roose and Prof. Stepan Lomov for their kind hospitality, assistance and valuable knowledge. My sincere gratitude to Bart Verleye for the introduction into the exciting field of permeability computations in textiles. I thank him for innumerable discussions and for his support during this thesis.

Jutta Adelsberger, Kathrin Bacher, Ann-Katrin Becher and Alexander Klitz have reviewed parts of this thesis, offered constructive criticism and answered many of my questions, for which I thank them most gratefully.



## A. Appendix

### A.1. Lebesgue and Sobolev Spaces

Let  $\Omega$  be an open set in  $\mathbb{R}^n$  and let us consider in  $\Omega$  the Lebesgue measure. We denote by

- $L^p(\Omega) := \{f : \Omega \rightarrow \mathbb{R} \text{ such that } \int_{\Omega} |f(x)|^p dx < \infty \text{ for } 1 \leq p < \infty\}$  the Lebesgue space (a Banach space) of  $p$ -integrable functions with the norm  $\|f\|_{L^p(\Omega)} = \left(\int_{\Omega} |f(x)|^p dx\right)^{\frac{1}{p}}$ .
- $L^p(\Omega)^n := \{\mathbf{f} : \Omega \rightarrow \mathbb{R}^n \text{ such that } \int_{\Omega} |\mathbf{f}(x)|^p dx < \infty \text{ for } 1 \leq p < \infty\}$  the Lebesgue space (a Banach space) of vector-valued  $p$ -integrable functions with the norm  $\|\mathbf{f}\|_{L^p(\Omega)^n} = \left(\int_{\Omega} |\mathbf{f}(x)|^p dx\right)^{\frac{1}{p}}$  where now  $|\mathbf{f}|$  denotes the  $p$ -norm  $|\mathbf{f}| = \sum_{i=1}^n (|f_i|^p)^{\frac{1}{p}}$ .
- $L^\infty(\Omega) := \{f : \Omega \rightarrow \mathbb{R} \text{ such that } f \text{ is essentially bounded}\}$  the Lebesgue space (a Banach space) of essentially bounded functions with the norm  $\|f\|_{L^\infty(\Omega)} = \text{ess sup}_{x \in \Omega} |f(x)|$ .

Furthermore, we note that the Lebesgue space of square-integrable (vector and non-vector valued) functions is a Hilbert space with the usual scalar product  $(f, g)_{L^2(\Omega)} = \int_{\Omega} f(x)g(x) dx$ .

We introduce the Sobolev spaces

- $H^{1,p}(\Omega) = \{f \in L^p(\Omega), \nabla f \in L^p(\Omega)^n\}$  (a Banach space) of functions having  $p$ -integrable derivatives with the norm  $\|f\|_{H^{1,p}(\Omega)} = \left(\|f\|_{L^p(\Omega)} + \|\nabla f\|_{L^p(\Omega)^n}\right)^{\frac{1}{p}}$ .
- $H^1(\Omega) = H^{1,2}(\Omega)$  (a Hilbert space) of functions having square-integrable derivatives.
- $H_0^{1,p}(\Omega) = \{f \in H^{1,p}(\Omega) \text{ such that } f|_{\partial\Omega} = 0\}$  of functions  $f \in H^{1,p}(\Omega)$  that vanish on the boundary  $\partial\Omega$ . We use the notation  $H_0^1(\Omega) = H_0^{1,2}(\Omega)$ , and denote the dual space by  $H^{-1}(\Omega)$ , which is the space of all continuous linear functionals on  $H_0^1(\Omega)$ .

### A.2. Two-Scale Function Spaces

Note that the subscript ‘‘per’’ for some function space always means that the functions in this space are periodic. For example,  $C_{\text{per}}(Y)$  denotes functions  $f \in C(Y)$  which are  $Y$ -periodic, and so on. Following [31], we define spaces of functions that have values in Banach or Hilbert spaces.

- $L^2(\Omega \times Y) = L^2[\Omega; L^2(Y)] = \left\{f : \Omega \rightarrow L^2(Y) \text{ such that } \int_{\Omega} \|f(x, \cdot)\|_{L^2(Y)}^2 dx < \infty\right\}$ , the Lebesgue space of functions with a micro- and a macrovariable and its norm  $\|f\|_{L^2[\Omega; L^2(Y)]} = \left(\int_{\Omega} \|f(x, \cdot)\|_{L^2(Y)}^2 dx\right)^{\frac{1}{2}}$ .

- $C_0^\infty[\Omega, C_{\text{per}}^\infty(Y)] = \{f : \Omega \rightarrow C_{\text{per}}^\infty(Y) : \text{supp } f \text{ is compact, } f \text{ has derivatives of all orders}\}$ , the space of test functions with a micro- and a macrovariable.
- $L^2[\Omega; H_{\text{per}}^1(Y)^n] = \left\{f : \Omega \rightarrow H_{\text{per}}^1(Y) \text{ such that } \int_\Omega \|f(x, \cdot)\|_{H^1(Y)}^2 dx < \infty\right\}$ , the Sobolev space of functions with a micro- and macrovariable and its norm  $\|f\|_{L^2[\Omega; H^1(Y)]} = \left(\int_\Omega |f(x, \cdot)|_{H^1(Y)}^2 dx\right)^{\frac{1}{2}}$ .

### A.3. Elementary Inequalities

**Young's inequality** Let  $1 < p, q < \infty$  and  $\frac{1}{p} + \frac{1}{q} = 1$ . Let  $a, b > 0$ . Then

$$ab \leq \frac{a^p}{p} + \frac{b^q}{q}.$$

**Young's inequality with  $\varepsilon$**  Let  $1 < p, q < \infty$  and  $\frac{1}{p} + \frac{1}{q} = 1$ . Let  $a, b, \varepsilon > 0$ . Then

$$ab \leq \varepsilon a^p + C(\varepsilon)b^q$$

for  $C(\varepsilon) = (\varepsilon p)^{-q/p} q^{-1}$ .

**Cauchy-Schwarz inequality** Let  $H$  be a real linear space and let the mapping  $(\cdot, \cdot) : H \times H \rightarrow \mathbb{R}$  denote an inner product. Then for  $u, v \in H$  the Cauchy-Schwarz inequality states

$$|(u, v)| \leq \|u\| \|v\|.$$

**Poincaré's inequality** Assume  $U$  is a bounded open subset of  $\mathbb{R}^n$ . Suppose  $u \in W_0^{1,p}(U)$  for some  $1 \leq p < n$ . Then we have the estimate

$$\|u\|_{L^q(U)} \leq C \|\nabla u\|_{L^p(U)}$$

for each  $q \in [1, p^*]$  with  $p^* = \frac{np}{n-p}$  the Sobolev conjugate of  $p$  and the constant  $C$  depends only on  $p, q, n$  and  $U$ . In particular, for all  $1 \leq p \leq \infty$

$$\|u\|_{L^p(U)} \leq C \|\nabla u\|_{L^p(U)}.$$

## Bibliography

- [1] <http://biosystems.okstate.edu/darcy/LaLoi/basics.htm>.
- [2] <http://enr.smu.edu/waves/porous.html>.
- [3] <http://wissrech.iam.uni-bonn.de/research/projects/NaSt3DGP>.
- [4] <http://www-unix.mcs.anl.gov/mpi/>.
- [5] ALLAIRE, G.: *Homogenization of the Stokes Equations in a Connected Porous Medium*. *Asymptotic Analysis*, 2:203–222, 1989.
- [6] ALLAIRE, G.: *Continuity of the Darcy's Law in the Low-Volume Fraction Limit*. *Annali Scuola Normale Superiore di Pisa, Classe di Scienze*, 4(18(4)):475–499, 1991.
- [7] ALLAIRE, G.: *Homogenization of the Navier-Stokes Equations and Derivation of Brinkman's Law*. *Applied Mathematics for Engineering Sciences*, 1991.
- [8] ALLAIRE, G.: *Homogenization of the Navier-Stokes Equations in Open Sets Perforated with Tiny Holes, Part I: Abstract Framework, a Volume Distribution of Holes, II: Non-Critical Sizes of the Holes for a Volume Distribution and a Surface Distribution of Holes*. *Archive for Rational Mechanics and Analysis*, pages 209–298, 1991.
- [9] ALLAIRE, G.: *Homogenization of the Navier-Stokes Equations with a Slip Boundary Condition*. *Communications on Pure and Applied Mathematics*, pages 605–641, 1991.
- [10] ALLAIRE, G.: *Homogenization and Two-Scale Convergence*. *SIAM Journal on Mathematical Analysis*, 23(6):1482–1518, 1992.
- [11] ALLAIRE, G.: *Two-Scale Convergence and Homogenization of Periodic Structures*, 1993.
- [12] ANGOT, P.: *Analysis of Singular Perturbations on the Brinkman Problem for Fictitious Domain Models of Viscous Flow*. *Mathematical Methods in the Applied Sciences*, 22:1395–1412, 1999.
- [13] ANGOT, P., C.H. BRUNEAU and P. FABRIE: *A Penalization Method to Take into Account Obstacles in Incompressible Viscous Flows*. *Numerische Mathematik*, 81:497–520, 1999.
- [14] BANG, B. and D. LUKKASSEN: *Application of Homogenisation Theory Related to Stokes Flow in Porous Media*. *Applications of Mathematics*, 44(4):309–319, 1999.

- 
- [15] BELL, J.B., P. COLELLA and H.M. GLAZ: *A Second-Order Projection Method for the Incompressible Navier-Stokes Equations*. Journal of Computational Physics, 85:257–283, 1989.
- [16] BELOV, E.B., S.V. LOMOV, I. VERPOEST, T. PEETERS and D. ROOSE: *Modelling of Permeability of Textile Reinforcements: Lattice Boltzmann Method*. Composites Science and Technology, pages 1069–1080, 2004.
- [17] BERDICHEVSKY, A.L. and Z. CAI: *An Improved Self-Consistent Method for Estimating Permeability of a Fiber Assembly*. Polymer Composites, 14(4):314–323, 1993.
- [18] BERDICHEVSKY, A.L. and Z. CAI: *Preform Permeability Predictions by Selfconsistent Method and Finite Element Simulation*. Polymer Composites, 14(2):132–43, 1993.
- [19] BROWN, D.L., R. CORTEZ and M.L. MINION: *Accurate Projection Methods for the Incompressible Navier-Stokes Equations*. Journal of Computational Physics, 186:464–499, 2001.
- [20] CHORIN, A.: *Numerical Solutions of the Navier-Stokes Equations*. Mathematics of Computations, 22:745–762, 1968.
- [21] CROCE, R.: *Ein paralleler, dreidimensionaler Navier-Stokes-Löser für inkompressible Zweiphasenströmungen mit Oberflächenspannung, Hindernissen und dynamischen Kontaktflächen*. Diplomarbeit, Institut für Angewandte Mathematik, Universität Bonn, Bonn, Germany, 2002.
- [22] DESPLENTERE, F., S.V. LOMOV and I. VERPOEST: *Influence of the Scatter of Preform Permeability on the Mould Filling: Numerical Simulations*. In *Proceedings of the 25th International SAMPE Europe Conference*, pages 331–336, Paris, March 2004.
- [23] DESPLENTERE, F., S.V. LOMOV, D.L. WOERDEMAN, I. VERPOEST, M. WEVERS and A. BOGDANOVICH: *Micro-CT Characterization of Variability in 3D Textile Architecture*. Composites Part A, 65:1920–1930, 2005.
- [24] DURLOFSKY, L. and J.F. BRADY: *Analysis of the Brinkman Equation as a Model for Flow in Porous Media*. Physics of Fluids, 30(11):3329–3341, 1987.
- [25] FERZIGER, H. and M. PERIĆ: *Computational Methods for Fluid Dynamics*. Springer, 1996.
- [26] GEBART, B.R.: *Permeability of Unidirectional Reinforcements for RTM*. Journal of Composite Materials, 26(8):1100–33, 1992.
- [27] GHIA, U., K.N. GHIA and C.T. SHIN: *High-Re Solutions for Incompressible Flow Using the Navier-Stokes Equations and a Multigrid Method*. Journal of Composite Materials, 26(8):1100–33, 1992.
- [28] GRIEBEL, M., T. DORNSEIFER and T. NEUNHOEFFER: *Numerical Simulation in Fluid Dynamics, a Practical Introduction*. SIAM, Philadelphia, 1998.

- [29] HOES, K.: *Development of a New Sensor-Based Setup for Experimental Permeability Identification of Fibrous Media*. PhD thesis, Vrije Universiteit Brussel, 2003.
- [30] HOES, K., D. DINESKU, M. VANHUELE, H. SOL, R. PARNAS, E.B. BELOV and S.V. LOMOV: *Statistical Distribution of Permeability Values of Different Porous Materials*. In SOL, H. and J. DEGRIECK (editors): *10th European Conference on Composite Materials (ECCM-10)*, 2001.
- [31] HORNING, U.: *Homogenization and Porous Media*. Interdisciplinary Applied Mathematics Volume 6, Springer-Verlag New York, 1997.
- [32] ILIEV, O. and V. LAPTEV: *On Numerical Simulation of Flow through Oil Filters*. Technical Report, Fraunhofer ITWM, 2003.
- [33] KHADRA, K., P. ANGOT, S. PARNEIX and J.P. CALTAGIRONE: *Fictitious Domain Approach for Numerical Modelling of Navier-Stokes Equations*. International Journal for Numerical Methods in Fluids, 34:651–684, 2000.
- [34] LAPTEV, V.: *Numerical Solution of Coupled Flow in Plain and Porous Media*. PhD thesis, Universität Kaiserslautern, 2003.
- [35] LOMOV, S.V., E.B. BELOV, T. BISCHOFF, S.B. GHOSH, T. TRUONG CHI and I. VERPOEST: *Carbon Composites Based on Multiaxial Multiply Stitched Preforms. Part 1: Geometry of the Preform*. Composites Part A, 33(9):1171–1183, 2002.
- [36] LOMOV, S.V., T. TRUONG CHI, I. VERPOEST, T. PEETERS, D. ROOSE, P. BOISSE and A. GASSER: *Mathematical Modelling of Internal Geometry and Deformability of Woven Preforms*. International Journal of Forming Processes, 6(3-4):413–442, 2003.
- [37] LOMOV, S.V., A.V. GUSAKOV, G. HUYSMANS, A. PRODROMOU and I. VERPOEST: *Textile Geometry Preprocessor for Meso-Mechanical Models of Woven Composites*. Composites Science and Technology, 60:2083–2095, 2000.
- [38] LOMOV, S.V., G. HUYSMANS, Y. LUO, R. PARNAS, A. PRODROMOU, I. VERPOEST and F.R. PHELAN: *Textile Composites Models: Integrating Strategies*. Composites Part A, 32(10):1379–1394, 2001.
- [39] LOMOV, S.V., G. HUYSMANS and I. VERPOEST: *Hierarchy of Textile Structures and Architecture of Fabric Geometric Models*. Textile Research Journal, 71(6):534–543, 2001.
- [40] LOMOV, S.V., A. NAKAI, R.S. PARNAS, S. BANDYOPADHYAY GHOSH and I. VERPOEST: *Experimental and Theoretical Characterisation of the Geometry of Flat Two- and Three-Axial Braids*. Textile Research Journal, 72(8):706–712, 2002.
- [41] LOMOV, S.V., I. VERPOEST, T. PEETERS, D. ROOSE and M. ZAKO: *Nesting in Textile Laminates: Geometrical Modelling of the Laminate*. Composites Science and Technology, 2002.

- [42] MEI, C.C., J.L. AURIAULT and C.O. NG: *Some Applications of the Homogenization Theory*. Advances in Applied Mechanics, pages 277–348, 1996.
- [43] METSCH, B.: *Ein paralleles graphenbasiertes algebraisches Mehrgitterverfahren*. Diplomarbeit, Institut für Numerische Simulation, Universität Bonn, Bonn, Germany, 2004.
- [44] MIKELIC, A.: *Homogenization of Nonstationary Navier-Stokes Equations in a Domain with a Grained Boundary*. Annali di Matematica Pura et Applicata (IV), pages 167–179, 1991.
- [45] MIKELIC, A.: *Homogenization Theory and Applications to Filtration through Porous Media*. To appear in Lecture Notes in Mathematics, Springer, Version of March, 2000.
- [46] MOESEN, M., S.V. LOMOV and I. VERPOEST: *Modelling of the Geometry of Weft-Knit Fabrics*. In *TechTextil Symposium*, pages CD–Edition, Frankfurt, 2003.
- [47] NEDANOV, P.B. and S.G. ADVANI: *Numerical Computation of the Fiber Preform Permeability Tensor by the Homogenization Method*. Polymer Composites, 23:758–770, 2002.
- [48] NEUSS, N.: *Schnelle numerische Approximation von effektiven Parametern mit einer interaktiven Finite-Elemente Umgebung*. Habilitationsschrift, Fakultät für Mathematik und Informatik der Ruprecht-Karls-Universität Heidelberg, 2003.
- [49] NGO, N.D. and K.K. TAMMA: *Complex Three-Dimensional Microstructural Permeability Prediction of Porous Fibrous Media with and without Compaction*. International Journal for Numerical Methods in Engineering, 60:1741–1757, 2004.
- [50] NIELD, D.A. and A.BEJAN: *Convection in Porous Media*. Springer-Verlag, New York, 1999.
- [51] OCHOA-TAPIA, J.A. and S. WHITAKER: *Momentum Transfer at the Boundary between a Porous Medium and a Homogeneous Fluid. I. Theoretical Development*. International Journal of Heat and Mass Transfer, 38:2635–2646, 1995.
- [52] RIEF, S.: *Numerical Solution of the Navier-Stokes System with Two Pressure and Application to Paper Making*. PhD thesis, Universität Kaiserslautern, 2005.
- [53] SANCHEZ-PALENCIA, R.: *Non-Homogeneous Media and Vibration Theory*. Springer-Verlag, Berlin, 1980.
- [54] SANGANI, A.S. and A. ACRIVOS: *Slow Flow through a Periodic Array of Spheres*. International Journal of Multiphase Flow, 8(4):343–360, 1982.
- [55] SIMACEK, P. and S.G. ADVANI: *Desirable Features in Mold Filling Simulations for Liquid Composite Molding Processes*. Polymer Composites, 25(4):355–367, 2004.
- [56] TAM, C.K.W.: *The Drag on a Cloud of Spherical Particles in Low Reynolds Number Flow*. Journal of Fluid Mechanics, pages 537–546, 1969.

- 
- [57] TARTAR, L.: *Incompressible Fluid Flow in a Porous Medium - Convergence of the Homogenization Process*. Appendix of Non-Homogeneous Media and Vibration Theory, pages 368–377, 1980.
- [58] TEMAM, R.: *Navier-Stokes Equations*. North-Holland Publishing Company, 1977.
- [59] TROCHU, F., E. RUIZ, V. ACHIM and S. SOUKANE: *Advanced Numerical Simulation of Liquid Composite Molding for Process Analysis and Optimization*. Composites Part A - Applied Science and Manufacturing, 37(6):890–902, 2006.
- [60] VERLEYE, B., M. KLITZ, R. CROCE, M. GRIEBEL, S.V. LOMOV, D. ROOSE and I. VERPOEST: *Predicting the Permeability of Textile Reinforcements via a Hybrid Navier-Stokes/Brinkman Solver*. In *8th International Conference on Flow Processes in Composite Materials*, Douai, France, 2006.
- [61] VERLEYE, B., M. KLITZ, R. CROCE, D. ROOSE, S.V. LOMOV and I. VERPOEST: *Computation of Permeability of Textile Reinforcements*. In *17th IMACS World Congress*, Paris, France, 2005.
- [62] VERLEYE, B., M. KLITZ, R. CROCE, D. ROOSE, S.V. LOMOV and I. VERPOEST: *Computation of the Permeability of Textiles*. Technical Report, Dept. Computer Science, K.U. Leuven, 2006.
- [63] VERPOEST, I. and S.V. LOMOV: *Virtual Textile Composites Software WiseTex: Integration with Micro-Mechanical, Permeability and Structural Analysis*. Composites Science and Technology, 65(15-16):2563–2574, 2005.
- [64] VORST, H. VAN DER: *BI-CGSTAB: A Fast and Smoothly Converging Variant of BI-CG for the Solution of Nonsymmetric Linear Systems*. SIAM Journal on Scientific and Statistical Computing, 13:631–344, 1992.
- [65] WESSELING, P.: *Principles of Computational Fluid Dynamics*. Springer, 2001.